공학박사 학위논문

Development of SPH-MHD Code for Wire X-Pinch Plasma Simulation

엑스 핀치 플라즈마 시뮬레이션을 위한 SPH-MHD 코드 개발

2023 년 8 월

서울대학교 대학원
에너지시스템공학부
박 수 산

Development of SPH-MHD Code for Wire X-Pinch Plasma Simulation

엑스 핀치 플라즈마 시뮬레이션을 위한
SPH-MHD 코드 개발

지도교수 김 응 수

이 논문을 공학박사 학위논문으로 제출함
2023 년 **7** 월

서울대학교 대학원
에너지시스템공학부
박 수 산

박수산의 박사 학위논문을 인준함
2023 년 **7** 월

위 원 장	정 경 재	(인)
부위원장	김 응 수	(인)
위 원	김 덕 규	(인)
위 원	나 용 수	(인)
위 원	조 영 범	(인)

Abstract

Development of SPH-MHD Code for Wire X-Pinch Plasma Simulation

Su-San Park
Department of Energy System Engineering
The Graduate School
Seoul National University

High-Energy-Density Physics (HEDP) is the study of matter under extreme states of pressure, temperature, and density, which are found in nuclear fusion, star formation, and high-energy-density experiments. Recent advances in experimental and computational techniques have increased the research capacity for HEDP, and the use of HEDP research is increasing in various fields. Pinch plasma, a phenomenon in which plasma is compressed by a magnetic field to form high density, is widely observed and studied as a means of achieving high-energy-density. Especially, the X-pinch has been attracting attention as a valuable tool for exploring high-energy-density physics, as it utilizes a relatively small amount of current to generate intense X-rays.

The computational study of X-pinch plasmas driven by pulsed power

generators is essential because it can replace experimental research that requires a high-performance power supply. Most magnetohydrodynamics (MHD) models for simulating pinch plasmas are based on grid-based methods, which are very mature for well-defined and fixed domains. However, it has been reported that the mixed cell commonly used as the boundary processing between plasma and vacuum causes various errors in the grid-based method. In contrast, Lagrangian numerical methods allow physical fields to move along with particles and are relatively free from such problems. Especially, utilizing the Lagrangian-based Smoothed Particle Hydrodynamic (SPH) methods that completely separate the vacuum and plasma area can be an effective modeling approach. In this respect, an SPH-MHD model has been developed in this study by integrating an MHD model capable of encompassing the extreme conditions of pinch plasma into the SPH framework.

The developed SPH-MHD model has incorporated several numerical treatments, such as a correction term to satisfy the $\nabla \cdot B$ constraint and some artificial dissipation terms to govern the shock wave. Moreover, it includes the evaluation of a novel SPH discretization for non-ideal MHD terms, including current density calculations. The proposed model has been verified with three benchmark cases: (1) Brio & Wu shock tube (ideal MHD), (2) resistive MHD shock simulation, and (3) magnetized Noh Z-pinch problem. The simulation results have been compared with the results of some reference Eulerian MHD simulations and analytical solutions. The simulations well agree with the reference data, and the introduced numerical treatments are effective.

Ultimately, the performance of the developed SPH-MHD code has been assessed by comparing its predictions with experimental data derived from the X-pinch experiment. To accomplish this, detailed physics models specialized for X-pinch physics were integrated into the code. First, the SPH-MHD code was extended to a two-temperature equation that separates the energies of electrons and ions. Because the numerical time step size is much shorter than the electron-ion collision time scale, a two-temperature description of the plasma is adequate in HED plasma. Next, to effectively capture the HED plasma characteristics in the X-pinch condition, the equation of states (EOS) based on the Thomas-Fermi theory was employed. Specifically, it addresses the overestimation of ionization in the low-density regions by adopting the Desjarlais correction model as the plasma ionization balance model. Additionally, a radiation model based on the flux-limited diffusion approximation was incorporated into the code to account for the energy loss through X-ray emission over a wide energy range.

Finally, X-pinch simulations were conducted in full 3D dimensions using the developed code, and these results were compared with experimental data from the X-pinch device at Seoul National University. The simulation successfully captured the implosion behavior of X-pinch plasma, accurately reproducing the four-step X-pinch evolution process commonly observed in various configurations. Additionally, the simulations provided comprehensive spatiotemporal information on various plasma parameters, including density, temperature, velocity field, and radiated power. Notably, the electron temperature and density at the hot spot were well-reproduced when compared with the experimental values, showcasing the accuracy and reliability of the developed

simulation code. Furthermore, the radiation data exhibited significantly higher accuracy compared to previous simulation results, confirming the effectiveness of the proposed model.

The developed SPH-MHD code is expected to be a good alternative for some plasma simulation, which were challenging to address using traditional numerical methods since the numerical scheme used in the code have a high potential for simulation of complicated physics with highly deformable interfaces. To conclude, the developed code is confirmed to be a reliable Lagrangian particle-based CFD tool for HEDP studies, and it shows a high potential to provide comprehensive knowledge of the complex behavior of pinch plasma.

Keywords

High Energy Density Physics (HEDP), Magnetohydrodynamics (MHD), Smoothed Particle Hydrodynamics (SPH), Pinch Palsma, X-pinch, Flux-limited Diffusion Approximation Model

Student Number: 2018-34777

List of Contents

Abstract.....i

List of Contents.....v

List of Figures..... vii

List of Tables.....iX

Chapter 1. Introduction.....1

1.1 Background 1

1.2 Previous studies.....3

1.2.1 Previous studies for pinch simulation.....3

1.2.2 Previous studies for SPH-MHD code development 5

1.3 Objectives.....6

Chapter 2. Development of SPH-MHD model 10

2.1 Smoothed particle hydrodynamics 10

2.1.1 Mathematical concept of SPH 10

2.1.2 SPH kernel weighting function 12

2.1.3 SPH kernel approximation 13

2.2 Magnetohydrodynamics 14

2.2.1 resistive MHD governing equationis 15

2.2.2 Equation of state 16

2.3 SPH-MHD model development 17

2.3.1 SPH formulation for resistive MHD.....17

2.3.2 Numerical techniques applied in the SPH-MHD model 18

2.3.3 Non-ideal MHD terms of the SPH method 24

2.4 SPH-MHD model implementation 17

2.4.1 Algorithm of SOPHIA-MHD model 25

2.4.2 Nearest Neighbor Particle Search (NNPS).....26

2.4.3 Time integration.....27

2.4.4 GPU parallelization 28

2.5 Model verification.....29

2.5.1 Brio and Wu shock tube simulations 29

2.5.2 Resistive MHD shock tube simulations 30

2.5.3 Magnetized Noh Z-pinch Problem 32

Chapter 3. Physics Model for X-pinch Simulation 44

3.1 Challenges for X-pinch simulations.....44
3.2 SPH governing equations for X-pinch simulations.....45
3.2.1 Single-fluid two-temperature model.....45
3.2.2 Electron-ion energy exchange model 47
3.2.3 Radiation model.....49
3.2.4 SPH governing equations 53
3.3 Physical property model.....54
3.3.1 Plasma ionization model.....55
3.3.2 Plasma transport model 56
3.3.3 Plasma opacity model.....59
3.3.4 Algorithm of SOPHIA-X code 60

Chapter 4. X-pinch Simulation.....68

4.1 Experimental setup.....69
4.2 X-pinch simulaton setup 69
4.2.1 Initial conditions for X-pinch simulation 69
4.2.2 Numerical modeling for X-pinch simulation 70
4.3 X-pinch simulation results and discussions 73
4.3.1 Evolution of an X-pinch 73
4.3.2 Evolution of an X-pinch: Micro Z-pinch formation.....73
4.3.3 Evolution of an X-pinch: Jet formation.....74
4.3.4 Evolution of an X-pinch: Hot spot formation.....75
4.3.5 Evolution of an X-pinch: Neck breaking.....77
4.3.6 Radiation emission from the X-pinch hot spot.....78

Chapter 5. Conclusion and Recommendation.....93

5.1 Conclusions.....93
5.2 Recommendations.....95

References.....98

국문 초록 **109**

감사의 글 **114**

List of Tables

Table 1.1. Previous studies on pinch simulation.....7
Table 1.2. Previous studies on SPH-MHD code development 7
Table 2.1. Conditions of kernel function 36
Table 2.2. Types of kernel function.....36
Table 2.3. Four types of SPH derivatives for the non-ideal MHD term 37
Table 2.4. Benchmark problems for developed SPH-MHD code verification 37
Table 4.1. Comparison of X-ray emission time between experiment and simulation 81

List of Figures

Figure 1.1. Citations and publications over time with the keyword 'HEDP' 8
Figure 1.2 The approximate magnitude of various plasma.....8
Figure 1.3. Conceptual description of X-pinch.....9
Figure 1.4. Overview of the research scope.....9
Figure 2.1. Particle System of Smoothed Particle Hydrodynamics (SPH).....38
Figure 2.2. Schematic diagram of particle kernel radius in non-uniform particle distribution 38
Figure 2.3. Simplified algorithm of developed SPH-MHD code 39
Figure 2.4. Biro&Wu shock tube simulation results.....40
Figure 2.5. The pressure field profiles of Brio&Wu shock tube simulation.....40
Figure 2.6. Effects of particle resolution on SPH current density profiles 41
Figure 2.7. SPH current density profiles of resistive MHD shock tube simulation 41
Figure 2.8. SPH current density profiles of resistive MHD shock tube simulation 42
Figure 2.9. Time derivative of magnetic field according to the SPH discretization 42
Figure 2.10. Magnetized Noh simulation results 43
Figure 2.11. Particle arrangement in magnetized Noh simulation.....43
Figure 3.1. Electron and ion collision time and Collisional mean free path on the X-pinch plasma regime 62
Figure 3.2. The schematic diagram for collision frequency as a function of the temperature 63
Figure 3.2. The schematic diagram for collision frequency as a function of the temperature 63
Figure 3.3. Effective ionization level of copper as a function of temperature and density 64
Figure 3.4. Electric conductivity of copper as a function of temperature and density 65
Figure 3.5. Rosseland mean opacity of copper calculated in ATOMIC.....66
Figure 3.6. Simplified algorithm of SOPHIA-X code 67

Figure 4.1. Schematic view of SNU X-pinch device with the filtered AXUV diode array 82
Figure 4.2. Initial condition of the X-pinch simulation 83
Figure 4.3. Time evolution of density distribution in X-pinch simulations 83
Figure 4.4. The time evolution of the maximum plasma density 84
Figure 4.5. The time evolution of the maximum azimuthal magnetic field 84
Figure 4.6. The time evolution of the azimuthal magnetic field distribution 85
Figure 4.7. Time evolution of the axial fluid jet velocity, along the vertical axis at 50 - 350 ns 86
Figure 4.8. Time evolution of the maximum electron temperature 86
Figure 4.9. Temporal evolution of estimated electron densities, electron temperatures, and fast electron fractions around the X-pinch hot spot 87
Figure 4.10. A series of radiographs of wire X-pinch just after the emission of its X-ray burst 87
Figure 4.11. Velocity profile of X-pinch simulations at 300 and 350 nsec 88
Figure 4.12. Time evolution of the radial jet velocity 88
Figure 4.13. Time evolution of the radiation power 89
Figure 4.14. Comparison between the simulated radiation power and the measured X-ray power (55 kV, ϕ30μm) 90
Figure 4.15. Comparison between the simulated radiation power and the measured X-ray power (55 kV, ϕ25μm) 90
Figure 4.16. Comparison between the simulated radiation power and the measured X-ray power (55 kV, ϕ20μm) 91
Figure 4.17. Comparison between the simulated radiation power and the measured X-ray power (50 kV, ϕ25μm) 91
Figure 4.18. Comparison between the simulated radiation power and the measured X-ray power (50 kV, ϕ15μm) 92
Figure 4.19. Radiation loss power of the copper X-pinch (ϕ30μm) 92

Chapter 1

Introduction

1.1 Background

High-Energy-Density Physics (HEDP) is the study of matter under extreme states of pressure (> 1 Mbar), which are found in nuclear fusion, star formation, and high-energy-density experiments. Recent advances in experimental and computational techniques have increased the research capacity for HEDP, and many scientists and engineers striving to devise new methods for exploring and managing matter under extreme conditions. Accordingly, the need for HEDP research is increasing in various fields such as astrophysics, material science, and nuclear fusion energy. This trend is supported by statistical data on research trends. **Figure 1.1** illustrates the number of publications and citations per year obtained using the keyword "HEDP." Both the number of publications and citations have been increasing steadily. Furthermore, it can be seen that the number of citations compared to the number of publications is very large. This phenomenon is believed to be due to the high demand for research in this area, despite the limited number of groups with the expertise required to conduct HEDP research.

A pinch plasma refers to a particular type of plasma configuration where a strong self-generated magnetic field compresses the plasma towards its axis. This

compression occurs due to the interaction of electric currents flowing through the plasma. The magnetic field created by these currents can exert a significant force on the plasma, leading to compression and concentration of plasma along the pinch axis. The resulting plasma column can reach high temperatures and densities belonging to the HED regime (**Figure 1.2**). One of the various pinch configurations, the X-pinch stands out as a particularly intriguing option for small-scale experimentation, as it utilizes a relatively small amount of current to generate intense X-rays. The inherent geometry of two or more thin metallic wires intersecting at a single point leads to very high plasma compression when a fast-rising current of a few hundred kA is applied (**Figure 1.3**). Because of this efficiency, X-pinch plasma has been attracting attention as a valuable tool for exploring high-energy-density physics.

However, the experimental implementation of pinch plasma is inherently challenging due to the requirements of high-performance current sources and a diverse array of diagnostic equipment. Therefore, various numerical approaches have been proposed to describe the complex behavior of pinch plasmas. In recent decades, various pinch simulations have been performed mainly by the Eulerian magnetichydrodynamics (MHD) code and have built up an understanding of the physics of the pinch plasma. However, the Eulerian method requires additional numerical processes to handle complex and deformable boundaries due to their reliance on pre-defined and fixed meshes. Thus, utilizing the Lagrangian-based computational fluid dynamics (CFD) methods that completely separate the vacuum and plasma area can be an effective modeling approach. This approach allows for more concise expressions in MHD calculations conducted at the plasma-vacuum interface.

In this regard, an in-house code was developed by integrating an MHD model capable of encompassing the extreme conditions of pinch plasma into the Lagrangian-based CFD method. Specifically, the code was implemented using the Lagrangian Smoothed Particle Hydrodynamics (SPH) method, widely employed in various physics disciplines. Moreover, a novel non-ideal MHD model was proposed and incorporated for simulating pinch plasma. The performance of the developed SPH-MHD code is assessed by comparing its predictions with experimental data derived from the X-pinch experiment. To accomplish this, detailed physics models specialized for X-pinch physics are integrated into the code.

The developed SPH-MHD code is expected to be a good alternative for some plasma simulation, which were challenging to address using traditional numerical methods since the numerical scheme used in the code have a high potential for simulation of complicated physics with highly deformable interfaces. In addition, this code system can contribute to HEDP research by enabling numerical experiments to be performed under diverse and challenging conditions that are difficult to test.

1.2 Previous studies

1.2.1 Previous studies for pinch simulation

Various resistive MHD model-based Eulerian code has been used to accurately capture rapid changes in pinch plasma behavior. This model is useful for describing plasmas whose local resistivity varies with temperature and pressure.

These previous studies are summarized in **Table 1.1**.

Multi-dimensional resistive MHD codes, such as FLASH, MARED 2D, ZEUS, and ATHENA, have been utilized to study the magnetized Noh Pinch problem and the implosion evolution of simple wire-array Z-pinches (J .Huang et al., 2012; P. Tzeferacos et al., 2012; A. L. Velikovich et al., 2012; N. Ding et al., 2016). The Eulerian modular code PLUTO was recently used to simulate the plasma dynamics of X-pinch experiments with two tungsten wires (A. Skoulakis et al., 2022). Particularly, the GORGON code has been determined to be ideal for MHD plasma applications involving X- and Z-pinch wire configurations (F. N. Beg et al., 2006; J. P. Chittenden et al., 2007; D. Haas et al., 2007; G. W. Collins et al., 2012).

The presence of a vacuum necessitates a specialized numerical approach when dealing with the plasma-vacuum interface within the computational domain. To prevent the occurrence of "non-physical" shocks and ensure stable simulations, researchers have proposed multi-material approximations (W .Fuyuan et al., 2018; A. C. Robinson et al., 2004; W. Neal et al., 2007). Additionally, mixed material elements have been employed to represent the interface between the plasma and the low-density background in ALEGRA code (A. C. Robinson et al., 2008). A transitional region surrounding the plasma can be utilized to model the interface, while the remainder of the domain, characterized by a specific density threshold, is considered a vacuum. In this approach, the vacuum is treated using the vacuum form of Maxwell's equations, which incorporates the displacement current (A. Ciardi et al., 2007).

1.2.2 Previous studies for SPH-MHD code development

Although Eulerian codes are widely used to simulate pinch plasmas under extreme conditions, they require additional numerical processes to handle complex and deformable boundaries due to their reliance on pre-defined and fixed meshes. In contrast, Lagrangian numerical methods allow physical fields to move along with particles and are relatively free from such problems.

Smoothed particle hydrodynamics (SPH) is a Lagrangian-based particle method for solving fluid dynamics equations. Although few SPH codes have been developed to describe the complex behavior of the pinch plasma, it has been employed to simulate various MHD scenarios since it was first proposed by Monaghan in the late 1970s. In 2012, Tricco and Price proposed a smoothed particle MHD (SPMHD) scheme that incorporates the hyperbolic divergence cleaning method. They improved the existing method of Price and Monaghan (2004) by altering the discretization forms for $\nabla \cdot B$ and $\nabla \varphi$. Iwasaki (2011) proposed an SPMHD method based on the Godunov SPH proposed by Inutsuka (2002). Instead of employing the artificial dissipation term used in Price and Monaghan, Iwasaki used a solution of the non-linear Riemann problem to reduce the numerical dissipation. Tsukamoto (2013) suggested an SPH discretization of Ohmic dissipation, and Vela (2019) extended it to the pinch plasma problem through a new boundary treatment method. However, the previously proposed SPMHD methodologies do not afford a consistent SPH discretization for non-ideal MHD terms. Furthermore, pinch plasma constitutes extreme conditions of high temperature of over 10^6 K and high density of over 10^3 kg/m3, which have

not been analyzed in previous studies. A novel process is required to obtain and verify the SPH discretization suitable for pinch plasma simulations under extreme conditions.

1.3 Objectives

The purpose of this study is to construct a numerical code that can simulate the complex behavior of X-pinch plasma. To this end, the research proceeds in the following order: (1) to develop 3D Lagrangian SPH-MHD code valid under extreme conditions of pinch plasma, (2) to integrate detailed physics models for X-pinch simulation, and (3) to further give better understanding and insight on X-pinch dynamics and effect of radiation on X-pinch evolution. The research scope derived here also consists of three stages and the overview of the scope is illustrated in **Figure 1.4**.

In Chapter 2, the non-ideal MHD model is developed and implemented in the SPH framework with valid form under the extreme conditions of pinch plasma. The developed model integrates multiple numerical techniques, each of which is individually validated through separate benchmark simulations. Chapter 3 describes the continued expansion of the developed code through the incorporation of the detailed physics model essential for X-pinch simulation. The chapter proceeds by offering a comprehensive description of the applied physics model and outlines the process of extending the algorithm to accommodate these advancements. Finally, Chapter 4 introduces simulation results and some discussions on the X-pinch simulation, including a comparison with experiments.

Table 1.1. Previous studies on pinch simulation

Study	Numerical Method	Temperature Model	EOS/Transport Model	Radiation Model	Dim
Chittenden (2007)	Eulerian	Two Temperature	Thomas-Fermi	Optically thin	3D
Byun (2022)	Eulerian	Two Temperature	Thomas-Fermi/ Lee-More	Optically thin	3D
Koundourakis (2020)	Eulerian AMR*	One Temperature	SESAME EOS	Optically thin	3D
Oreshkin (2017)	Eulerian	Two Temperature	Ideal EOS/ Brazinskii model	Collisional radiative model	1D
Skoulakis (2022)	Eulerian AMR*	One Temperature	SESAME EOS/ Spitzer/10	Optically thin	3D
Vikhrev (2008)	Eulerian	One Temperature	Ideal EOS	Bremsstrahlung	2D
Angus (2020)	Lagrangian	Two Temperature	Ideal EOS/ Spitzer	X	1D
This study	***Lagrangian (SPH)***	***Two Temperature***	***Thomas-Fermi/ Lee-More-Dejalais***	***Flux-limited model***	***3D***

Table 1.2. Previous studies on SPH-MHD code development

Study	Subject	MHD Model	Temperature Model	Significant Point	Dim
Price & Monaghan (2004)	Riemann problem	Ideal MHD	One Temperature	Apply the hyperbolic divergence cleaning method.	1D
Iwasaki (2011)	Non-linear Riemann problem	Ideal MHD	One Temperature	Employ a non-linear Riemann problem solution to minimize numerical dissipation.	3D
Wurster (2014)	Star formation	Non-ideal MHD	One Temperature	Account for the three non-ideal MHD effects (AD, JH, HE).	3D
Tsukamoto (2013)	Star formation	Non-ideal MHD	One Temperature	Recommend a SPH discretization of Ohmic dissipation	3D
Vela (2019)	Magnetically confined plasma	Non-ideal MHD	One Temperature	Suggest a boundary treatment with ghost particles allocation	3D
This study	***High-energy-density Pinch Plasma***	***Non-ideal MHD***	***Two Temperature***	***Propose a non-ideal MHD term suitable for extreme conditions***	***3D***

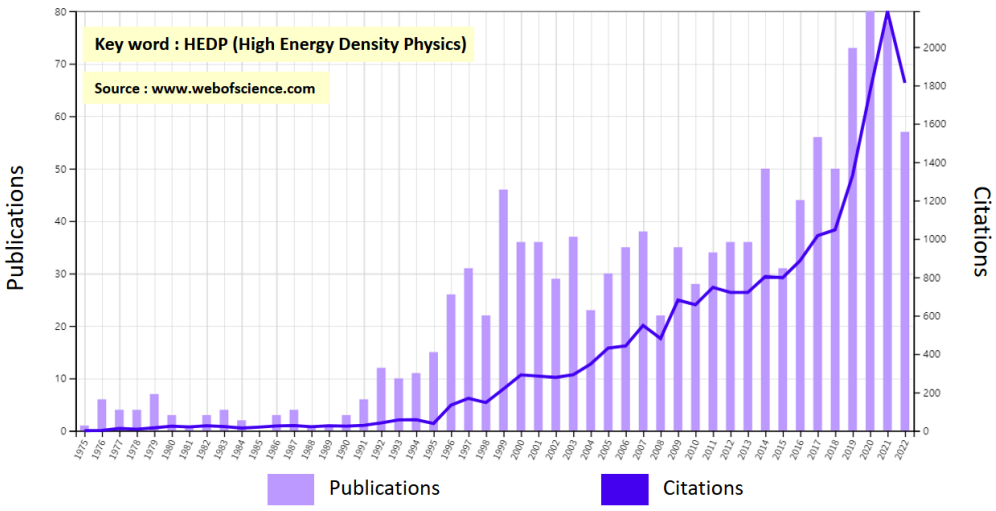

Figure 1.1. Citations and publications over time with the keyword 'HEDP'

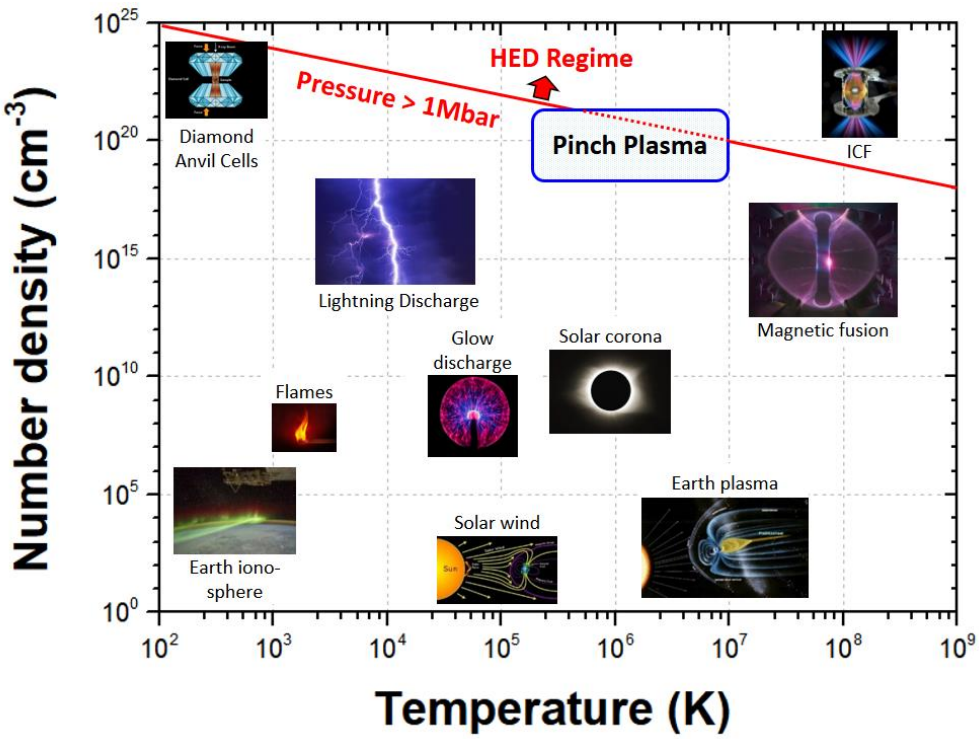

Figure 1.2. The approximate magnitude of various plasma. Here, the blue box represents pinch plasma, and the red line represents the pressure criterion of 1 Mbar classified as a high-energy-density (HED) regime.

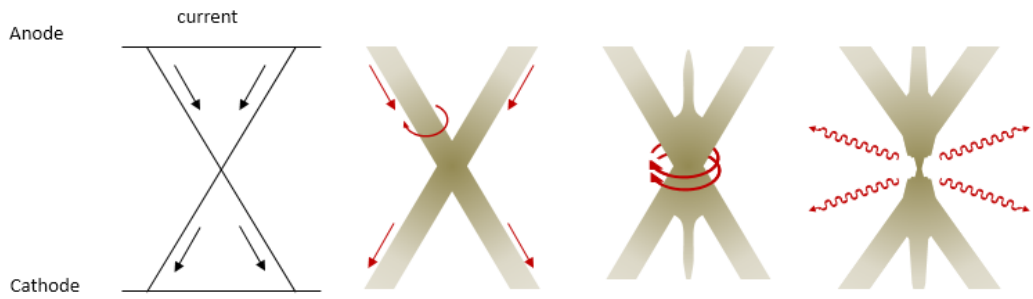

Figure 1.3. Conceptual description of X-pinch

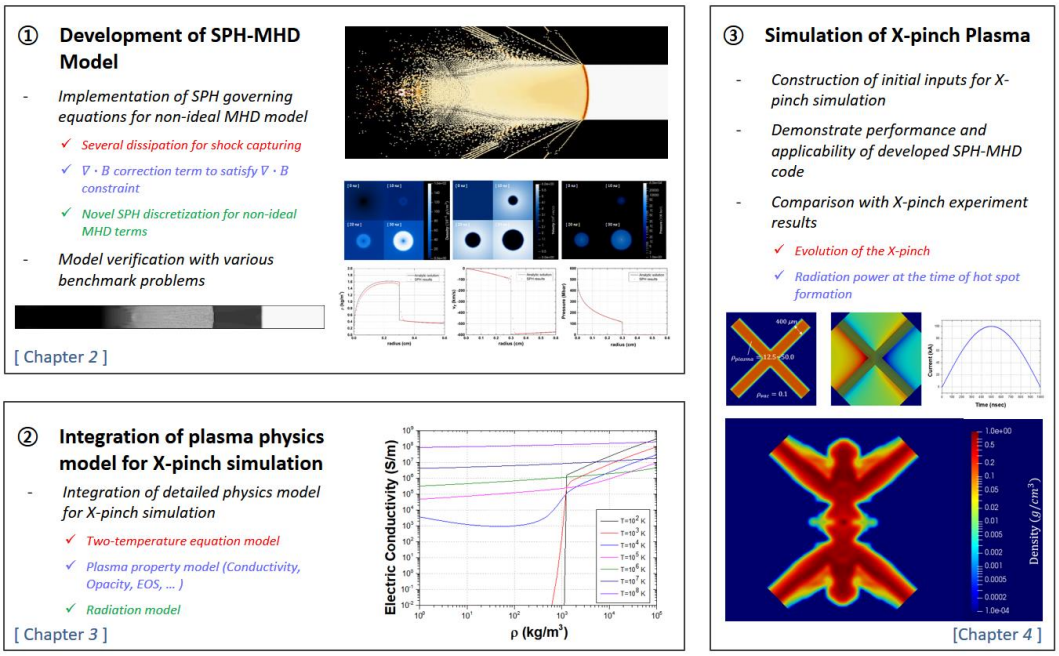

Figure 1.4. Overview of the research scope

Chapter 2

Development of SPH-MHD code

2.1 Smoothed particle hydrodynamics

Smoothed Particle Hydrodynamics (SPH) is a Lagrangian based particle method to solve fluid dynamics equations. Recently, it has been used in various fields with the development of computing techniques. The SPH method has definite advantages over the traditional grid-based numerical methods in dealing with applications that involve large deformations. For this reason, it is relatively easy to implement various types of physics, and therefore it is expected to be fit well into the simulation of pinch plasma. In this section, the basic concept of SPH method and the SPH formulations of the MHD model used to simulate plasma behavior are explained.

2.1.1 Mathematical concept of SPH

In the SPH method, the entire fluid system is expressed by a finite number of particles representing the material properties of that space, and the physical quantities such as density, momentum, and internal energy are calculated through the smoothing of neighboring particles. The smoothing procedure in the SPH method is based on the theory of integral interpolants using a delta function.

$$f(r) \ = \int_{\Omega} f(r')\delta(r - r', h)d\Omega \tag{2.1}$$

However, the delta function is a discontinuous function, and hence it is difficult to handle numerically. To solve this problem, the delta function can be approximated as a continuous function W (known as the smoothing kernel function) with a characteristic width h (known as the smoothing length), and the integral interpolant of a function f is defined as follow:

$$f(r) \ = \int_{\Omega} f(r')W(r - r', h)d\Omega + \mathcal{O}(h^2) \tag{2.2}$$

The integral form of Eq. (2.2) can be discretized by representing the integral with a summation expression, and it ensures the second-order accuracy for h.

$$< f(\boldsymbol{r}_i) > \ = \sum_j f_j W(\boldsymbol{r}_i - \boldsymbol{r}_j, h) V_j \tag{2.3}$$

where, $f(\boldsymbol{r}_i)$ is a function at the position $\boldsymbol{r}_i$, subscript j is the nearby particles of center particle i, and $V(= m/\rho)$ is the particle volume. Applying the relation between mass and density, the above Eq. (2.3) can be transformed to the equation below:

$$< f(\boldsymbol{r}_i) > \ = \sum_j f_j W(\boldsymbol{r}_i - \boldsymbol{r}_j, h) \frac{m_j}{\rho_j} \tag{2.4}$$

Figure 2.1 shows the particle distribution with the kernel function. The value of the kernel function is determined by the distance between particles, and it must be normalized over the entire computational domain.

2.1.2 SPH kernel weighting function

In order for the kernel function to be applied as an averaging weighting function in the SPH method, it has to satisfy some mathematical properties of the delta function (G. R. Liu, 2003). The first condition for the kernel function is the 'unity condition', which means that the integral value over the entire volume should have the value of one, the same as the delta function. In addition, since it is not possible to perform a calculation for an infinite area, the value of the kernel function must be zero outside the support domain (compact condition), and it must always have a positive value within the support domain (positive condition). Also, the 'decay condition' that the kernel function value monotonically decreases as the distance from the reference particle increases, the 'delta function condition' that the function becomes the same as the Dirac-delta function as h approaches to zero, and the 'symmetric condition' that it must be symmetric function, must be satisfied. These conditions are summarized in **Table 2.1**.

Various types of kernel functions that satisfy these conditions have been proposed, and each kernel function has some characteristic pros and cons. Therefore, it is important to select and use the appropriate one depending on the applied physical model. The SPH model developed in this study equipped three types of kernel functions (Gaussian/Quartic/Wendland), and each weighting

function is summarized in **Table 2.2**. Among these, the Wendland function is known to be able to prevent particle clustering because it has a non-negative Fourier transform in the multi-dimensional analysis (W. Dehnen et al., 2012). Additionally, through some simulations, it has been confirmed that the Wendland kernel function yields the most converged results for the kernel approximation, surpassing the other two options. As a result, the Wendland function is utilized as the kernel function in this study to simulate various physical problems.

2.1.3 SPH kernel approximation

The approximation for the scalar field gradient can be derived by taking the spatial derivative of Eq. (2.2). Since the function that depends on $\boldsymbol{r}$ on the right side is only the smoothing kernel function W,

$$\nabla f(r) = \int_{\Omega} f(r')\nabla W(r - r', h) d\Omega + \mathcal{O}(h^2) \tag{2.5}$$

Finally, this may be discretized in the same way as Eq. (2.4), to give

$$< \nabla f(\boldsymbol{r}_i) >= \sum_j f_j \ \nabla W(\boldsymbol{r}_i - \boldsymbol{r}_j, h) \ \frac{m_j}{\rho_j} \tag{2.6}$$

Eq. (2.6) is a widely used SPH gradient approximation, but since it is not a symmetrical shape for particle i and particle j, it leads to quite poor gradient estimates. In addition, the adaptive SPH (ASPH) method (detail explained in

Section 4.3) is applied for simulations with particle imbalance occurring caused by shock. In the ASPH method, it has been observed that the utilization of the asymmetrical form leads to non-conservation of physical quantities. By considering the vector calculus presented below, a symmetric form for the SPH gradient interpolation is derived, which holds true for all $n \in \mathbb{R}$.

$$\nabla(f\rho^n) = nf\rho^{n-1}\nabla\rho + \rho^n\nabla f \tag{2.7}$$

Summarizing this for ∇f,

$$\nabla f = \frac{1}{\rho^n}[\nabla(f\rho^n) - nf\rho^{n-1}\nabla\rho] \tag{2.8}$$

By substituting $f\rho^n$ and ρ into Eq. (2.6), a general interpolant for ∇f can be obtained,

$$< \nabla f(\boldsymbol{r}_i) >= \frac{1}{\rho_i^n}\sum_j m_j\left[f_j\rho_j^{n-1} - nf_i\rho_i^{n-1}\right] \nabla W\left(\boldsymbol{r}_i - \boldsymbol{r}_j, h\right) \tag{2.9}$$

In particular, in the case of $n = -1$, the symmetrical SPH gradient approximation can be obtained as follows:

$$< \nabla f(\boldsymbol{r}_i) >= \rho_i \sum_j m_j \left[\frac{f_i}{\rho_i^2} + \frac{f_j}{\rho_j^2}\right] \nabla W\left(\boldsymbol{r}_i - \boldsymbol{r}_j, h\right) \tag{2.10}$$

Similarly, other SPH formulations for differential operators, such as divergence and curl, can be derived based on the kernel interpolation scheme (J. J. Monaghan et al., 2001).

2.2 Magnetohydrodynamics

Magnetohydrodynamics (MHD) is the study of the magnetic properties and behavior of electrically conducting fluids, specifically plasmas. Plasma is a state of matter that comprises charged particles such as ions and electrons. In principle, to describe plasma behavior, the equation of motion of each particle needs to be calculated. However, since plasma contains abundant particles, solving the equations of motion for each particle is impractical. Instead, MHD equations are derived by treating the plasma as a continuum, where the fluid is assumed to have the same properties at each unit domain (H. Alfven, 1942). This simplification allows for a more tractable description of plasma behavior and has been proven to be a powerful tool for understanding and predicting plasma dynamics. The MHD equations are a combination of the Navier–Stokes equations of fluid dynamics and Maxwell's equations of electromagnetism. These differential equations need to be simultaneously solved, either analytically or numerically. Various MHD equations can be derived depending on the type of plasma and applied assumptions.

2.2.1 Resistive MHD governing equations

The MHD equations used herein are the resistive MHD equations that include the effect of plasma resistivity in ideal MHD. In this section, the governing equations constituting the MHD equations are described. The main variables characterizing an electrically conductive fluid are the bulk plasma velocity field $\boldsymbol{v}$, internal energy u, mass density ρ, and thermodynamic pressure P. The

flowing charged particles are the source of the magnetic field $\boldsymbol{B}$, and current density J. All these parameters generally vary with time t. By neglecting the displacement current, plasma viscosity, and thermal conduction, the equations based on the resistive MHD model can be expressed using the Lagrangian derivative $d/dt = \partial/\partial t + \boldsymbol{v} \cdot \nabla$, as shown below (T. Boyd and J. Sanderson, 1920):

$$\frac{d\rho}{dt} + \rho(\nabla \cdot \boldsymbol{v}) = 0 \tag{2.11}$$

$$\frac{d\boldsymbol{v}}{dt} = \frac{1}{\rho}\nabla \cdot \left(\frac{\boldsymbol{B} \otimes \boldsymbol{B}}{\mu_0} - \left(\frac{|\boldsymbol{B}|^2}{2\mu_0} + P\right)\overleftrightarrow{I}\right) \tag{2.12}$$

$$\frac{d\boldsymbol{B}}{dt} = -\boldsymbol{B}(\nabla \cdot \boldsymbol{v}) + (\boldsymbol{B} \cdot \nabla)\boldsymbol{v} - \nabla \times \eta \boldsymbol{J} \tag{2.13}$$

$$\frac{du}{dt} = -\frac{P}{\rho}(\nabla \cdot \boldsymbol{v}) + \frac{\eta|\boldsymbol{J}|^2}{\rho} \tag{2.14}$$

where the current density $\boldsymbol{J}$ is obtained as follows according to the Ampere's law:

$$\boldsymbol{J} = \frac{1}{\mu_0}\nabla \times \boldsymbol{B} \tag{2.15}$$

2.2.2 Equation of sate

The above governing equations are closed by the equation of state (EOS), which determines the fluid pressure as a function of density and internal energy. For accurate hydrodynamic simulations, the EOS model should be chosen as it yields accurate thermodynamic properties of a matter over a wide range of

relevant physical conditions.

The ideal gas EOS is the simplest EOS and can be easily and quickly incorporated in MHD simulations despite its restrictions on the valid physical conditions:

$$P = (\Upsilon - 1)\rho u \tag{2.16}$$

where $\Upsilon = \mathrm{C}_P / C_V$ is the adiabatic index, C_V is the specific heat at constant volume, and C_P is the specific heat at constant pressure.

Various EOS models that are practically applicable to real materials have been developed based on fundamental thermodynamic and statistical physics, such as the chemical equilibrium model of Saha equation (M. N. Saha, 1920; D. –K. Kim and I. Kim, 2003) and the Thomas–Fermi theory of quotidian equation of state (QEOS) (A. Kemp et al., 1998). In this study, the SPH-MHD model has been configured to utilize a tabulated form of EOS in order to enable the utilization of various EOS suitable for interpretation problems. More details on this content are covered in Chapter 3.

2.3 SPH-MHD model development

2.3.1 SPH formulation for resistive MHD

Applying the SPH formulation for the differential operator described in section 2.1.3, the set of resistive MHD governing equations consisting of continuity equation, momentum equation, induction equation, energy equation, and equation

of states is expressed as follows:

$$\boldsymbol{\rho}_i = m_i \sum_j W_{ij} \tag{2.17}$$

$$\frac{d\boldsymbol{v_i}}{dt} = \sum_j m_j \left(\frac{\overleftrightarrow{\boldsymbol{M}_i}}{\rho_i^2} + \frac{\overleftrightarrow{\boldsymbol{M}_j}}{\rho_j^2} \right) \cdot \nabla_i W_{ij} \tag{2.18}$$

$$\frac{d\boldsymbol{B_i}}{dt} = \frac{1}{\rho_i} \sum_j m_j \left(\boldsymbol{B}_i \boldsymbol{v}_{ij} - \boldsymbol{v}_{ij} \boldsymbol{B}_i \right) \cdot \nabla_i W_{ij} + \left(\frac{d\boldsymbol{B_i}}{dt} \right)_{non-ideal} \tag{2.19}$$

$$\frac{du_i}{dt} = \frac{1}{2} \sum_j m_j \left(\frac{P_i}{\rho_i^2} + \frac{P_j}{\rho_j^2} \right) \boldsymbol{v}_{ij} \cdot \nabla_i W_{ij} + \frac{1}{\rho_i} \eta \boldsymbol{J}_i^2 \tag{2.20}$$

$$P_i = P(u_i, \rho_i) \tag{2.21}$$

where $\overleftrightarrow{\boldsymbol{M}} = \boldsymbol{BB} - (\boldsymbol{B}^2/2 + P)\overleftrightarrow{I}$ is the Maxwell stress tensor, $\boldsymbol{v}_{ij} = \boldsymbol{v}_i - \boldsymbol{v}_j$ is the relative velocity between two particles, and $W_{ij} = W(\boldsymbol{r}_i - \boldsymbol{r}_j, h)$ denotes the kernel function. For this implementation, a unit for the magnetic field is used that normalizes the permeability μ_0 to 1 in the same way as some previous MHD studies.

2.3.2 Numerical techniques applied in the SPH-MHD model

The SPH simulation for pinch plasma has various features that threaten the numerical stability and numerical accuracy. In this section, several characteristics of pinch plasma that cause inaccurate SPH calculation are discussed, and numerical treatment techniques applied for controlling these incorrections are introduced.

① $\nabla\cdot\boldsymbol{B}$ Correction term

According to Gauss's law for magnetism, magnetic monopoles cannot exist, so the magnetic field line is always a closed curve, and then, $\nabla\cdot\boldsymbol{B}$ is always zero. However, in the numerical MHD simulation, $\nabla\cdot\boldsymbol{B}$ is not accurately zero because of numerical noise. This violation of the divergence constraint causes severe stability problems.

The problem of dealing with these $\nabla\cdot\boldsymbol{B}$ constraints is not an inherent problem of the SPH methodology. As noted by Toth (2000), in the case of Eulerian-based numerical MHD codes, three schemes are mainly used: Harten's TVD, van Leer's TVD-MUSCL, or Yee's TVD Lax–Friedrich scheme to deal with these $\nabla\cdot\boldsymbol{B}$ constraints (G.Toth, 1998). The approach of Børve (2007), commonly utilized in the SPH field, explicitly negates the effect of the non-vanishing $\nabla\cdot B$ by adding a corrective term in Eq. (2.23) to the momentum equation. The SPH-MHD model developed in this study also incorporates this method.

$$\left(\frac{D\boldsymbol{v}}{Dt}\right)_{\nabla\cdot\boldsymbol{B}\ correction} = -\boldsymbol{B}_i \sum_j m_j \left(\frac{\boldsymbol{B}_i}{\rho_i^2} + \frac{\boldsymbol{B}_j}{\rho_j^2}\right) \cdot \nabla W_{ij} \tag{2.23}$$

② Artificial dissipation term

In early shock simulation studies, it was recognized that a shock wave accompanied by a sharp velocity discontinuity boundary caused inaccurate calculations during numerical simulations. In more detail, a shock wave is not a true discontinuity, but a very narrow transition zone whose thickness is only a few molecular mean-free paths. Because the size of the computational domain

used in most numerical schemes is not small enough, this short transition length can lead to inaccurate calculations in numerical codes. Some investigators were able to make the transition zone thick enough to resolve computationally by introducing an unphysical viscosity, called 'artificial viscosity' (W.F Noh et al., 1998; M. L. Wilkins, 1980). Various types of ‘artificial viscosity' have been proposed and developed in various numerical schemes over the past several decades. In this study, an artificial viscosity form commonly utilized in the SPH methodology is employed to address the occurrence of discontinuous boundaries during plasma compression. The employed artificial viscosity is an improved version of the one introduced by Monaghan & Gingold (1983).

$$\left(\frac{d\boldsymbol{v}_i}{dt}\right)_{diss} = -\sum_j m_j \Pi_{ij} \nabla_i W_{ij}$$

$$\Pi_{ij} = \begin{cases} \dfrac{-\alpha \overline{c_{ij}} \phi_{ij} + \beta \phi_{ij}^{\,2}}{\overline{\rho_{ij}}} & if \ \left(\boldsymbol{v}_{ij} \cdot \boldsymbol{r}_{ij} < 0\right) \\ 0 & if \ \left(\boldsymbol{v}_{ij} \cdot \boldsymbol{r}_{ij} \geq 0\right) \end{cases} \quad where \ \phi_{ij} \qquad (2.24)$$

$$= \frac{h_{ij} \ \boldsymbol{v}_{ij} \cdot \boldsymbol{r}_{ij}}{\left|\boldsymbol{r}_{ij}\right|^2 + \varphi^2}$$

Here, α and β are constants that are typically set at approximately 1.0, and $\varphi = 0.1h_{ij}$ is applied to prevent numerical divergences. In this case, $\overline{\rho_{ij}}$ and $\overline{c_{ij}}$ denote the mean value of the density and the speed of sound between particle i and j.

Since the viscosity coefficient Π_{ij} is symmetric with particles i and j, the viscous force between any pair of interacting particles also will be symmetric

along the line joining the particles. Hence linear momentum and angular momentum are still preserved. However, there is a problem that the total energy is not conserved due to energy loss caused by the artificial viscous term. To conserve the total energy, the work done needs to be compensated for against the viscous force, as shown below:

$$\left(\frac{Du}{Dt}\right)_{diss} = \frac{1}{2}\sum_j m_j \Pi_{ij} \boldsymbol{v}_{ij} \cdot \nabla_i W_{ij} \tag{2.25}$$

In MHD simulations, shocks can lead to discontinuities in the magnetic field, which induce numerical instability. To address this issue, artificial resistivity can be introduced, which is similar to artificial viscosity. This approach is commonly used in SPH. This study employes the artificial resistivity proposed by Price (2012), which helps stabilize the simulation when magnetic field discontinuities caused by shocks are present.

$$\left(\frac{d\boldsymbol{B}_i}{dt}\right)_{diss} = \rho_i \sum_j m_j \frac{\alpha_B v_{sig}^B}{2\overline{\rho_{ij}}^2} (\boldsymbol{B}_i - \boldsymbol{B}_j) \hat{\boldsymbol{r}}_{\boldsymbol{ij}} \cdot \nabla W_{ij} \tag{2.26}$$

where v_{sig}^B is the averaged Alfvén speed, $\hat{\boldsymbol{r}}_{\boldsymbol{ij}}$ is the unit vector in the $\boldsymbol{r}_{\boldsymbol{ij}}$, and α_B is the artificial resistivity coefficient set using the switch described in Tricco and Price (2013):

$$\alpha_B = \min\left(\frac{h|\nabla \boldsymbol{B}|}{|\boldsymbol{B}|}, \quad 1 \right) \tag{2.27}$$

③ Adaptive SPH method

In SPH simulations involving shockwaves with expansion, the spacing between particles rapidly changes, leading to "particle inconsistency," where the smoothing length does not comprise a sufficient number of particles. This problem can significantly affect the accuracy of SPH simulations (M. B. Liu and G. R. Liu, 2006). Various methods have been proposed to solve this particle inconsistency problem (J. Bonet and S. Kulasegaram, 2000; G. R. Johnson et al., 1996; P. W. Randles and L. D. Libersky, 1996), such as adaptive SPH (ASPH). ASPH is a method wherein a different smoothing length is applied to each particle to increase the accuracy of the SPH approximation in a situation where the spacing between particles changes, as shown in **Figure 2.2**. In the pinch plasma simulation, this ASPH application is essential because the distance between particles can rapidly increase or decrease due to explosion or implosion due to shock.

This study utilizes the ASPH method proposed by Owen (1998) to adjust the smoothing length of particles based on the number of particles in the original search range. If excess particles are present, the search range is narrowed to improve the computational speed. On the other hand, if too few particles are present, the search range is widened to solve the "particle inconsistency" problem, which can reduce the calculation accuracy. This process is performed by defining and using a reference density value:

$$\rho_{ref} = m\left(\frac{\sigma}{h}\right)^{d} \tag{2.28}$$

where d is the system dimension, and σ is a parameter specifying the smoothing

length in units of average particle spacing $(m/\rho)^{1/d}$, which is 1.2 herein. To select an appropriate smoothing length, the below iteration process is used to compare the reference density with the density derived from the SPH calculation. This iteration is repeated until the difference between the two smoothing lengths $h_k$and h_{k+1} converges below a specified criterion. The smoothing length h is updated in each iteration using the following formula:

$$h_{k+1} = h_k - \frac{\partial h_k}{\partial \rho} \frac{\rho_{ref}(h_k) - \rho(h_k)}{1 - \frac{\partial h_k}{\partial \rho} \sum_j m_j \frac{\partial W(h_k)}{\partial h_k}} \tag{2.29}$$

$$\frac{\partial h}{\partial \rho} = -\frac{1}{d}\frac{h}{\rho} \tag{2.30}$$

$$\frac{\partial W}{\partial h} = -\frac{r}{h}\nabla W - \frac{d}{h}W \tag{2.31}$$

To account for the changes in the smoothing length, a smoothing length gradient correction factor Ω is used, which is determined as follows:

$$\Omega = 1 - \frac{\partial h_k}{\partial \rho} \sum_j m_j \frac{\partial W(h_k)}{\partial h_k} \tag{2.32}$$

The variable Ω is applied to Eqs. (2.17)–(2.20) to account for the changes in the smoothing length. This correction is important as it ensures the calculation accuracy with varying smoothing length. For example, if ASPH is applied to Eq. (2.18), it is converted into the following equation:

$$\frac{d\boldsymbol{v_i}}{dt} = \sum_j m_j \left(\frac{\overleftrightarrow{\boldsymbol{M}_i}}{\Omega_i \rho_i^2} \cdot \nabla_i W_{ij} + \frac{\overleftrightarrow{\boldsymbol{M}_j}}{\Omega_j \rho_j^2} \cdot \nabla_j W_{ij} \right) \tag{2.33}$$

2.3.3 Non-ideal MHD terms of the SPH method

To calculate the non-ideal MHD term in the resistive MHD, the current density $\boldsymbol{J}$ needs to be accurately calculated first. Previous SPMHD studies calculated the current density via the following two ways:

$$\boldsymbol{J}_i = -\frac{1}{\rho_i} \sum_j m_j (\boldsymbol{B}_i - \boldsymbol{B}_j) \times \nabla_i W_{ij} \tag{2.34}$$

$$\boldsymbol{J}_i = -\rho_i \sum_j m_j \left(\frac{\boldsymbol{B}_i}{\rho_i^2} + \frac{\boldsymbol{B}_j}{\rho_j^2} \right) \times \nabla_i W_{ij} \tag{2.35}$$

For example, to obtain the current density, Wurster (2016) used the difference operator of Eq. (2.34) and Price (2010) used the symmetric operator of Eq. (2.35). In this study, a more suitable SPH formulation is employed to calculate the current density under pinch plasma conditions, wherein a large magnetic field discontinuity can occur. A detailed explanation of this process is provided in next section along with suitable example problems.

The flexibility of SPH approximations enables a diverse set of constructions, and the SPH formula for the non-ideal MHD term has also been used in various ways. For instance, Bonafede et al. (2011) and Tsukamoto et al. (2013) addressed this term by directly taking the second derivatives of the magnetic field. Wurster (2014) computed this term by applying a curl calculation to the current density.

However, it is unclear which of the two approaches has numerical advantages when using SPH for simulations involving the non-ideal MHD term. Further investigation and comparison between the two methods are necessary to determine the approach that is more accurate or efficient in practical applications. Basically, the first derivative of the current density is computed first using symmetric and difference operators. An "inter-particle" formulation that is known to be effective between two phases with significantly different properties is adopted. Consequently, the SPH model developed in this study is equipped with four types of derivatives for the non-ideal MHD term (i.e., symmetric, difference, Laplacian, and inter-particle), and the derivative forms are summarized in **Table 2.3**.

2.4 SPH-MHD model implementation

2.4.1 Algorithm of developed SPH-MHD model

Figure 2.3 shows a basic algorithm of the developed SPH-MHD model. The model is based on the existing SPH-based hydrodynamics code, SOPHIA (Y. B. Jo et al., 2019), but it includes some additional calculations that are essential for analyzing pinch plasmas. First, the initial positions, properties, and conditions of each particle. Then, the nearest-neighboring particle search process is conducted for each particle based on each position. Then, the density and current density of each particle are estimated using the Eq. (2.21) and Eq. (3.34). After that, the pressure is calculated for each particle through the EOS table in the form of Eq. (2.21). After the pressure is calculated, Then, the change in velocity, density,

magnetic field, and internal energy of each particle is calculated according to the governing equations represented by Eq. (2.18) – (2.20). Then, all physics quantities including each particle's velocity and position are updated. Upon updating the particle positions, the neighbor particle searching (NNPS) process is repeated based on the new position. This iterative calculation persists until the termination condition is met.

2.4.2 Nearest Neighbor Particle Search (NNPS)

In general, the neighbor particle searching (NNPS) process is known to be the most time-consuming step in SPH calculations. To estimate the properties of a specific particle, denoted as particle 'i,' it is necessary to search for neighboring particles within a kernel radius, which in this study is set as three times the initial particle distance. Under these conditions, the number of neighboring particles is approximately 25 to 30 in 2D simulations and 100 to 120 in 3D simulations. The intuitive approach for neighbor particle searching involves searching all particles throughout the entire computational domain based on the particle distance condition. However, this NNPS algorithm is inefficient and computationally demanding, scaling proportionally to the number of particles ($\sim N^2$). Therefore, for high-resolution analysis, an efficient NNPS algorithm is essential, and in this study, a constant grid-based NNPS algorithm is adopted. Regularly spaced grids are allocated across the entire computational domain, depending on user specifications. Subsequently, only particles belonging to the grid adjacent to the center grid, where the particle of interest 'i' resides, are searched, and neighboring particles 'j' within the search range are selected. This NNPS algorithm enables

efficient searching calculations and significantly reduces computation time (Xia, 2016).

2.4.3 Time integration

In this study, a modified predictor–corrector time-stepping scheme proposed by Gomez-Gesteira (2012) is applied. The predictor–corrector scheme divides the time integration into two steps. First, the prediction step extrapolates the physical variables (e.g., velocity, density, magnetic field, and internal energy) as follows:

$$\boldsymbol{v}^{p}_{t+\frac{\Delta t}{2}} = \boldsymbol{v}_t + \frac{\Delta t}{2}\left(\frac{d\boldsymbol{v}}{dt}\right)_t \tag{2.36}$$

$$\rho^{p}_{t+\frac{\Delta t}{2}} = \rho_t + \frac{\Delta t}{2}\left(\frac{d\rho}{dt}\right)_t \tag{2.37}$$

$$\boldsymbol{B}^{p}_{t+\frac{\Delta t}{2}} = \boldsymbol{B}_t + \frac{\Delta t}{2}\left(\frac{d\boldsymbol{B}}{dt}\right)_t \tag{2.38}$$

$$u^{p}_{t+\frac{\Delta t}{2}} = u_t + \frac{\Delta t}{2}\left(\frac{du}{dt}\right)_t \tag{2.39}$$

where Δt is the time step, and the superscript p denotes “predictor.” The time derivatives of velocity, density, magnetic field, and internal energy are evaluated by solving Eqs. (2.36)–(2.39) using the predicted values. Then, the field variables are re-calculated over the entire time step using the updated time derivatives in the correction step.

$$\boldsymbol{v}^{c}_{t+\Delta t} = \boldsymbol{v}_t + \Delta t\left(\frac{d\boldsymbol{v}}{dt}\right)_{t+\frac{\Delta t}{2}} \tag{2.40}$$

$$\rho_{t+\Delta t}^{c} = \rho_t + \Delta t \left(\frac{d\rho}{dt}\right)_{t+\frac{\Delta t}{2}} \tag{2.41}$$

$$\boldsymbol{B}_{t+\Delta t}^{c} = \boldsymbol{B}_t + \Delta t \left(\frac{dB}{dt}\right)_{t+\frac{\Delta t}{2}} \tag{2.42}$$

$$u_{t+\Delta t}^{c} = u_t + \Delta t \left(\frac{du}{dt}\right)_{t+\frac{\Delta t}{2}} \tag{2.43}$$

where the superscript c denotes "corrector." These corrected values become the initial values for the next time step.

2.4.4 GPU Parallelization

The numerical expressions used in the SPH method are highly linear, and calculations of particles are performed explicitly. Therefore, there is no problem even if the calculations of particles are conducted independently. As a result, the SPH method is optimized for GPU (Graphics Processing Unit) parallelization, which is crucial for reducing SPH interpolation errors by utilizing a large number of SPH particles and achieving high-resolution simulations.

The GPU is composed of multiple blocks, with each block containing several threads. All particles involved in the simulation are allocated to individual threads, enabling simultaneous parallel calculations across all threads. The calculation for the neighboring particle is performed within each thread using a loop, and the summation operation of the estimated values is carried out through parallel reduction. In this study, the SPH-MHD model is parallelized based on the NVIDIA

CUDA architecture (GPGPU), improving computational efficiency.

2.5 Model verification

In this section, the results of the simulation performed to verify the constructed SPH model are explained. The simulations using the implemented models are conducted for three benchmark cases: (1) Brio and Wu shock tube (ideal MHD), (2) resistive MHD shock tube simulation, and (3) magnetized Noh Z-pinch problem, and summarized in **Table 2.4**. All simulation results are compared with the simulation results and analytical solutions of some reference Eulerian code.

2.5.1 Brio and Wu shock tube simulations

The Brio & Wu shock tube problem generalizes the classic hydraulics Sod shock tube to MHD (M. Brio and C. C. Wu, 1988). In the Brio & Wu shock tube, the right and left states are initialized to different values. The components of the anti-parallel magnetic field on the two sides of the initial discontinuity lead to four waves, i.e., fast rarefaction wave, slow compound wave, slow shock wave, and fast shock wave, resulting in complex property distribution. In this test, the left and right states are initialized as $(\rho, v_x, v_y, B_x, B_y, P)$ = [1,0,0,0.75,1,1] and [0.125,0,0,0.75,−1,0.1], respectively. This example tests whether the model can accurately represent the shocks, rarefactions, contact discontinuities, and compound structures of MHD. Thus, it has been widely used as a benchmark problem to validate ideal MHD calculations (J. J. Monaghan, R. A. Gingold, 1983; S. Vanaverbeke et al., 2009). In this study, the "1.5D" Brio & Wu shock tube problem (i.e., 1D but with 2D magnetic and velocity fields) is analyzed with 1000

particles in the range $x \in [-0.5, 0.5]$. Four physical quantities (i.e., density, pressure, x,y-directional velocity, internal energy, and magnetic field) of the Brio & Wu shock problem are obtained through the constructed SPH model. **Figure 2.4** depicts the simulation results of the Brio & Wu shock tube at 0.1 s. In the figure, the black dots represent the physical quantities of all the particles and the red lines represent the numerical solution obtained using a proven Riemann solver (D.S. Balsara, 1998). The results show that the proposed SPH model yields numerically accurate simulations of the ideal MHD problem.

The effect of numerical techniques such as the correction terms to satisfy the $\nabla \cdot \boldsymbol{B}$ constraints and artificial dissipation terms to handle shocks through this problem is also verified. **Figure 2.5** shows that the applied numerical treatments are effective. First, whether the numerical instability caused by the $\nabla \cdot \boldsymbol{B}$ constraint can be effectively controlled is determined by introducing Eq.(2.23). The comparison of **Figure 2.5** (a) and (b) shows that various numerical errors are removed after the introduction of the correction term. **Figure 2.5**(c) displays the calculation results obtained after the incorporation of the artificial resistivity of Eq. (21) into the result of **Figure 2.5**(b). As shown in the figure, the dissipation term for the magnetic field partially controls the existing numerical instability.

2.5.2 Resistive MHD shock tube simulations

In actual pinch plasma simulations, the effect of plasma resistivity on plasma behavior must be considered. Therefore, the resistive term is added in the induction and energy equations. Additionally, the current density needs to be calculated to derive these resistive terms. To verify the accurate functioning of

these added terms, resistive MHD shock tube simulations are performed, wherein plasma resistivity is distributed in the ideal MHD shock tube, which is represented by the Brio & Wu shock tube. The left and right states are initialized as (ρ^L, v_x^L, P^L) = [1, 0, 1] and (ρ^R, v_x^R, P^R) = [0.125, 0, 0.1], respectively. To calculate the exact peak value of the current density, the initial magnetic field is applied as the following steep sigmoidal function:

$$\boldsymbol{B}_{\mathrm{y}} = \frac{0.5 - 0.5\ \exp(x/d)}{1 + \exp(x/d)} \tag{2.44}$$

where d is the value that determines the magnetic field gradient in the steep region, which is 0.0005 m herein. In this case, the peak value of current density is 500. Here, high resolution is required to capture the sharp current density peak. Therefore, a sensitivity analysis of the particle resolution is performed, and the result is shown in **Figure 2.6**. Subsequently, simulations are conducted with the particle spacing of 0.00025 m, which is four times closer than that in the Brio & Wu shock tube.

Fig. 5 presents the SPH current density profiles of the resistive MHD shock tube simulations. As described in **Section 2.3.3**, two types of SPH discretization are used to compute the current density. **Figure 2.7** clearly shows that the current peak at x = 0 is underestimated when the symmetric operator is employed. This tendency becomes more pronounced as the discontinuity of the magnetic field at the interface becomes steeper. **Figure 2.8** displays the current profile when d is 0.00005 m. In this case, the difference operator well captures the current peak and the symmetric operator yields an additional non-physical current peak. These

results emphasize the importance of using the correct discretization method to obtain accurate results at the discontinuous interface of pinch plasmas.

To accurately model the non-ideal MHD effects in the simulation, investigations are conducted to identify the appropriate SPH discretization form for this term. The plasma resistivity is simulated as a function of density ($\eta = 10^{-3}\rho^{-6}$), and the results are evaluated via comparison with the data from a reference Euler code (PLUTO code (Mignone et al., 2007). As mentioned in Section III.E, four types of SPH formulations are considered for the non-ideal MHD term. **Figure 2.9**(a) displays the time derivative of the magnetic field obtained using each of the four discretization methods at t = 0.0002 s. Non-physical oscillations can be observed in the time derivative of the magnetic field for some SPH discretization types. These oscillations grow over time and have a significant negative impact on the computational accuracy. **Figure 2.9**(b) shows the difference between the simulation results and the reference data. The figure shows that the inter-particle type of non-ideal MHD term is the most effective in reducing the current density noise stemming from the discretization of the initial large magnetic field discontinuity. This methodology is expected to be effective for various types of pinch plasmas accompanied by discontinuous magnetic fields and resistivities.

2.5.3 Magnetized Noh Z-pinch Problem

Velikovich (2011) proposed the magnetized Noh problem as an example for verifying the pinch plasma analysis ability. The Noh problem has been used for many years to verify codes designed to deal with implosions such as in inertial

confinement fusion to investigate the hydrodynamic component of MHD codes. The extension of this classic gas dynamics Noh problem to the electromagnetic problem is known as the magnetized Noh Z-pinch problem. The operation of a Z-pinch is very simple. A current driven through the cylindrical column of the plasma causes the material to rapidly compress axially through the $\boldsymbol{J} \times \boldsymbol{B}$ force. To simulate this multi-dimensional pinch plasma, an initial plasma state is considered that is defined as a function of r, which represents the distance from the central point. The initial properties of plasma including the density (ρ), radial velocity ($\mathrm{v_r}$), toroidal magnetic field (B_ϕ), and plasma pressure (P) are $\rho = 3.1831 \times 10^{-5}\mathrm{r}^2\ \mathrm{g/cm^3}$, $\mathrm{v_r} = -3.24101 \times 10^7\ \mathrm{cm}/s$, $\mathrm{B}_\phi = 6.35584 \times 10^8\mathrm{r}$ gauss, and $P = \beta \times \mathrm{B}_\phi^2$, respectively. Here, the ratio of the plasma pressure and magnetic pressure (β) is $8\pi \times 10^{-6}$.

The SPH particles are arranged with spacings of 0.01 cm on a 2D plane in the range of −3 cm < x < 3 cm and −3 cm < y < 3 cm. For the boundary condition, an approach similar to that in a previous study is followed (A. L. Velikovich et al., 2011). Specifically, the outermost 10 layers of particles are assigned as boundary particles, and the physical properties of the last layer of plasma particles are copied. Accordingly, the ρ, $\mathrm{v_r}$, B_ϕ, and P values of the boundary particle satisfy the zero gradient condition at $\mathrm{r_{out}}$ $(= 3\ \mathrm{cm})$. This approach is effective because the boundary is far enough from the center of the plasma, preventing significant influence on the internal dynamics within the first 30 ns of the simulation.

During the simulation, the plasma undergoes temporal evolution, which leads to a significant change in its properties. Therefore, a crucial criterion for determining the effectiveness of the MHD code for simulating multi-dimensional

pinch plasma is its ability to reproduce the self-similar solution for this problem. To evaluate the accuracy of developed model, the problem is simulated and the density, velocity, and pressure of the plasma at 30 ns are analyzed.

Through this 2D simulation, the application effect of the introduced ASPH method is confirmed. **Figure 2.10** (b) presents the comparison of the analytic solution and the simulation result obtained through the SPH moel before the ASPH application. As shown in the figure, the peak value of physical properties in the compressed region significantly differs from that in the analytic solution. Two factors contribute to this error. First, the smoothing length at the center point is too large. As shown in **Figure 2.11** (a), the strong compression by the magnetic field causes the particles to gather with a high number density at the central point. If ASPH is not applied, the initial smoothing length used in the simulation may be too large to yield a high number density. Previous studies using Eulerian codes have reported that physical variables are underestimated when the mesh is not dense enough in the magnetized Noh problem. Similarly, in the SPH simulations, an excessively wide smoothing length relative to the particle number density results in the underestimation of physical quantities at the peak point (A. L. Velikovich et al., 2011). Second, the tensile instability during the simulation is observed. As shown in **Figure 2.11** (a), during the simulation of the magnetized Noh problem, the particles aggregated and assembled in the same direction. These particle arrangements are known to cause tensile instability, which is accompanied with significant numerical errors in SPH simulations (T. A. Shelkovenko et al., 2018). For the above problems, significant improvement has been achieved through the application of the ASPH method. **Figure 2.10** (c) shows the comparison between the simulation results with the ASPH method

applied and the analytic solution for the magnetized Noh problem. The figure shows that the accuracy of the SPH model greatly improves in the compression problems after the application of the ASPH method. In addition, as shown in **Figure 2.11** (b), the existing tensile instability is successfully removed due to the application of the ASPH method.

Table 2.1. Conditions of kernel function

Condition	**Mathematical Expression**
Unity Condition	$\int_{\Omega} W(r,h)d\Omega = 1$
Symmetry Condition	$\mathrm{W}(r,h) = \mathrm{W}(-r,h)$
Delta-function Approximation	$\lim_{h\to 0} W(r,h) = \delta(r)$
Compact Support Condition	$W(r,h) = 0$ for $\lvert r\rvert > \kappa h$
Positive Condition	$W(r,h) \geq 0$ for any r
Monotonic Decrease Condition	$W'(r,h) < 0$

Table 2.2. Types of kernel functions

Kernel function	**Formulation**
Gaussian	$W(R,\mathrm{h}) = \begin{cases} \frac{1}{(\pi^{0.5}h)} e^{-R^2} & for\ 1D \\ \frac{1}{(\pi^{0.5}h)^2} e^{-R^2} & for\ 2D \\ \frac{1}{(\pi^{0.5}h)^3} e^{-R^2} & for\ 3D \end{cases}$
Quartic	$W(R,\mathrm{h}) = \begin{cases} \frac{1}{h}\left(\frac{2}{3} - \frac{9}{8}R^2 + \frac{19}{24}R^3 - \frac{5}{32}R^4\right) & for\ 1D \\ \frac{15}{7\pi h^2}\left(\frac{2}{3} - \frac{9}{8}R^2 + \frac{19}{24}R^3 - \frac{5}{32}R^4\right) & for\ 2D \\ \frac{315}{208\pi h^3}\left(\frac{2}{3} - \frac{9}{8}R^2 + \frac{19}{24}R^3 - \frac{5}{32}R^4\right) & for\ 3D \end{cases}$
Wendland C2	$W(R^*,h) = \begin{cases} \frac{5}{4(2h)}(1-R^*)^3(1+3R^*) & for\ 1D \\ \frac{7}{\pi(2h)^2}(1-R^*)^4(1+4R^*) & for\ 2D \\ \frac{21}{2\pi(2h)^3}(1-R^*)^4(1+4R^*) & for\ 3D \end{cases}$

Table 2.3. Four types of SPH derivatives for the non-ideal MHD term

SPH discretization	SPH Formulation
Symmetric	$\left(\frac{d\boldsymbol{B}}{dt}\right)_{non-ideal} = \rho_i \sum_j m_j \left(\frac{\eta_i \boldsymbol{J}_i}{\rho_i^2} + \frac{\eta_j \boldsymbol{J}_j}{\rho_j^2}\right) \times \nabla_i W_{ij}$
Difference	$\left(\frac{d\boldsymbol{B}}{dt}\right)_{non-ideal} = -\frac{1}{\rho_i} \sum_j m_j (\eta_i \boldsymbol{J}_i - \eta_j \boldsymbol{J}_j) \times \nabla_i W_{ij}$
Laplacian	$\left(\frac{d\boldsymbol{B}}{dt}\right)_{non-ideal} = \sum_j \frac{4\eta_i \eta_j}{\eta_i + \eta_j} \frac{m_j}{\rho_j} (\boldsymbol{B}_i - \boldsymbol{B}_j) \frac{\boldsymbol{r}_{ij} \cdot \nabla_i W_{ij}}{\lvert \boldsymbol{r}_{ij} \rvert^2}$
Inter-particle	$\left(\frac{d\boldsymbol{B}}{dt}\right)_{non-ideal} = -\frac{\rho_i}{m_i} \sum_j \left(\frac{m_i^2}{\rho_i^2} + \frac{m_j^2}{\rho_j^2}\right) \frac{\rho_i \eta_j \boldsymbol{J}_j + \rho_j \eta_i \boldsymbol{J}_i}{\rho_i + \rho_j} \times \nabla_i W_{ij}$

Table 2.4. Benchmark problems for developed SPH-MHD model verification

Benchmark problems	Assessment objectives
➢ **Hydrodynamic shock problem** - *Slab detonation* - *SOD shock tube*	- Shock capturing (artificial viscosity) - Large discontinuity
➢ **Ideal MHD problem** - *Brio&Wu shock tube*	- MHD calculation ($\nabla \cdot \boldsymbol{B}$ correction) - Shock capturing (artificial resistivity)
➢ **Resistive MHD problem** - *Resistive MHD shock tube (w/ constant resistivity)* - *Resistive MHD shock tube (w/ varying resistivity)*	- Resistive MHD calculation (Non-ideal MHD term) - Large discontinuity
➢ **Pinch plasma problem** - *Magnetized Noh Z-pinch problem*	- Shock capturing - Large discontinuity - Multi-dimension calculation (ASPH)

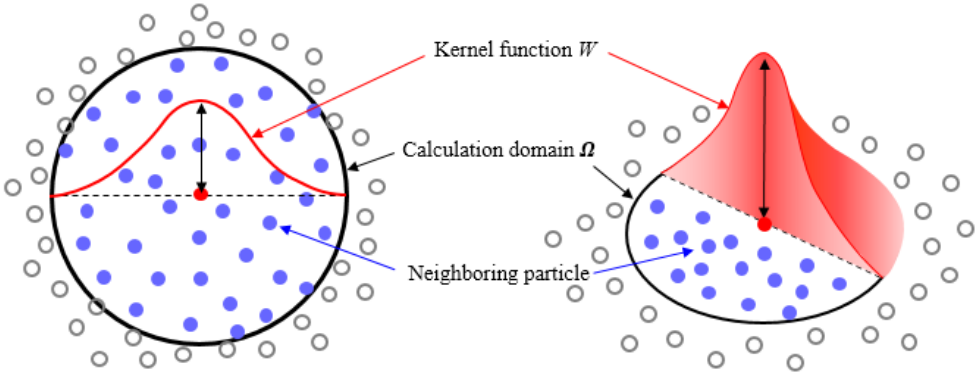

Figure 2.1. Particle System of Smoothed Particle Hydrodynamics (SPH)

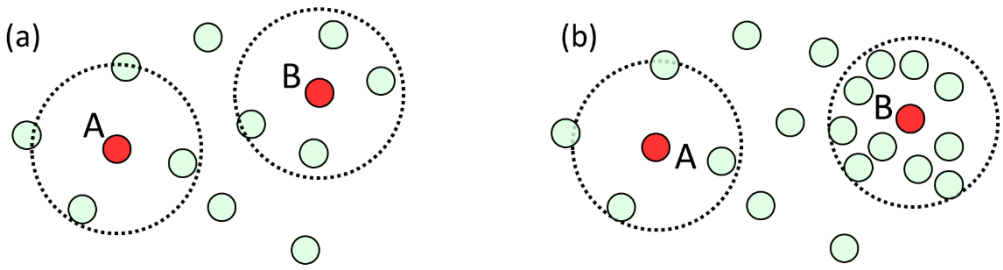

Figure 2.2. Schematic diagram of particle kernel radius in non-uniform particle distribution (a) before applying ASPH, and (b) after applying ASPH

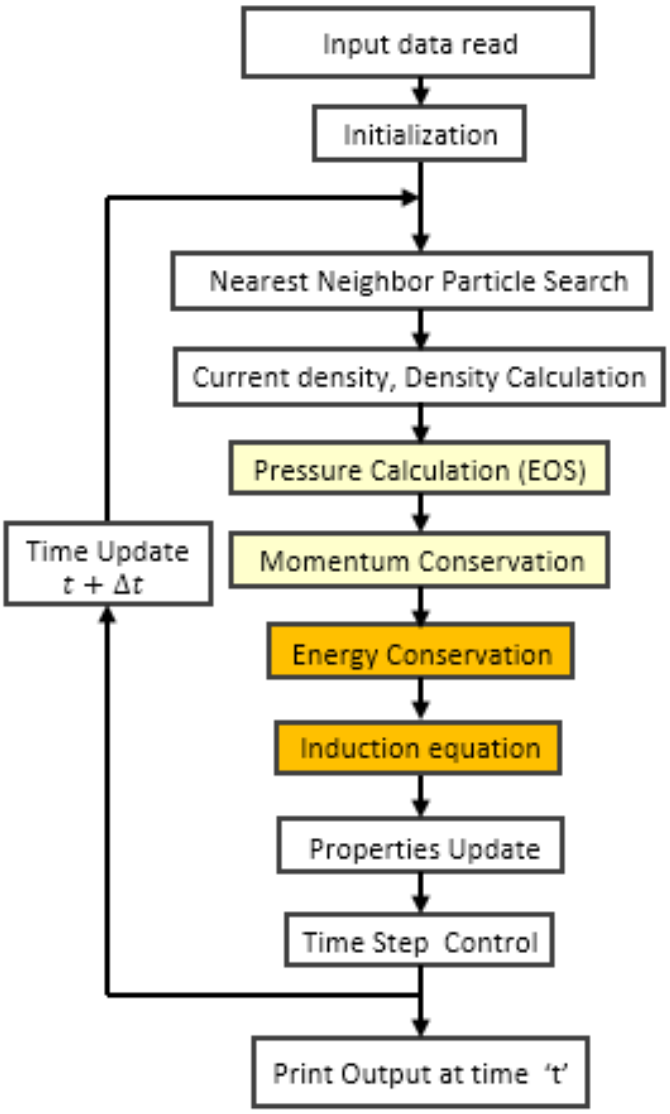

Figure 2.3. Simplified algorithm of SOPHIA-MHD model

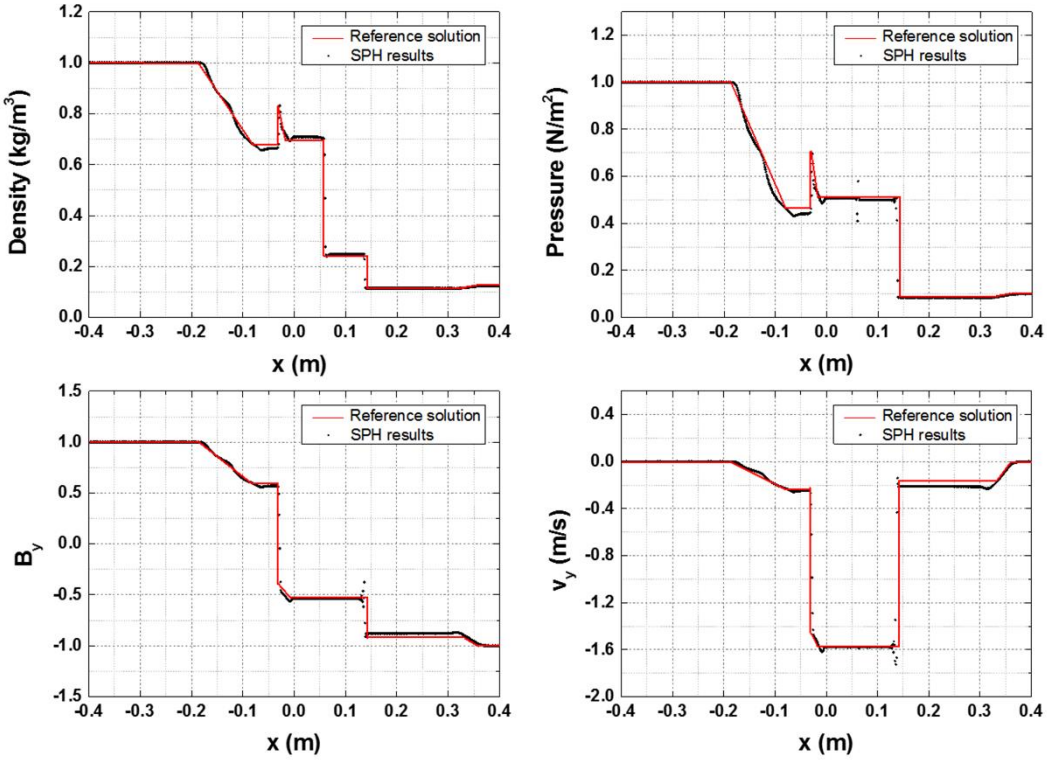

Figure 2.4. Biro&Wu shock tube simulation results

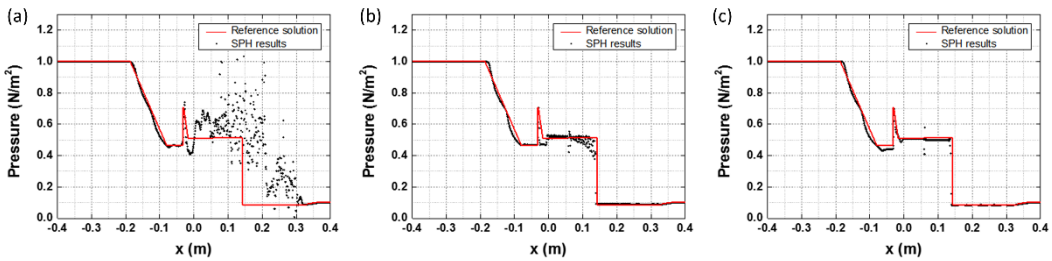

Figure 2.5. The pressure field profiles of Brio&Wu shock tube simulation (b) after applying the $\nabla \cdot B$ correction term, and (c) artificial resistivity term.

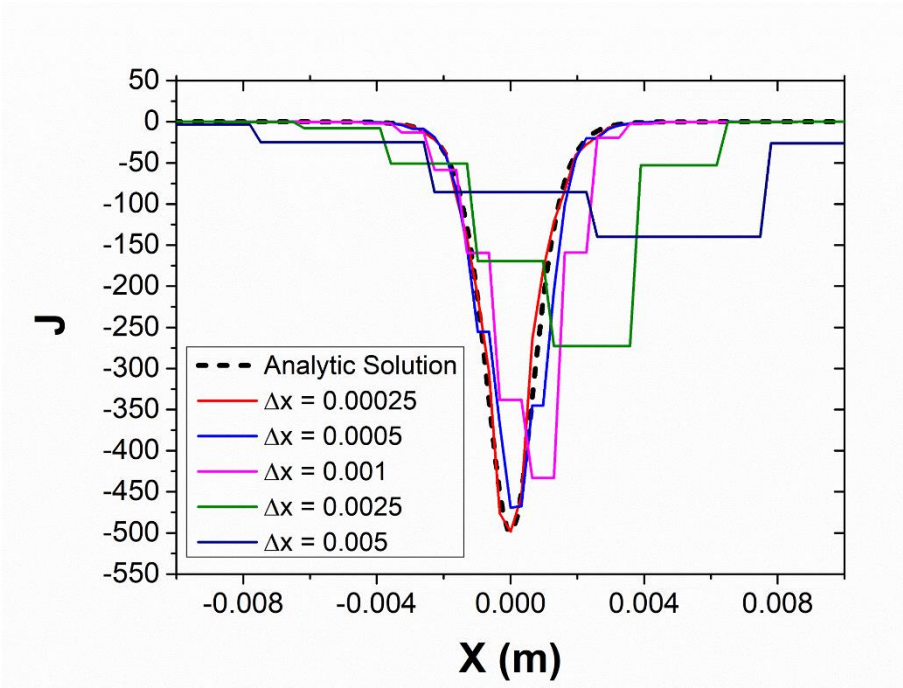

Figure 2.6. Effects of particle resolution on SPH current density profiles in resistive MHD shock tube simulation. This sensitivity analysis of particle resolution demonstrates that a sufficiently high resolution is required to capture the sharp peak in current density.

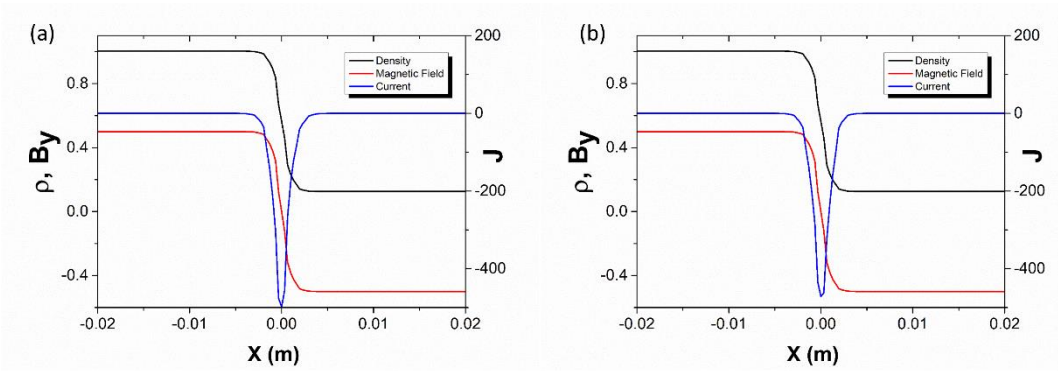

Figure 2.7. SPH current density profiles of resistive MHD shock tube simulation using (a) difference operator, and (b) symmetric operator. (d = 0.0005)

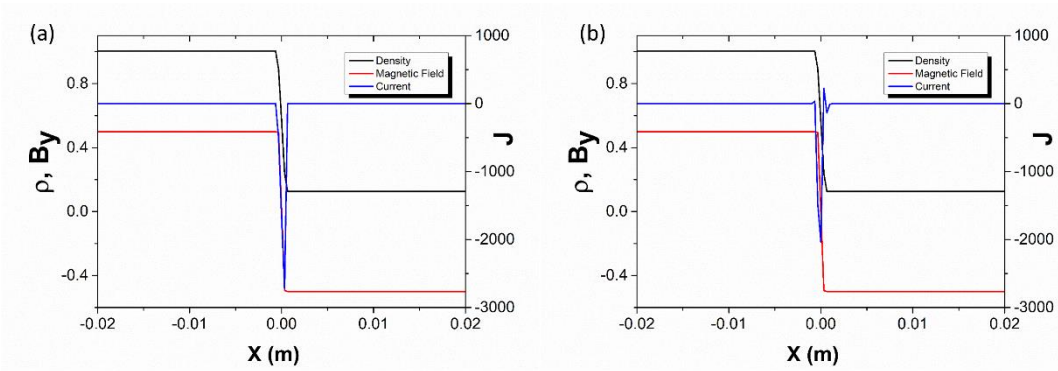

Figure 2.8. SPH current density profiles of resistive MHD shock tube simulation using (a) difference operator, and (b) symmetric operator. (d = 0.00005)

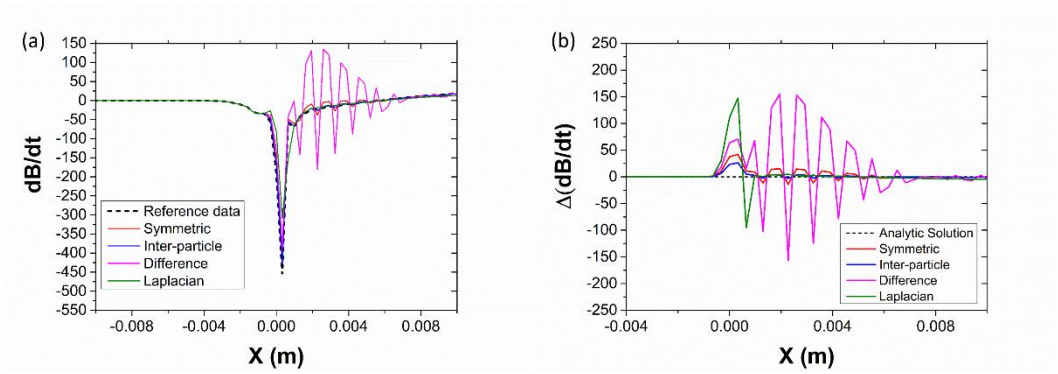

Figure 2.9. (a) Time derivative of magnetic field according to the SPH discretization and (b) deviation from reference data at t=0.0002 sec.

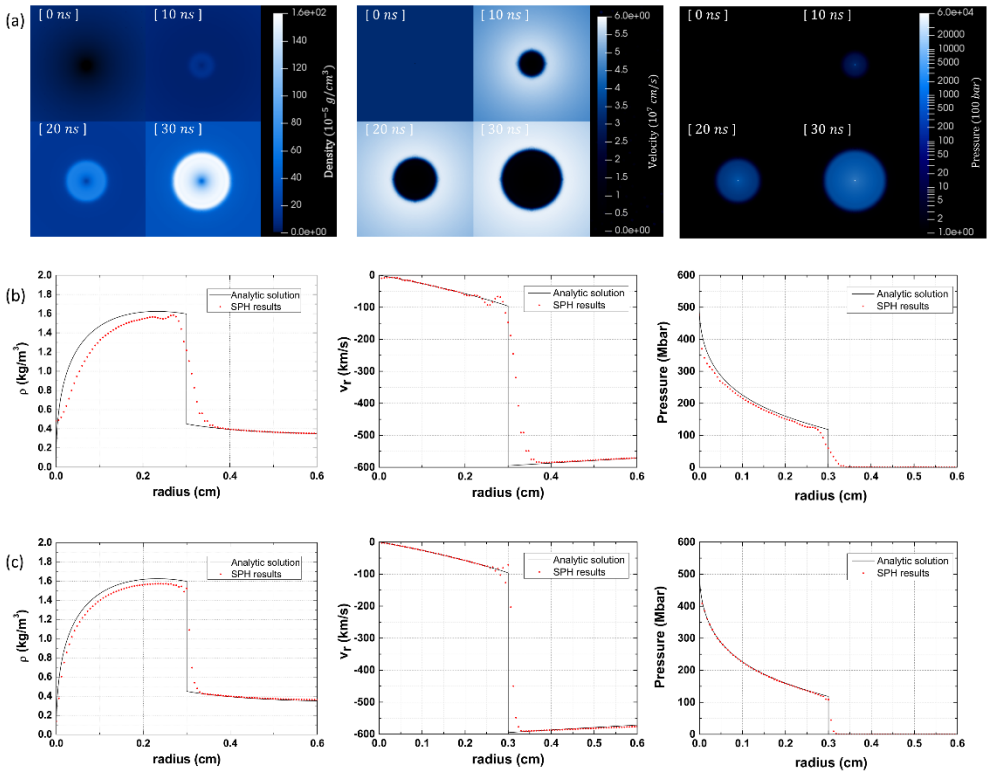

Figure 2.10. Magnetized Noh simulation results from 2-dimensional SPH model: (a) the time evolution of density, velocity, and pressure distributions, and the profiles of the variables (b) before and (c) after applying ASPH. The solid curve is the self-similar solution at 30 ns to the magnetized Noh problem.

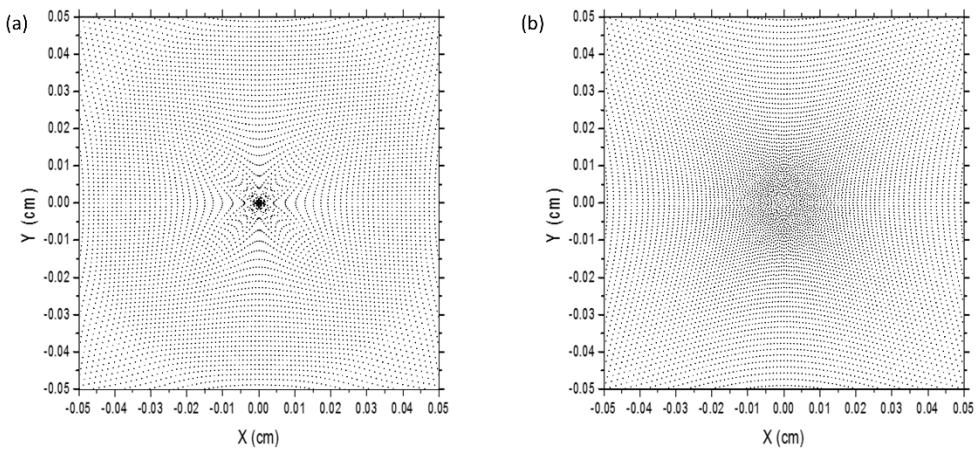

Figure 2.11. Particle arrangement in magnetized Noh simulation (a) before and (b) after applying ASPH

Chapter 3

Physics Model for X-pinch Simulation

3.1 Challenges for X-pinch simulations

In this section, the main challenges encountered in the simulation of X-pinch phenomena are summarized. Each challenge addresses a specific aspect of the simulation process and highlights the modifications made to the code to overcome these challenges. Firstly, in the high-temperature conditions of pinch plasma, the insufficiency of electron-ion collisions renders the one-temperature model inadequate. To address this, the code has been expanded to incorporate a two-temperature equation, allowing for the separation of electron and ion energies. Secondly, selecting an appropriate Equation of State (EOS) is crucial for accurately capturing the non-ideal characteristics of plasma under extreme conditions. The code incorporates a Thomas-Fermi model-based EOS, specifically tailored to describe the non-ideal effects of High-Energy-Density Plasmas (HEDP). Thirdly, an accurate plasma transport model is essential for reflecting the energy transport and electromagnetic properties of pinch plasma. Desjarlais' modified model, which addresses overestimated ionization in low-density regions, has been integrated into the code to provide a more realistic representation of plasma dynamics. Lastly, given the presence of both optically thin and optically thick regions in X-pinch phenomena, an appropriate radiation

model is necessary to cover the entire plasma column. The code employs the flux-limited diffusion model, enabling comprehensive radiative calculations throughout the X-pinch region. By addressing these challenges, the enhanced simulation code offers a more accurate and comprehensive representation of X-pinch phenomena, facilitating a deeper understanding of the complex physics involved in HEDP.

3.2 SPH governing equations for X-pinch simulations

Understanding transport processes in plasma, including particle diffusion, heat conduction across magnetic fields, electric resistivity, and energy transfer, is essential for addressing critical challenges in X-pinch research. However, the existing SOPHIA-MHD code developed in Chapter 2 lacks a comprehensive model that incorporates these processes, requiring enhancements to enable effective X-pinch simulation. This section provides a detailed description of the MHD model specifically designed for X-pinch simulation and derives its SPH formulation.

3.2.1 Single-fluid two-temerature model

The most commonly employed model for dense pinch plasmas is the one-fluid, two-temperature Magnetohydrodynamics (MHD) model developed by Braginskii (1963) and Rosenbluth (1956). This model combines the individual fluid equations governing ions and electrons while incorporating several approximations (Krall and Trivelpiece, 1973; T. G. Cowling, 1957; and others) to

derive the one-fluid MHD equations. In some cases, equations describing the ionization kinetics or radiative energy transport should be added to the system. The model includes equations of mass and charge continuity, the equation of motion, and the energy equations for ions and electrons as follow:

$$\frac{d\rho}{dt} + \rho(\nabla \cdot \boldsymbol{v}) = 0 \tag{3.1}$$

$$\frac{d\boldsymbol{v}}{dt} = \frac{1}{\rho}\nabla \cdot \left(\frac{\boldsymbol{B} \otimes \boldsymbol{B}}{\mu_0} - \left(\frac{|\boldsymbol{B}|^2}{2\mu_0} + P\right)\overleftrightarrow{I}\right) \tag{3.2}$$

$$\frac{du_{ion}}{dt} = -\frac{P_{ion}}{\rho}(\nabla \cdot \boldsymbol{v}) + \frac{1}{\rho}\nabla \cdot \boldsymbol{q}_{ion} + \frac{1}{\rho}\Delta_{ie} \tag{3.3}$$

$$\frac{du_{elec}}{dt} = -\frac{P_{elec}}{\rho}(\nabla \cdot \boldsymbol{v}) + \frac{1}{\rho}\nabla \cdot \boldsymbol{q}_{elec} + \frac{\eta|\boldsymbol{J}|^2}{\rho} - \mathrm{Q_{rad}} + \frac{1}{\rho}\Delta_{ei} \tag{3.4}$$

Here, $\rho, \boldsymbol{v}, P, u$ represent the mass density, velocity, pressure, and specific internal energy respectively. Radiation effects are included through a radiation losses sink term $\mathrm{Q_{rad}}$ and Ohmic heating is given by the source term $\eta|\boldsymbol{J}|^2$, where η is the resistivity. The ion and electron thermal fluxes are given, respectively, by $\boldsymbol{q}_{ion} = -k_{ion}\nabla T_{ion}$ and $\boldsymbol{q}_{elec} = -k_{elec}\nabla T_{elec}$, where k is the thermal conductivity. In the single-fluid approximation, the plasma momentum is primarily influenced by the ions, neglecting electron inertia. So, the flow is described by a single momentum equation, as given in Eq. (3.2). As mentioned in the previous section, the HED plasma regime presents challenges when assuming equal temperatures for electrons and ions. In such cases, the energy of electrons and ions is treated separately, considering their significant mass ratio. Consequently, two distinct energy equations are obtained: Eq. (3.3) for ions and

Eq. (3.4) for electrons. The energy equations for electrons and ions are coupled through the electron-ion energy exchange term Δ_{ei} $(= -\Delta_{ie})$. The calculation of this term, along with Q_{rad}, is discussed in detail in the subsequent section.

In cases involving very high currents or particle beams interacting with dense pinch plasmas, where relativistic effects are significant, the single-fluid approximation proves inadequate. Instead, a two-fluid model of a non-neutral plasma should be utilized (Meierovich and Sukhorukov, 1975; Solov'ev, 1984). When dealing with low-density plasmas found in RFPs or EXTRAP, alternative fluid models such as the perpendicular MHD model and the CGL model may be more relevant. Some stability issues cannot be adequately addressed using a fluid model alone and necessitate a kinetic approach. However, for dense pinch plasmas, Eq. (3.1)-(3.4) has been known to be valid in most cases (M. A. Liberman et al., 1999). Notably, the validity of the single-fluid assumption under the X-pinch condition was confirmed by Byun(2022) through a comparison of collision time (τ_{ei}), collisional mean free path (λ_{mfp}) and pulse duration, plasma length scales. **Figure 3.1** illustrates that the contours of τ_{ei} and λ_{mfp} are predominantly small in comparison to the pulse duration (100 ns to a few μs) and plasma length scales (mm). Therefore, the single-fluid model was utilized for the X-pinch simulation in this study.

3.2.2 Electron-ion exchange model

The electron-ion exchange term Δ_{ei} is expressed as Eq. (3.5) from the temperature difference of electron and ion (R. Ramis et al., 2012).

$$\Delta_{ei} = \frac{3m_e}{m_i^2} Z_{eff} \nu_{ei} \, (T_e - T_i) \tag{3.5}$$

where ν_{ei} is the electron-ion collision frequency, $m_{e,i}$ are the electron and ion mass respectively, and Z^* is the average ionization level. To determine the collision frequency of the plasma, the Spitzer model has traditionally been employed (L. Spitzer and R. Härm, 1953).

$$\nu_{Spitzer} = \frac{4}{3} (2\pi)^{\frac{1}{2}} \frac{Z^* \, e^4 m_e n_e}{(m_e k_B T_e)^{3/2}} ln(\Lambda) \tag{3.6}$$

where e denotes the unit charge, n_e reperesents the electron density, $ln(\Lambda)$ is the Coulomb logarithm, and k_B stands for the Boltzmann constant. However, this model yields significantly different values from reality, particularly in the low-temperature region (M. Basko, 1997). Given that the X-pinch phenomenon encompasses low-temperature regions where the Spitzer model is not valid, it is necessary to obtain a collision frequency ν_{ei}, that is applicable over a wide temperature range, including the cold, solid state of plasma. Within this specific region, the dependence of collision frequency on electron temperature diminishes due to the electrons being in a degenerate state. Instead, the interaction between electrons and phonons or lattice vibrations becomes the governing factor for the collision frequency. This electron-phonon model accurately characterizes the behavior of solid states at low temperatures below the melting point. Under conditions of a cold solid state, denoted as $v_{\mathrm{F}} \ll c$ and $\hbar\omega_{\mathrm{pi}} \ll k_B T_{ion}$, this model is known to be able to approximated using the following form:

$$\nu_{elec-phonon} \approx 2k_s \frac{e^2 k_B T_i}{\hbar^2 v_F} \tag{3.7}$$

Here, c is the speed of light, ω_{pi} the ion plasma frequency, and v_{F} the Fermi velocity v_{F} $(= \hbar(3\pi^2 n_e)^{\frac{1}{3}}/m_e)$. k_s is a numerical constant, for which the value 13 is given in the previous study (D.G. Yakovlev and V.A. Urpin, 1980). Finally, the classical Spitzer collision frequency is combined with the electron-phonon collision frequency through interpolation as shown in Eq. (3.8).

$$\nu_{ei}^{-1} = \nu_{Spitzer}^{-1} + \nu_{elec-phonon}^{-1} \tag{3.8}$$

The energy exchange term in Eq. (3.5) can be accurately calculated in the low-temperature region by utilizing the collision frequency in Eq. (3.8). **Figure 3.2** shows a schematic diagram of collision frequency as a function of temperature.

3.2.3 Radiation model

It is necessary to include an accurate radiation model to reproduce the actual physical phenomena that occur in the X-pinch, such as neck breaking. In many previous X-pinch simulation studies, the optically thin assumption was employed. In this case, the radiation power generated in the plasma can be calculated from the radiation losses that occur through electronic transitions (Byun et al., 2022; Koundourakis, 2020; Skoulakis 2022). However, the actual X-pinch plasma exhibits a complex nature, encompassing regions that are both optically thin and

optically thick. Therefore, it is necessary to utilize a radiation model capable of addressing both aspects of the phenomenon. The radiation model employed in this study is the flux-limited diffusion model. This model is an extension of the diffusion approximation radiation model, which estimates thermal spread by assuming equal magnitude of radiation in multiple directions. A full description of the flux-limited diffusion approximation is given by Turner & Stone (2001). This section provides a summary of the main points.

In this model, additional transport equations are necessary for the calculation of radiation energy. The derivation of radiation transport equations assumes local thermal equilibrium (LTE) and utilizes the diffusion approximation and gray approximations. In this context, the formulas for computing the specific internal energy of electrons and specific radiation energy (ξ) are proposed as follows (S. Whitehouse, 2004):

$$\frac{du_{elec}}{dt} = -\frac{P_{elec}}{\rho}(\nabla \cdot \boldsymbol{v}) + \frac{1}{\rho}\nabla \cdot \boldsymbol{q}_{elec} + \frac{\eta|\boldsymbol{J}|^2}{\rho} + c\kappa_p\left(E_{rad} - \frac{4\sigma_B}{c}T_{elec}^4\right) \tag{3.9}$$

$$\frac{d(\xi_{rad})}{dt} = -\frac{1}{\rho}\nabla \cdot \boldsymbol{F} - \frac{1}{\rho}\nabla v : \overleftrightarrow{\boldsymbol{P}} - c\kappa_p\left(E_{rad} - \frac{4\sigma_B}{c}T_{elec}^4\right) \tag{3.10}$$

where $\boldsymbol{F}$ denotes the radiative flux, c is the speed of light, κ_p is the planck mean opacity, σ_B is the Stefan-Boltzmann constant with a value of 5.67×10^{-8} $\mathrm{W/m^2}K^4$ and E_{rad} is the radiation energy density ($E_{rad} = \rho\xi_{rad}$). At this stage, considering that u_{elec} is significantly larger than ξ_{rad} under most conditions, Eq. (3.11) is derived by combining Eq. (3.9) and Eq. (3.10):

$$\frac{d}{dt}(u_{elec}) \approx -\frac{P_{elec}}{\rho}(\nabla \cdot \boldsymbol{v}) + \frac{1}{\rho}\nabla \cdot \boldsymbol{q}_{elec} + \frac{\eta|\boldsymbol{J}|^2}{\rho} - \frac{1}{\rho}\nabla v : \overleftrightarrow{\boldsymbol{P}} - \frac{1}{\rho}\nabla \cdot \boldsymbol{F} \quad (3.11)$$

Here, assuming the radiation temperature is equal to the electron temperature, Eq. (3.11) can be solved without the need for a separate calculation of the radiation energy density. Although these assumptions are not strictly based on physical principles, it was employed in this study due to their advantage of ensuring calculation stability and allowing for radiation calculations within the hydrodynamic time step. In the diffusion approximation model, $\boldsymbol{F}$ expressed using the rosseland mean opacity κ_R as

$$\boldsymbol{F} = -\frac{c}{3\rho\kappa_R}\nabla E_{rad} \quad (3.12)$$

This expression provides accurate flux in regions with high optical thickness. However, the diffusion equation, while easy to solve, becomes inaccurate in regions with low optical thickness and a large energy density gradient. In optically thin regions, where $\rho\kappa_R$ approaches zero, the flux tends to approach infinity, whereas in reality, the magnitude of the flux should not exceed the speed of light times the energy density $(\boldsymbol{F} \leq c|E_{rad}|)$. To address this issue, the flux-limited diffusion approach imposes a limitation on the flux in optically thin environments, ensuring that it always satisfies the aforementioned inequality. To this end, Levermore & Pomraning (1981) formulated the radiation flux using below Fick's law of diffusion:

$$\boldsymbol{F} = -\frac{c\lambda}{\rho\kappa_R}\nabla E_{rad} \tag{3.13}$$

The dimensionless function λ is called the flux limiter. To determine the flux limiter, an appropriate expression needs to be selected. In this study, the flux limiter proposed by Levermore & Pomraning is chosen.

$$\lambda(R) = \frac{2 + R}{6 + 3R + R^2} \tag{3.14}$$

where R is the dimensionless quantity $R = |\nabla E_{rad}|/\rho\kappa_R E_{rad}$. In the optically thin limit,

$$\lim_{R\to\infty} \lambda(R) = \frac{1}{R} \tag{3.15}$$

resulting in a flux magnitude approaching $|\boldsymbol{F}| = c|\nabla E_{rad}|/\rho\kappa_R R = cE_{rad}$. In the optically thick limit,

$$\lim_{R\to 0} \lambda(R) = \frac{1}{3} \tag{3.16}$$

leading to the flux value given by Eq (3.11). Several alternative forms of flux limiter have been developed to provide more realistic performance in various problem scenarios (Turner and Stone, 2001).

3.2.4 SPH Governing equations

Through the preceding discussions, the SPH governing equations outlined in Chapter 2, which include the conservation of mass, momentum, induction, specific ion and electron internal energy equation are extended and employed in X-pinch simulations.

$$\boldsymbol{\rho}_i = m_i \sum_j W_{ij} \tag{3.17}$$

$$\frac{d\boldsymbol{v_i}}{dt} = \sum_j m_j \left(\frac{\overleftrightarrow{\boldsymbol{M}_i}}{\rho_i^2} + \frac{\overleftrightarrow{\boldsymbol{M}_j}}{\rho_j^2} \right) \cdot \nabla_i W_{ij} \tag{3.18}$$

$$\begin{aligned} \frac{d\boldsymbol{B_i}}{dt} = \frac{1}{\rho_i} \sum_j m_j \left(\boldsymbol{B}_i \boldsymbol{v}_{ij} - \boldsymbol{v}_{ij} \boldsymbol{B}_i \right) \cdot \nabla_i W_{ij} \\ - \frac{\rho_i}{m_i} \sum_j \left(\frac{m_i^2}{\rho_i^2} + \frac{m_j^2}{\rho_j^2} \right) \frac{\rho_i \eta_i \boldsymbol{J}_i + \rho_j \eta_j \boldsymbol{J}_j}{\rho_i + \rho_j} \times \nabla_i W_{ij} \end{aligned} \tag{3.19}$$

$$\begin{aligned} \frac{du_i^{ion}}{dt} = \frac{1}{2} \sum_j m_j \left(\frac{P_i^{ion}}{\rho_i^2} + \frac{P_j^{ion}}{\rho_j^2} \right) \boldsymbol{v}_{ij} \cdot \nabla_i W_{ij} - \frac{3 m_{elec}}{m_{ion}^2} Z^* \, \nu_{ei} \, (T_i^{elec} - T_i^{ion}) \\ + \sum_{j=1}^{N} \frac{4 k_i^{ion} k_j^{ion}}{k_i^{ion} + k_j^{ion}} \frac{m_j}{\rho_i} \left(T_i^{ion} - T_j^{ion} \right) \frac{\boldsymbol{r}_{ij} \cdot \nabla W_{ij}}{\left| \boldsymbol{r}_{ij} \right|^2} \end{aligned} \tag{3.20}$$

$$\begin{aligned} \frac{du_i^{elec}}{dt} = \frac{1}{2} \sum_j m_j \left(\frac{P_i^{elec}}{\rho_i^2} + \frac{P_j^{elec}}{\rho_j^2} \right) \boldsymbol{v}_{ij} \cdot \nabla_i W_{ij} + \frac{1}{\rho_i} \eta_i \boldsymbol{J}_i^2 \\ - \frac{4 \sigma_B}{c \rho} T_i^{elec^4} (\nabla \cdot \boldsymbol{v})_i f_i + \frac{3 m_{elec}}{m_{ion}^2} Z^* \, \nu_{ei} \left(T_i^{elec} - T_i^{ion} \right) \\ + \sum_{j=1}^{N} \frac{4 k_i^{elec} k_j^{elec}}{k_i^{elec} + k_j^{elec}} \frac{m_j}{\rho_i} \left(T_i^{elec} - T_j^{elec} \right) \frac{\boldsymbol{r}_{ij} \cdot \nabla W_{ij}}{\left| \boldsymbol{r}_{ij} \right|^2} \\ + \sum_{j=1}^{N} \frac{4 \mu_i \ \mu_j}{\mu_i \ + \mu_j} \frac{m_j}{\rho_i} \left(T_i^{elec} - T_j^{elec} \right) \frac{\boldsymbol{r}_{ij} \cdot \nabla W_{ij}}{\left| \boldsymbol{r}_{ij} \right|^2} \end{aligned} \tag{3.21}$$

Here, u^{ion} and u^{elec} are specific ion/electron internal energy, k^{ion} and k^{elec} are ion/electron thermal conductivity, $T^{ion}$and T^{elec} are ion/electron temperature, Z^* and ν_{ei} ars the average ionization level and collision frequency of i particle, and μ is the radiation thermal conductivity obtained from Eq. (3.13) and expressed as

$$\mu_i = \frac{16\lambda_i \sigma_B}{\rho_i \kappa_{R\_i}} T_i^{elec^3} \tag{3.22}$$

f is the Eddington factor expressed as the flux-limiter λ.

$$f_i = \lambda_i + \lambda_i^2 \left[\frac{\left|\nabla T_i^{elec}\right|}{\rho_i \kappa_{R\_i} \; T_i^{elec}} \right] \tag{3.23}$$

In Eq. (3.20) and Eq. (3.21), heat transfer terms due to radiation and conduction involve second-order spatial derivatives. Direct computation of second-order derivatives using standard SPH techniques is well known to be sensitive to particle disorder and may lead to unstable integration. To overcome this difficulty, Cleary & Monaghan (1999) proposed a reformulation of the second-order derivative as a first-order derivative using a Taylor series expansion. A detailed description of this reformulation can be found in the work of Jubelgas (2004).

3.3 Physical property model

The solution of Eqs. (3.17) – (3.21) necessitates detailed plasma property values spanning a wide range of temperatures and densities. These values were

derived using suitable material property models, including EOS, plasma transport, and radiation models, and organized in tabular format. In this section, a comprehensive explanation of the detailed physics model used to obtain each material property is provided. Furthermore, the subsequent section presents an algorithm of the entire code, including how the obtained plasma properties are effectively incorporated.

3.3.1 Plasma ionization balance model

The average ion charge state (Z^*) implies the ionization degree on each plasma state, and electron/ion densities (n_e, n_i) are determined from the ionization process. Accurate ionization calculations are crucial as they has a strong effect on many plasma properties found in Eqs. (3.17) to (3.21). To achieve precise modeling of plasma dynamics, an accurate calculation of the ionization degree is essential. A variety of methods have been adopted to determine the degree of ionization for strongly coupled plasmas. Two representative approaches that can classify the various approximation methods are the Saha equation method (W. Ebeling et al., 1976) and the Thomas-Fermi (TF) statistical atomic model. In this study, the average degree of ionization for a dense plasma is calculated using the modified Lee-More model based on the TF method.

The Lee-More model has demonstrated its efficacy in determining the average properties of atomic systems, including the equation of state and degree of ionization. It also has been widely employed in various high-density physics problems. With the generic Lee-More model, the electron density is commonly

determined using a TF ionization model. This approach is advantageous due to its natural connection to TF model-based EOS and its ability to cover a wide range of densities and temperatures. However, the TF model fails to accurately capture the metal-insulator transition because it neglects atomic structure effects on ionization equilibrium. As a result, it overestimates the ionization level under low-density conditions, which are known to produce very low ionization levels. To overcome this limitation, this study employed a Desjarlais corrected model (2001) that combines the TF model with a single ionization Saha model, incorporating a pressure ionization correction. In this corrected model, the effective ionization calculation is done as Eq. (3.24).

$$Z_{eff} = {f_e}^{2/Z_{TF}^2} Z_{TF} + \left(1 - {f_e}^{2/Z_{TF}^2}\right) f_e \tag{3.24}$$

where f_e is the ionization level by simplified non-ideal Saha, and Z_{TF} is the ionization level by Thomas-Fermi approximation. The effective ionization level for copper was computed using Eq. (3.4). As a results, the Desjarlais corrected model offers a comprehensive approach that smoothly transitions from Thomas-Fermi to non-ideal Saha in regions where the ionization calculated from the non-ideal Saha model is significantly less than 1.0, as depicted in **Figure 3.4**.

3.3.2 Plasma transport model

The Spitzer and Braginskii formulas are commonly used for calculating plasma transport coefficients, but these models are only applicable to fully ionized non-

degenerate plasmas (Y. T. Lee et al., 1984). In the case of X-pinch plasma, non-ideal effects become significant. There are two common approaches for obtaining transport coefficients in these kinds of high-density plasmas. The first approach involves using tabular data, such as SESAME tables, which provide explicit plasma transport coefficients values. The second approach involves employing an implicit model with in-line calculations, such as the Lee & More model (1984).

In this study, a combination of these two approaches is used. First, the Lee & More model is improved to better account for the non-ideal plasma conditions in the X-pinch scenario. These improvements enable the derivation of various transport coefficients necessary for the X-pinch simulation. Following that, the derived coefficients are organized and transformed into a tabular format, representing them as functions of density and temperature. Finally, the resulting property table is directly utilized for calculations.

There are several improvements based on the Lee & More model to accurately describe non-ideal plasma behavior. Firstly, the corrected Coulomb logarithm is taken into account to incorporate the non-ideal effects in the metal-insulator state. Instead of using the classical Coulomb logarithm, $\ln(1 + 1.4\Lambda_m^2)^{1/2}$ is utilized (R. J. Zollweg and R. W. Libermann, 1987). In this case, Λ_m represents a modified form derived from the classical Coulomb logarithm value (Λ), which can be expressed as

$$\Lambda_m = \Lambda\left[1 + \left(\frac{a_i}{\lambda_D}\right)^2\right]^{1/2} \tag{3.25}$$

Here, a_i represents the inter-ionic distance, and λ_D corresponds to the Debye shielding length. The corrected ratio of the cutoff shielding length (b_{max}) to the impact parameter (b_0) in Coulomb collisions is considered to account for the dense plasma condition. Secondly, the inclusion of electron-neutral atom collisions is considered when calculating the electrical conductivity of the plasma. The electrical conductivity of a plasma medium is greatly influenced by the degree of ionization. In fully ionized plasma, the movement of electrons is primarily governed by Coulomb interactions with ions, whereas in weakly ionized plasma, collisions between electrons and neutral atoms play a significant role. For partially ionized plasma, the electrical conductivity (σ) can be represented by a simple model that strikes a balance between the fully and weakly ionized conditions (Kim, 2003).

$$\frac{1}{\sigma} = \frac{1}{\sigma_{e-i}} + \frac{1}{\sigma_{e-n}} \tag{3.26}$$

$$\sigma_{e-i} = \frac{1}{38}\frac{T_e^{3/2}}{Z_{eff}}\frac{\gamma_E}{\ln(1+1.4\Lambda_m^2)^{1/2}} \tag{3.27}$$

$$\sigma_{e-n} = \frac{n_e e^2}{m_e \nu_{e-n}} \tag{3.28}$$

where σ_{e-i} and σ_{e-n} represent the electrical conductivities associated with electron-ion and electron-neutral collisions, respectively. γ_E is the correction factor for electron-electron collisions, and ν_{e-n} is the mean electron-neutral collision frequency calculated using the Chapman-Enskog theory (R.J. Rosa et al., 1991). At this point, the Desjarlais modified model, introduced in the previous section, can be utilized to calculate Eq. (3.27). The impact of these improvements

on the electrical conductivity of copper is illustrated in **Figure 3.4**.

3.3.3 Plasma opacity model

Opacity is a quantity that determines the transport of radiation through matter and is important for various problems in physics and astronomy. In particular, calculating opacity in HED (High-Energy-Density) plasma is essential for understanding the energy transport by radiation within the plasma and its effects. It is known that quantum mechanical effects, such as degeneracy, impact opacity because plasma is compressed in high-energy-density plasma, and the distance between ions is at the Debye length level. Therefore, to calculate opacities, atomic data for numerous processes involving the absorption and scattering of radiation is required.

In this study, the Rosseland mean opacity of copper is calculated using the ATOMIC code (J. Colgan et al., 2016). ATOMIC is a multi-purpose plasma modeling code (Magee et al., 2004; Hakel et al., 2006; Fontes et al., 2015) that can be operated in LTE or non-LTE mode. It provides the necessary Rosseland mean opacity data for calculating Eq.(3.21) across the temperature range from 0.5 eV to 10 keV. In ATOMIC code, Rosseland mean opacity was defined as (Weiss et al., 2004) :

$$\kappa_R = \frac{\int_0^\infty \frac{1}{\kappa_\nu} n_\nu^3 \frac{\partial B_\nu}{\partial T} d\nu}{\int_0^\infty \frac{\partial B_\nu}{\partial T} d\nu} \tag{3.29}$$

where ν is the photon frequency, B_ν represents the Planck function (Huebner & Barfield, 2014), n_ν denotes the frequency-dependent refractive index defined by Armstrong et al. (2014), and κ_ν represents the frequency-dependent opacity. κ_ν encompasses several contributions that can be summarized as follows:

$$\kappa_\nu = \kappa_{BB} + \kappa_{FF} + \kappa_{SC} \tag{3.30}$$

Here, the sum of bound-bound (*BB*), bound-free (*BF*), free-free (*FF*), and scattering (*SC*) contributions is considered. The first three contributions involve a factor accounting for stimulated emission. For a detailed description of the calculations of each of these contributions, refer to J. Colgan (2016). The finally obtained copper opacity data can be found in **Figure 3.5**.

3.3.4 Algorithm of SOPHIA-X code

The SOPHIA-X code, based on the SPH governing equations discussed in the previous section, is computed in a specific order as illustrated in **Figure 3.6**. Developed as an enhancement of the SOPHIA-MHD code discussed in Chapter 2, the SOPHIA-X code is specifically tailored for X-pinch analysis. This section highlights the main improvements made to the code. Firsty, the following parts of the SOPHIA-MHD code are modified for X-pinch analysis: (1) reading the input data, (2) updating various plasma properties using the EOS table, (3) solving the momentum conservation equation, and (4) solving the induction

equation, (5) updating the physical properties over time. Additionally, to account for radiation effects, the energy conservation equation is separated into separate equations for ions and electrons. At this time, all tabulated plasma properties used are determined by the temperature and density of the plasma. Therefore, a process of updating the plasma temperature through the internal energy value updated in the energy conservation equation must be added.

$$\frac{dT}{dt} = \left(\frac{du}{dt} - \frac{\partial u}{\partial \rho}\ \frac{d\rho}{dt}\right)\left(\frac{\partial u}{\partial T}\right)^{-1} \tag{3.31}$$

$$T_i^{n+1} = T_i^n + \left(\frac{dT_i}{dt}\right)\Delta t \tag{3.32}$$

Finally, the temperature gradient is obtained and used for radiation calculation. This process is performed concurrently with the calculation of the momentum conservation.

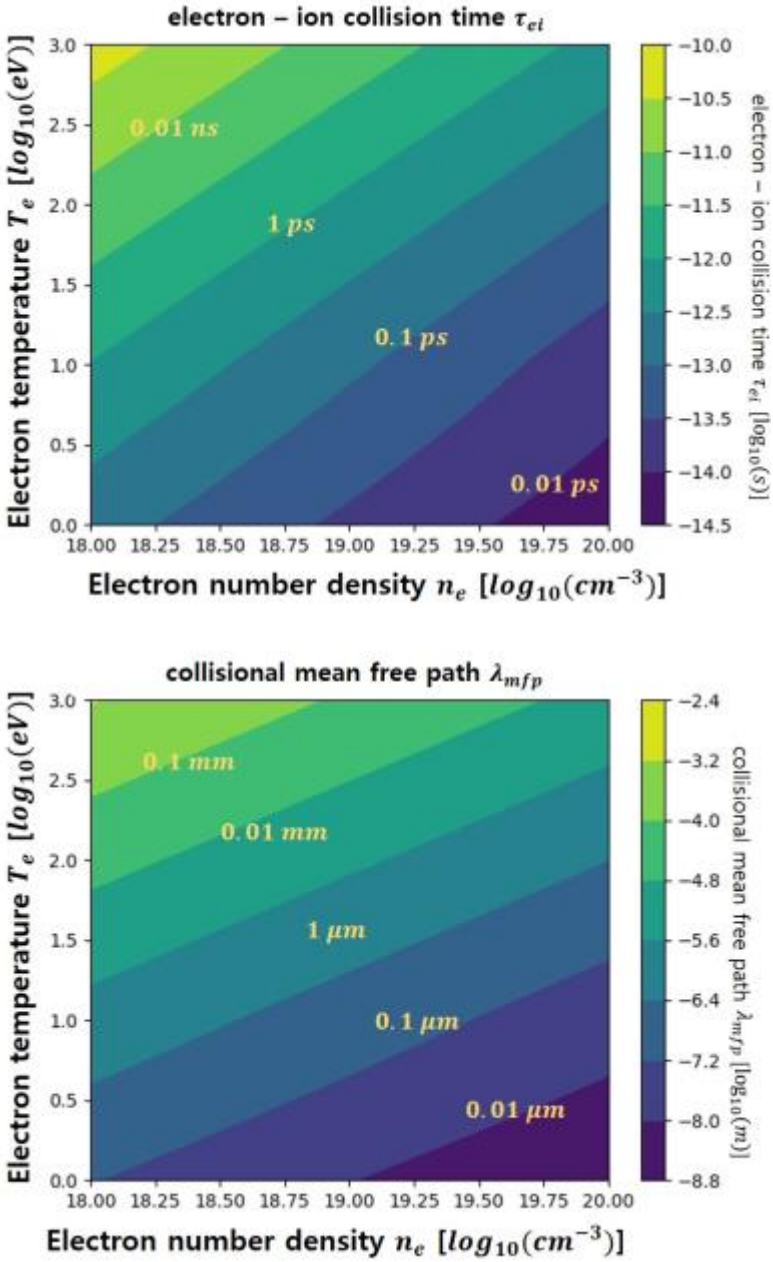

Figure 3.1. (Above) Electron and ion collision time τei and (Below) Collisional mean free path λ_{mfp} on the X-pinch plasma regime [Byun, 2022]. It indicates that the τ_{ei} and λ_{mfp} contours are primarily small compared to pulse duration.

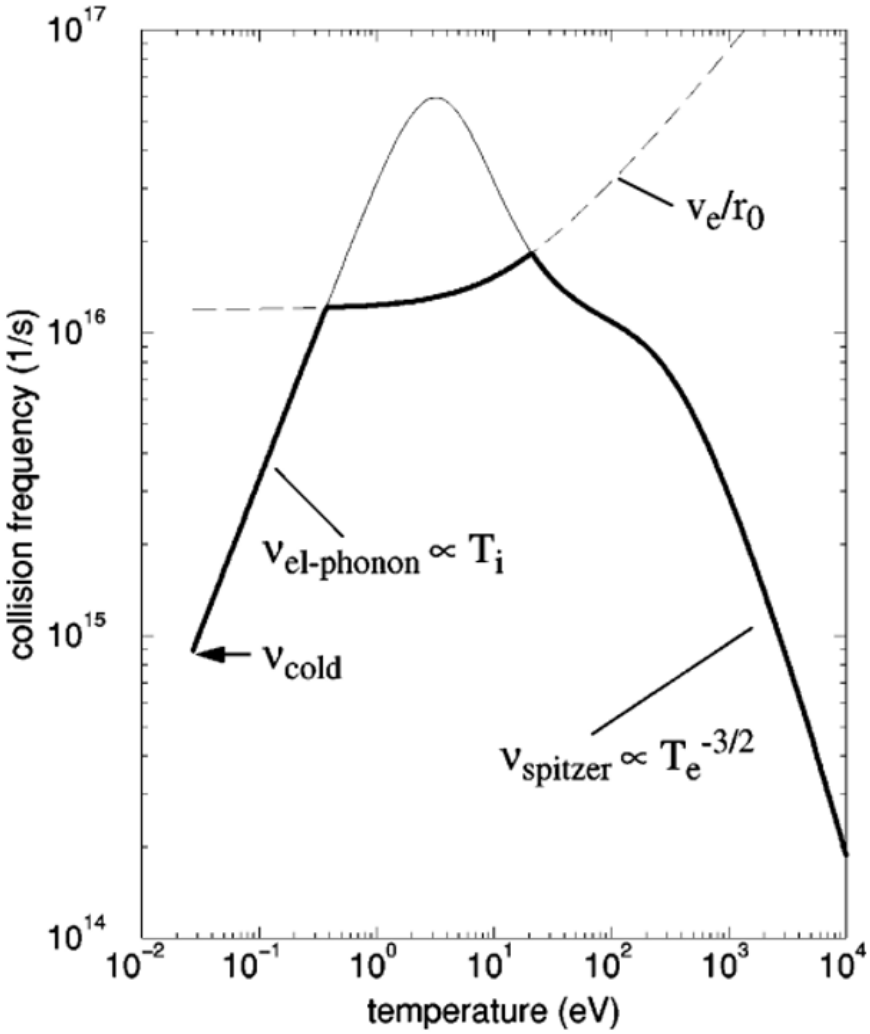

Figure 3.2. The schematic diagram for collision frequency as a function of the temperature $T_e = T_i$ (thick solid line). The thin solid line is the result of the interpolation Eq. (3.8), and the dashed line is the upper limit of the collision frequency given by the requirement $\lambda > r_0$ [Eidmann, 2000].

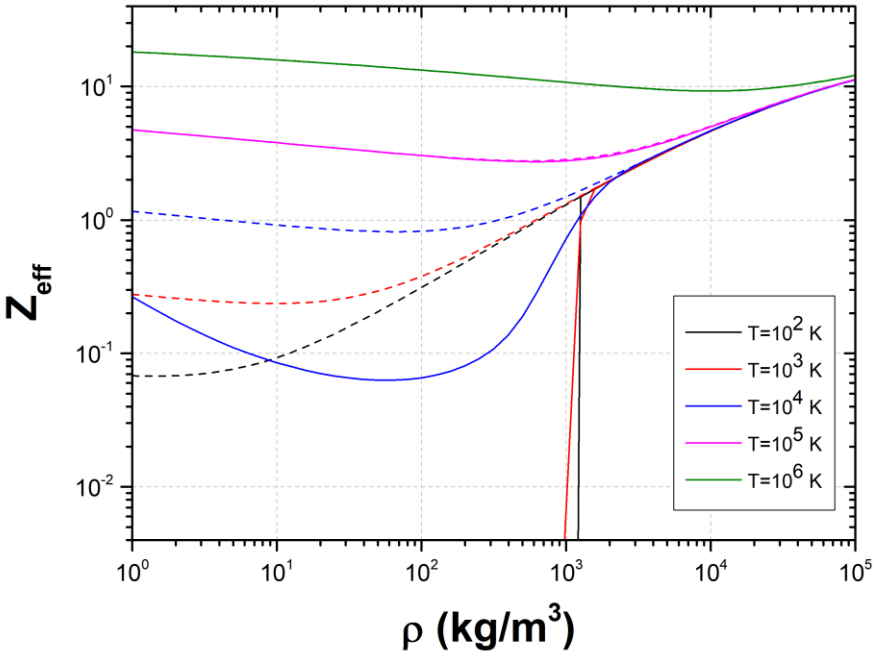

Figure 3.3. Effective ionization level of copper as a function of temperature and density. The dotted line represents the ionization levels obtained before applying the Desjarlais correction model, while the solid line represents the ionization levels after applying the model. The graph demonstrates that the corrected model accurately captures the insulator-like plasma state in the low-temperature, low-density condition.

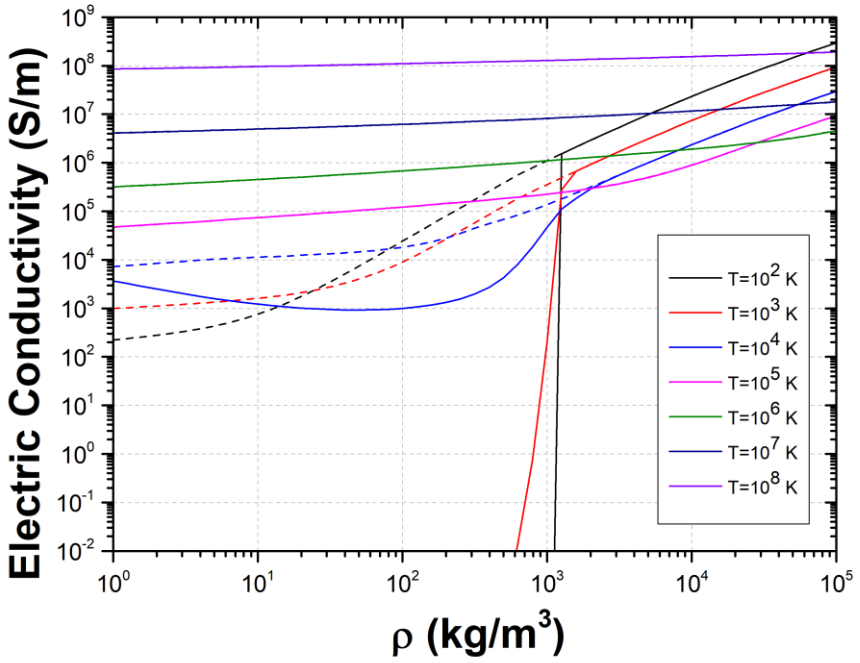

Figure 3.4. Electric conductivity of copper as a function of temperature and density. The dotted line represents the electric conductivity obtained before applying the Desjarlais correction model, while the solid line represents the electric conductivity after applying the model.

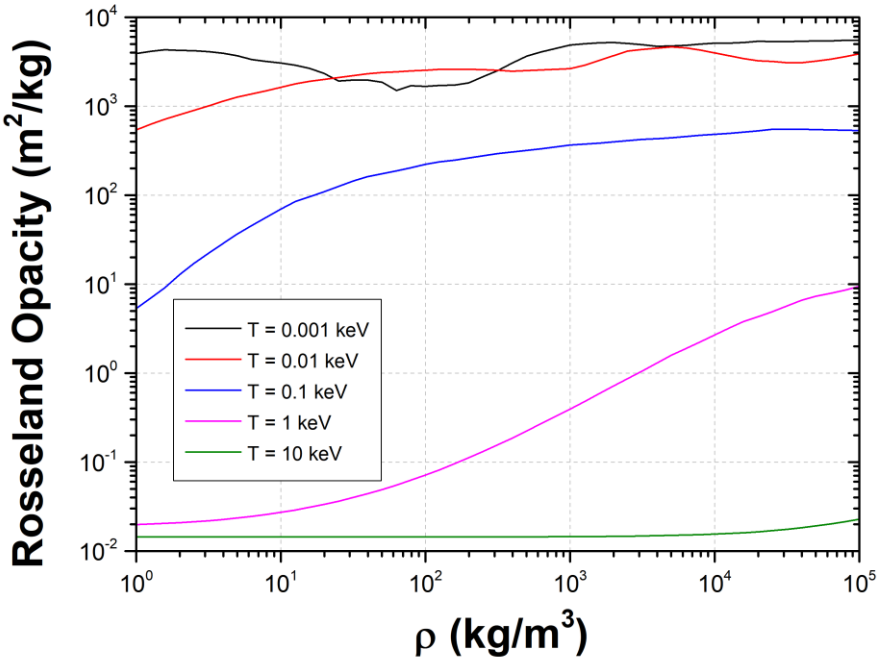

Figure 3.5. Rosseland mean opacity of copper calculated in ATOMIC, with a densites ranging from 1 to 10^5 $(\mathrm{kg/m^3})$ and a temperature ranging from 5×10^{-4} to 10 keV. The obtained opacity data is utilized for the radiation transport calculation in the X-pinch simulation.

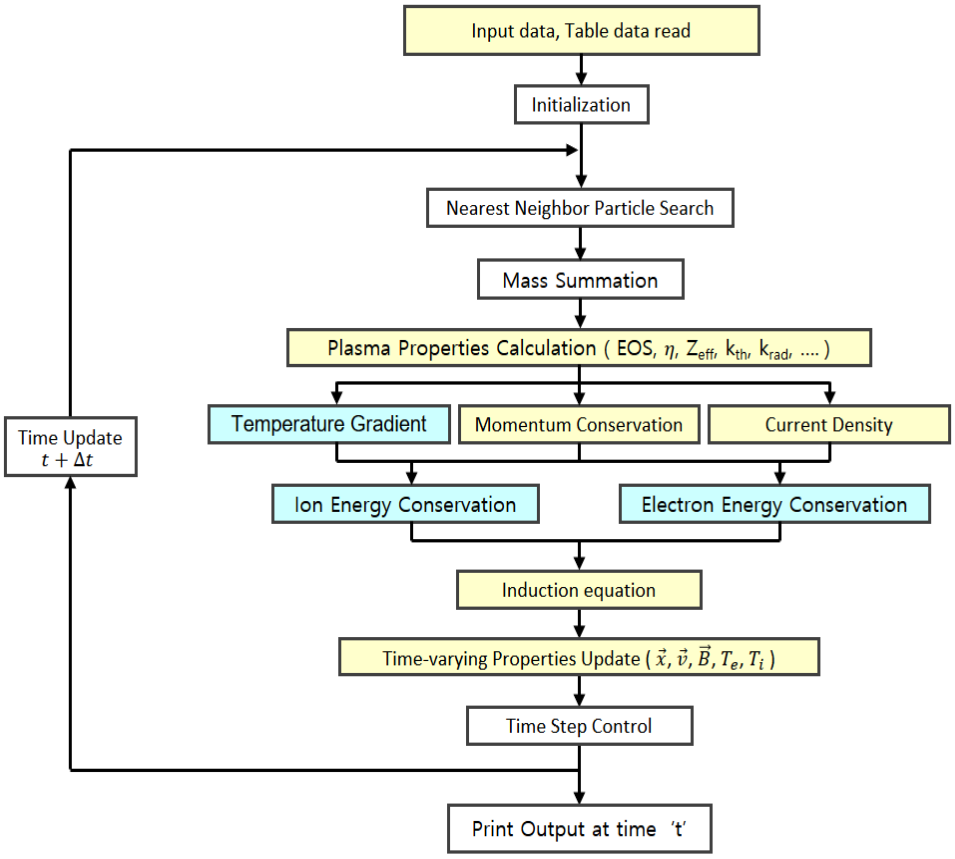

Figure 3.6. Simplified algorithm of SOPHIA-X code

Chapter 4

X-pinch Simulation

In this chapter, various numerical results obtained from the developed SPH-MHD code are examined. X-pinch simulations are conducted in full 3D dimensions, and the obtained results are compared with various previous findings, including experimental data from the X-pinch device at Seoul National University (SNU) (Ryu et al., 2021). The primary focus of this chapter is to compare the radiation loss power with the measured X-ray data. To achieve this, appropriate initial conditions for the simulations were designed to replicate the experimental setup. Subsequently, several key parameters of the X-pinch plasma obtained in the simulations are compared with the experimental results. The developed code demonstrates its capability to accurately handle the numerical demands of the X-pinch plasma evolution and provides precise insights into the mechanisms of plasma expansion, jet formation, and pinch generation. Additionally, it showcases the influence of radiation transport on the dynamic behavior of the simulated X-pinch plasma. The following sections present detailed simulation results and discussions related to these findings.

4.1 Experimental setup

In this section, experiments conducted to validate the developed SPH-MHD code for X-pinch analysis are described. Several experiments were designed and carried out at Seoul National University to investigate the radiation generation process in X-pinch (Ryu et al., 2021). The experiments were performed using an elaborately designed pulse generator capable of producing a peak current of approximately 100 kA, with a rise time of 523 ns. The generator was loaded with two thin copper wires, each having an initial diameter of 15~30 μm, which formed an X-pinch load. The distance between the anode and cathode was 10 mm, and the X-pinch wires were set at an angle of 90 degrees.

As illustrated in Figure 4.1, X-ray emissions were measured using a filtered absolute extreme ultraviolet (AXUV) diode array, which is capable of detecting soft X-ray spectra within the energy range of 1 to 10 keV. Previous studies utilizing this device have employed a comparison between experimentally measured X-rays and synthetic data to estimate the parameters of a copper plasma generated by an X-pinch (Ham et al., 2022). The experimental data obtained in this way are used as comparative data to evaluate the simulation results.

4.2 X-pinch simulation setup

4.2.1 Initial conditions for X-pinch simulation

The SPH particles are arranged with spacings of 30 μm in a 3D volume in the range of -2 mm < x < 2 mm, -2 mm < y < 2 mm, and -2 mm < z < 2 mm for X-pinch simulation. In this simulation, two copper wires are precisely positioned along the y and z axes. During the initialization of the simulation, the initial condition of the copper wire is represented as a cylindrical plasma with a higher temperature and lower density compared to the solid state. In this case, the copper wire with a diameter of 15 - 30 μm is replaced by a plasma with a diameter of 400 μm and a density ranging from 12.5 to 50.0 kg/m^3, while maintaining the line density. For all computational domains, the temperature of ions and electrons is initially set to 1000 K. However, the temperature inside the plasma rises rapidly due to the compression of the plasma that occurs in the initial stage of the simulation. Additionally, an initial low-density background of 0.1 kg/m^3 is set to model the vacuum. The distribution of the magnetic field is calculated using the provided experimental sinusoidal current through the approach described in the next section. The distribution of the magnetic field is calculated by utilizing the experimental sinusoidal current provided, employing the approach described in the subsequent section. To visually illustrate these initial conditions, Figure 4.2 presents the density and magnetic field distribution of the YZ plane, as well as the waveform of the current utilized in both the experiment and simulation.

4.2.2 Numerical modelling for X-pinch simulation

In various studies that have conducted pinch simulations, time-dependent magnetic field boundary conditions are often employed to solve this type of magnetic field-driven problem (Koundourakis et al., 2020; Byun et al., 2022;).

These conditions help impose the correct current density and energy flow within the system. In this approach, a transient time duration is required for the steady state to be reached after the propagation of a numerical wave back and forth (Fuyuan, 2018), several times, through the vacuum region where the induction equation relaxes to the Laplace equation. This characteristic transient time is inversely proportional to the resistivity and results in a significantly increasing time step for explicit codes. Moreover, applying time-dependent magnetic field boundary conditions can be challenging in complex geometries such as X-pinch. To overcome these limitations, a new procedure is proposed. The initial current density value of the simulation is determined using the current value at a specific experimental time moment. This current I_0 is uniformly distributed in the initial cylindrical plasma with radius R, so the azimuthal magnetic field $B(r)$ due to each wire is given by Eq. (4.1).

$$B(r) = I_0 \times \begin{cases} \dfrac{\mu_0 r}{2\pi R^2}, 0 \leq r \leq R \\ \dfrac{\mu_0}{2\pi r} \quad , R < r \end{cases} \tag{3.26}$$

Here, r is the distance from the center of the wire. At this time, the magnetic field distribution is derived over the global computational domain by linearly superposing the calculated values of each wire. In this study, instead of using a time-dependent magnetic field at the boundary planes, a different approach is employed to account for the imposed energy flow due to external current. In this approach, the magnitude of the magnetic field is updated proportionally across the entire computational domain based on the experimentally measured current. By solving the induction equation described in Eq.(3.19) using the updated

magnetic field, it is possible to determine the magnetic field distribution for the entire domain, taking into account the energy increase caused by the external current.

For a more stable and practical SPH simulation, this study incorporates certain constraints. Firstly, an upper limit on resistivity is imposed. According to the CFL condition that determines the time step, the time scale of the resistive MHD simulation is proportional to the material conductivity. This implies that a very small time step is required due to the high resistivity of the vacuum. To address this issue, a resistivity limiter is employed, set at a value of 10^{-5} Ωm. This allows for a reasonable time-step value, in a similar way to the approach used in previous studies (Skoulakis, 2022). Next, an additional constraint was implemented to ensure accurate radiation diffusion calculations in the low-temperature region. As described in Section 3.3.3, obtaining an accurate Rosseland mean opacity value of the plasma is crucial for radiation calculations, which is obtained using the ATOMIC code. However, the opacity data provided by the ATOMIC code is limited to temperatures above approximately 5×10^{-4} (K), resulting in potential inaccuracies in radiation calculations for the low-temperature region. To overcome this limitation, the approach employed in the ALEGRA code was adopted. In the ALEGRA code, the diffusion coefficient $D = c\lambda/\kappa_R\rho$ is replaced by the free streaming $D_{FS} = E_R/|E_R|$ when the flux limiter value is low (T. A. Brunner, & T. A. Mehlhorn, 2009). In a similar way, this study avoids the use of the Rosseland mean opacity by utilizing the free-streaming coefficient D_{FS} in the region $R > 100$.

4.3 X-pinch simulation results and discussions

4.3.1 Evolution of an X-pinch

X-pinches undergo several stages that are generally common to all X-pinch configurations: ablation, formation of micro-Z-pinches, hot spot formation, intense X-ray emission, Z-pinch collapse, and electron-beam emission. This process was also confirmed through an X-pinch simulation conducted on a 30μm-thick copper wire, as depicted in **Figure 4.3**, illustrating the implosion behavior of the X-pinch plasma in the crossed wire plane. In this section, each step of the X-pinch's time evolution is described in detail, based on the various investigated plasma parameters.

4.3.2 Evolution of an X-pinch: Micro-Z pinch formation

In the initial stages of the simulation (0–50 ns), the JxB force acts toward the center of the wire due to the current flowing in the plasma, resulting in compression of the plasma. This rapid compression leads to a significant increase in the plasma density at the cross point. This process is corroborated by **Figure 4.4**, which illustrates the temporal evolution of the maximum plasma density. Initially distributed at a density of 50 kg/m^3, the plasma undergoes compression, reaching a density of 100 kg/m^3 within a brief duration of 50 nsec. This compression subsequently leads to the formation of a high-pressure region, generating an expansive force. As a result of strong compression, a neck, similar in shape to that of a classical Z-pinch, forms at the crossing point of the X-pinch. This neck persists in a long-term quasi-equilibrium state, maintaining a nearly

constant density until the expansive force surpasses the compressive force (50–300 ns).

4.3.3 Evolution of an X-pinch: Jet formation

The overall shape of the X-pinch neck leads to an increase in the azimuthal magnetic field B_ϕ, accelerating the implosion of the plasma towards the axis. In **Figure 4.5**, it can be observed that the azimuthal magnetic field rapidly increases starting at 100 nsec, which aligns with the formation of the neck, in comparison to the externally applied current waveform. The rapid increase in the azimuthal magnetic field results in plasma transport in the vertical direction, known as a jet. Simultaneously, a new azimuthal global magnetic field is generated along the jet, as depicted in **Figure 4.6**. This global magnetic field continuously accelerates the jet. The evolution of the jet is analyzed and presented in **Figure 4.7**, where the instantaneous axial velocity of the plasma fluid is calculated along the vertical axis at specific time intervals. The accelerated jet reaches a convergence value after 150 ns, and the actual formation of the jet is observed at 250 ns in **Figure 4.3**. The maximum velocity remains constant between 15 km/s and 22 km/s until 350 ns, as indicated by the purple and navy curves. The axial jet velocity observed in the simulation corresponds to a physically reasonable value when compared to previous experimental and simulation studies. In particular, the convergence trend for the jet velocity observed in this study closely matches the simulation results conducted by Koundourakis (2020), confirming that the developed code accurately captures the dynamics of the X-pinch jet.

4.3.4 Evolution of an X-pinch: Hot spot formation

When the neck formed in the previous process continues to undergo compression and reaches a critical point, a hot spot is formed. This hot spot represents the region where the highest plasma parameters are achieved and serve as a source of X-ray emission with extreme characteristic. Accurately interpreting the hot spot in X-pinch plasma simulations is crucial due to its significant impact on the properties of the generated plasma. The radiation emitted by the hot spot serves as a valuable diagnostic tool, enabling researchers to gain insights into the characteristics of X-pinch plasma. Furthermore, precise interpretation of hot spots aids in optimizing the experimental designs of X-pinches, enhancing their overall performance and effectiveness.

As mentioned in previous studies, it is natural to expect that the maximum plasma parameters will be reached at the moment of maximum plasma compression, specifically in the neck when it reaches its minimal size. Although this statement may seem obvious, it is crucial to verify its validity. The developed SPH-MHD code is suitable for confirming this validity because it provides comprehensive information on the spatiotemporal evolution of various X-pinch parameters. I tracked the hot spot by analyzing the time-varying changes in the maximum electron temperature measured during the simulation. According to the simulation results, a hot spot characterized by the highest electron temperature occurs at 313 nsec when the neck is compressed to its maximum extent, as depicted in **Figure 4.3** and **4.8**. The electron temperature at this time is approximately 6.34×10^{6} K, and the electron density is measured to be around 2.54×10^{22} cm^{-3}. These plasma parameters obtained through analysis are then compared with the results estimated in the experiment. In the experiment (Ham

et al., 2023), the diagnostic system measured spatially integrated X-ray data, allowing for the estimation of various plasma parameters within the X-pinch. The plasma parameter near the hot spot, estimated using this method, is illustrated in Figure 4.8. In the experiment conducted under the same conditions as the simulation, the electron temperature and electron density at the hot spot were estimated as 1.36×10^{7} K and 9.54×10^{22} cm^{-3}, respectively. These results are summarized in **Figure 4.9**. The disparity between the measured plasma parameters in the experiment and the lower values observed in the X-pinch simulation can be attributed to several factors. Firstly, the diagnostic system employed in the experiment captures spatially integrated X-ray data, which means it collects information from various plasma regions within the X-pinch. This amalgamation of different plasmas, including high-energy electron components, can result in an upward estimation of parameters such as electron temperature and density. Secondly, the method of analyzing a wide range of spectra in the experiment introduces uncertainties due to the significant influence of continuum and K-shell radiation. Consequently, these factors collectively contribute to the possibility of overestimating the plasma parameters in the experiment. Taking these factors into consideration, it is assessed that the simulation reasonably reproduces the plasma parameters.

Another important aspect of X-pinch hot spot dynamics pertains to the emission of high-energy radiation from the hot spot. A more comprehensive analysis regarding the radiation characteristics of the hot spot has been conducted and will be presented in the following section.

4.3.5 Evolution of an X-pinch: Neck breaking

The final phase of X-pinch dynamics begins after the occurrence of the X-ray burst. During this stage, the thin neck that formed at one or two locations starts to dissipate, leading to the gradual dissipation of the X-pinch over time. As shown in the radiograph of **Figure 4.10**, the gap created by this process exhibits a significantly lower plasma density compared to that found in the neck. This gap is accurately reproduced in the simulation. As evident from the density distribution at 350 nsec shown in **Figure 4.3**, the formation of a hot spot and rapid mass loss immediately follow the occurrence of the X-ray burst. In the X-pinch simulations conducted under various conditions, I confirmed that the mass in the region measuring 0.2 mm x 0.2 mm x 0.2 mm near the cross point was reduced by over 70% within the time of hot spot formation +10 nsec. The exact reasons for the disassembly of the X-pinch are still uncertain, and despite the existence of various theories, no consensus has been reached among them. In this process, estimating plasma parameters is challenging due to the lack of sufficient radiation signals, leaving us with only limited inferences based on radiographs. However, the simulation conducted in this study directly confirms the velocity field, which is challenging to measure in experiments, providing a means to verify the disassembly process directly.

Figure 4.11 presents the velocity fields at 300 nsec and 350 nsec before and after the emission of radiation. Additionally, **Figure 4.12** specifically illustrates the velocity field in the direction perpendicular to the axis of the plasma jet. As observed in the velocity field, the plasma, initially compressed along the axial direction prior to radiation emission, exhibits movement away from the axis after the emission. This transport of plasma originates within the wire plasma and

gradually extends outward, with the plasma spreading at a velocity of approximately 3 m/sec at 350 nsec. Subsequently, this tendency of the velocity field remains consistent until the complete dissipation of the pinch.

4.3.6 Radiation emission from the X-pinch hot spot

Radiation power was measured to verify the emission characteristics of X-pinch radiation. The radiation power was calculated by integrating the power density values obtained at each time step within a 1 mm × 1 mm × 1 mm region near the cross point. The calculated radiation power, along with the temporal evolution of X-pinch density, is presented in Figure 4.13. Examining these results along with the electron temperature change depicted in Figure 4.8, the simulated X-pinch process follows this sequence: (1) Hot spot formation (313 nsec), (2) Radiation emission (327 nsec), and (3) Neck breaking (334 nsec).

Figures 4.14 to **4.18** present the measurements of X-ray emissions under various conditions, comparing them with experimental data. The simulation results demonstrate that the radiation power derived from the simulations accurately captures the experimentally measured X-ray profile in quantitative terms. However, there are some discernible discrepancies between these two datasets. Firstly, the simulation exhibits a lower radiation yield compared to the experimental measurement and fails to capture the sharp and sudden X-ray characteristics. I tentatively speculate this difference to the insufficient resolution employed in the simulation. A low resolution does not accurately capture a hot spot formed in a very narrow area and may underestimate the electron temperature. Moreover, energy transport, which is crucial for radiation emission,

may disperse extensively in the surrounding space, leading to a delay in X-ray generation. As another distinguishing feature, the simulation can not measure power peaks above 7.0 keV. This difference seems natural because this hard X-ray (HRX) emission is experimentally associated with the electron beam of the neck break structure and the single fluid model used in this simulation is not capable of producing the electron beam effect. However, despite these disparities, notable advancements have been observed when comparing them to previously proposed simulation models. **Figure 4.19** displays the outcomes of measuring the radiation power of the copper X-pinch using the STHENO code under conditions akin to those employed in this study (Byun, 2021). Although this reference code comprehensively elucidated the radiation characteristics of pinch plasma under diverse conditions, there exists a significant disparity in the radiation power values when compared to the experiment conducted in this study, differing by several orders of magnitude. On the other hand, the simulation conducted in this study accurately predicts the magnitude of the radiant force, which is comparable to the experimental measurements. This comparison indicates the effectiveness of the radiation model employed in this study under specific pinch conditions.

Finally, the variation in radiation emission time was verified and compared with experimental data under different conditions. Comparing the total radiation power with the experiment is challenging, and due to the difficulty in precisely capturing the maximum peak, the radiation emission time was determined based on the first peak observed in the radiation power above 1.6 keV. These comparison results are summarized in **Table 4.1**. As mentioned earlier, the simulation exhibits a delay in radiation emission compared to the experiment, but it demonstrates a similar trend. Specifically, it was observed that in both cases, an

increase in wire diameter led to a decrease in the rate of radiation emission, while an increase in voltage resulted in a faster rate of radiation emission.

Table 4.1 Comparison of X-ray emission time between experiment and simulation

Voltage	***Experiment***		***Simulation***	
	Wire Diameter	*X-ray emission*	*Wire Diameter*	*X-ray emission*
55kV	20 *μm*	248 *nsec*	20 *μm*	*276 nsec*
	25 *μm*	271 *nsec*	25 *μm*	291 *nsec*
	30 *μm*	308 *nsec*	30 *μm*	327 *nsec*
50kV	15 *μm*	205 *nsec*	15 *μm*	219 *nsec*
	25 *μm*	324 *nsec*	25 *μm*	340 *nsec*

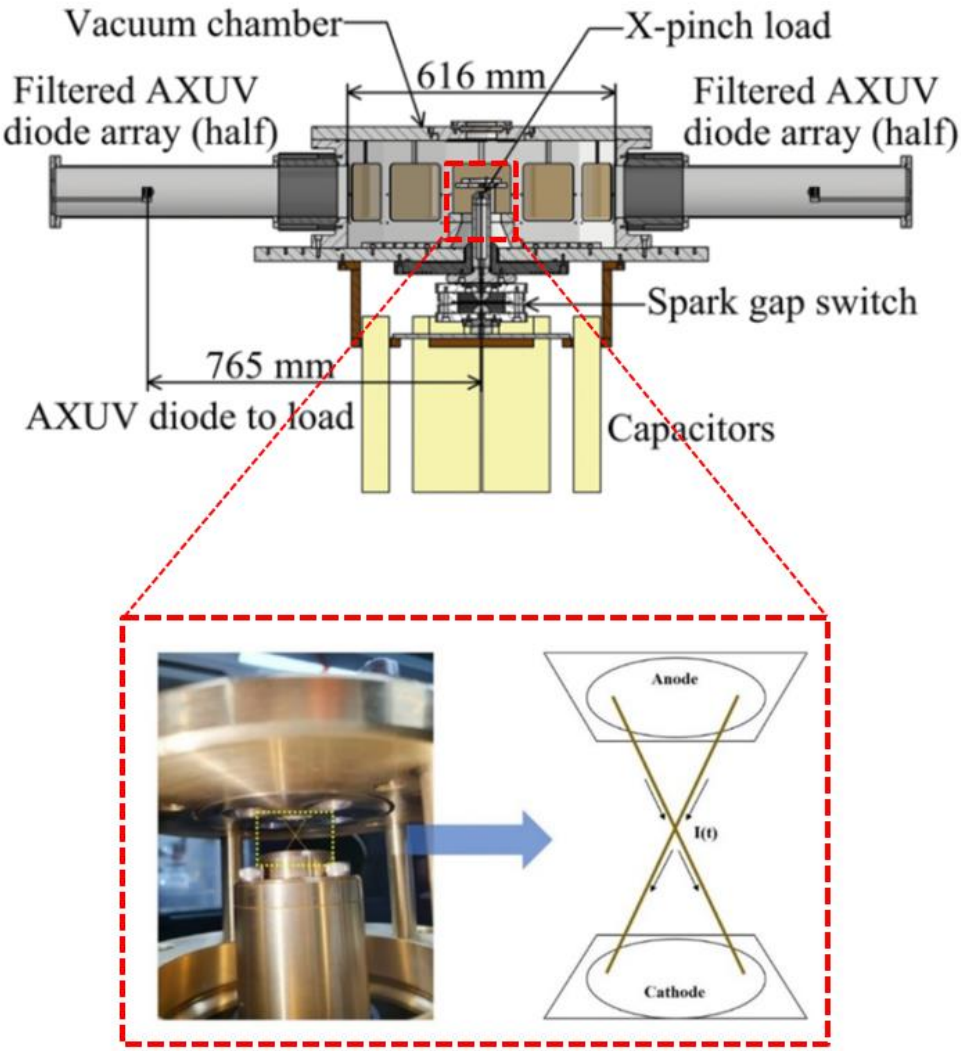

Figure 4.1. Schematic view of SNU X-pinch device with the filtered AXUV diode array. [Ham et al., 2022]

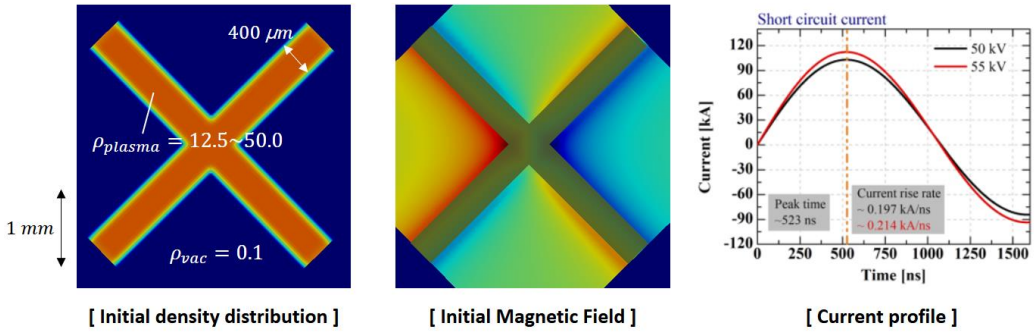

Figure 4.2. Initial condition of the X-pinch simulation

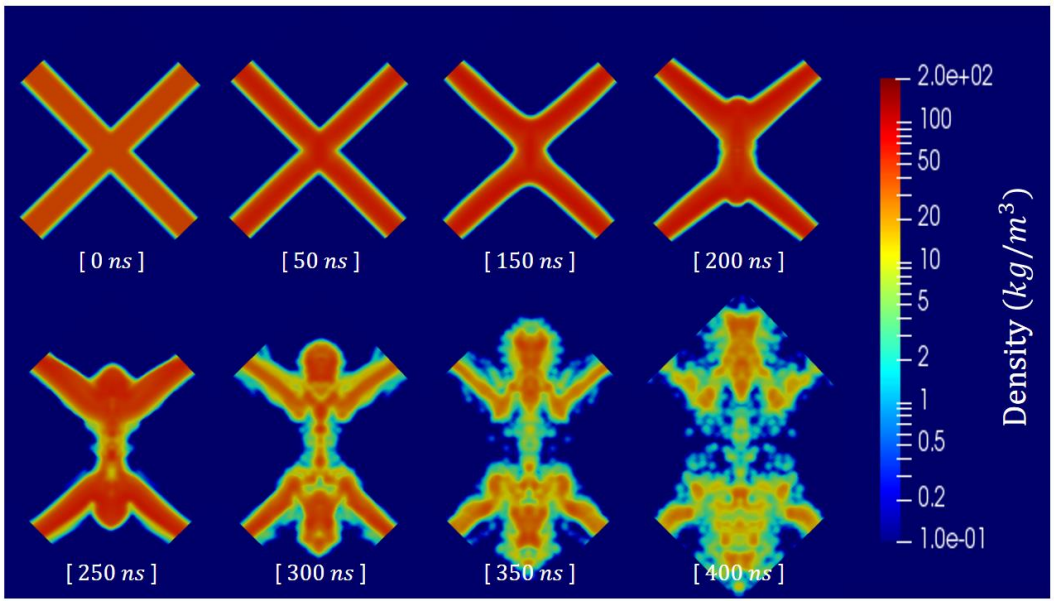

Figure 4.3. Time evolution of density distribution in X-pinch simulations

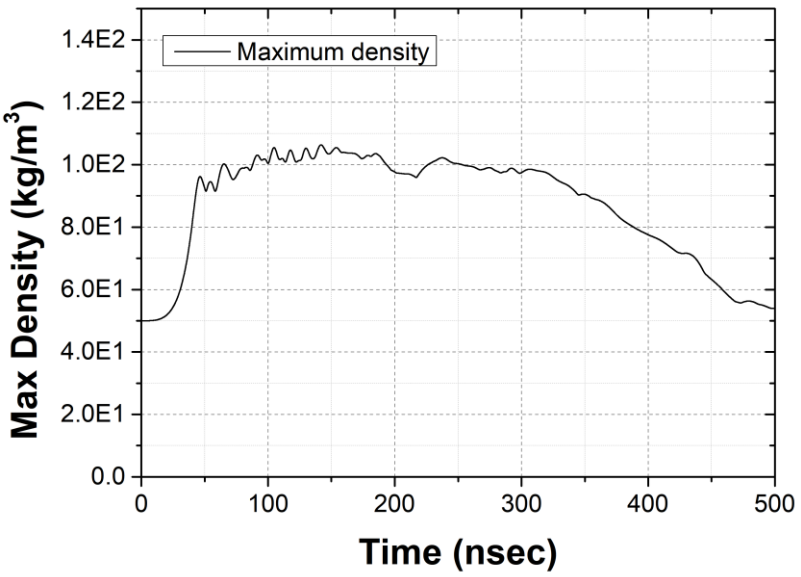

Figure 4.4. The time evolution of the maximum plasma density

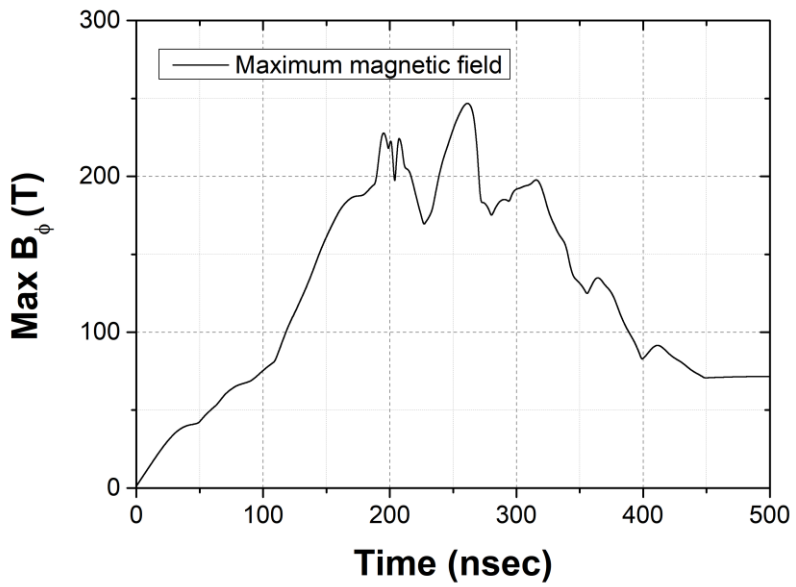

Figure 4.5. The time evolution of the maximum azimuthal magnetic field

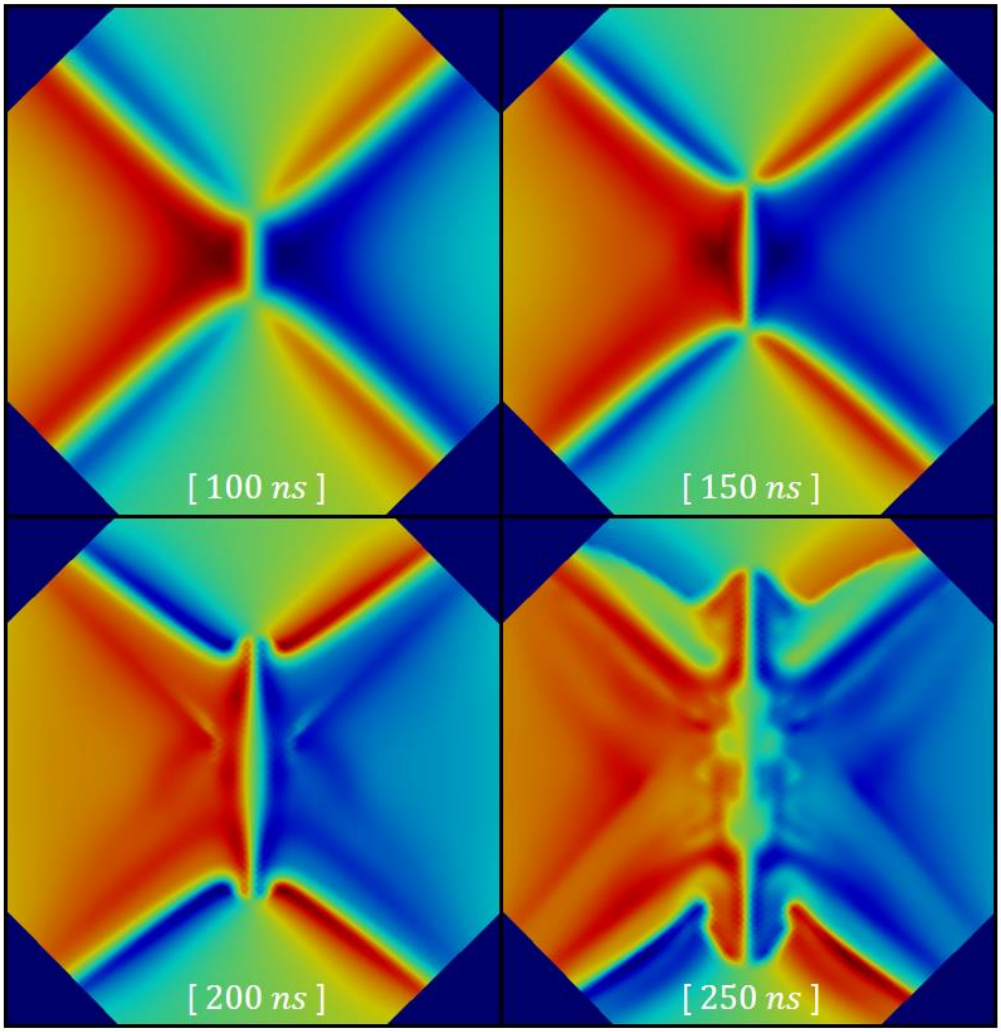

Figure 4.6. The time evolution of the azimuthal magnetic field distribution

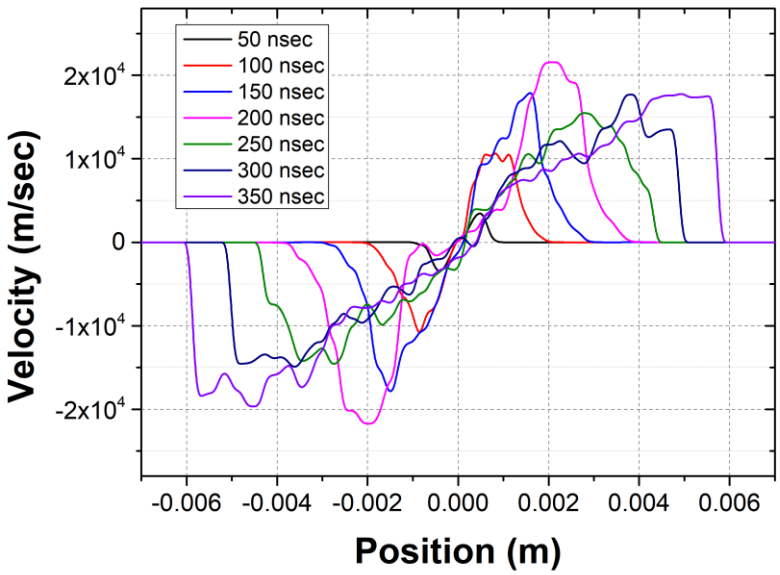

Figure 4.7. Time evolution of the axial fluid jet velocity, along the vertical axis at 50 - 350 ns

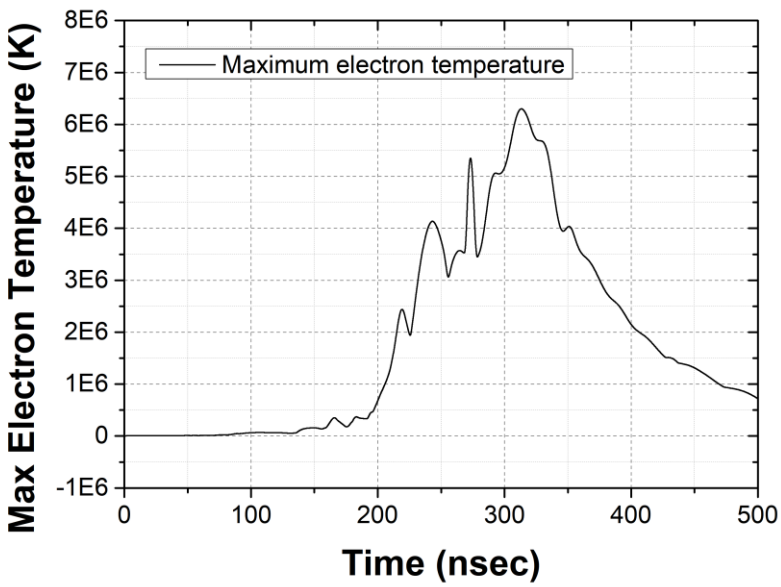

Figure 4.8. Time evolution of the maximum electron temperature

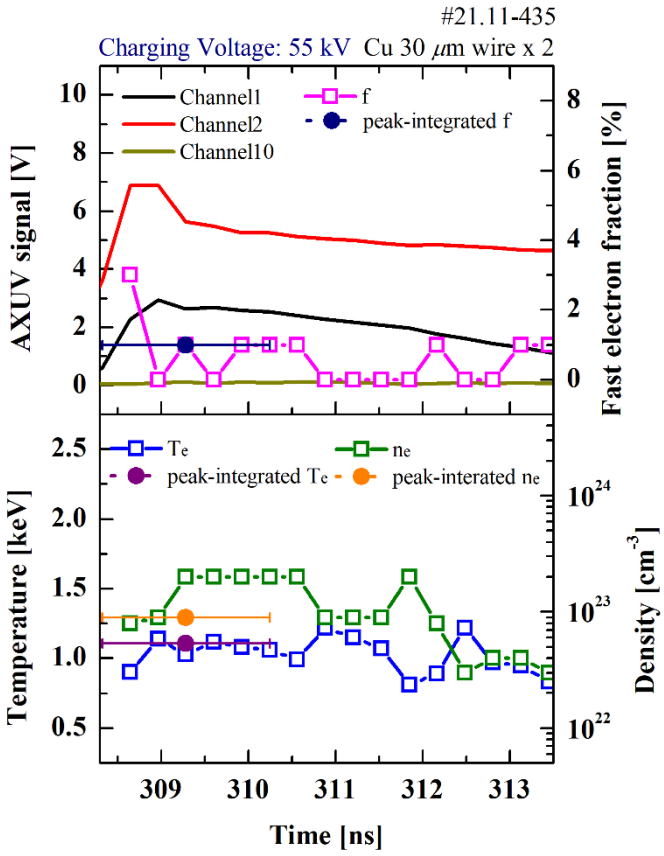

Figure 4.9. Temporal evolution of estimated electron densities, electron temperatures, and fast electron fractions around the X-pinch hot spot

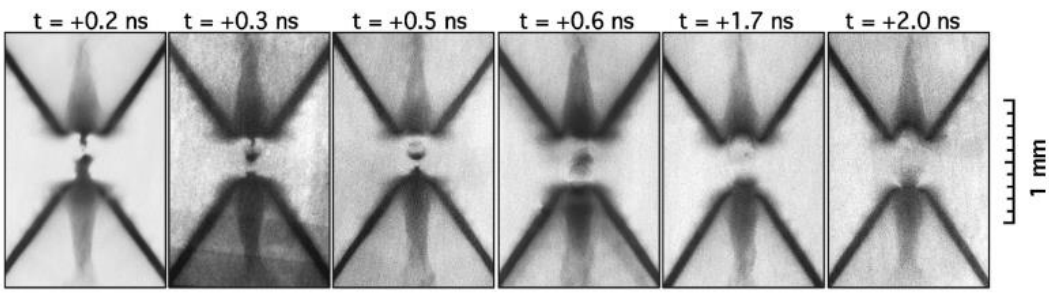

Figure 4.10. A series of radiographs of wire X-pinch just after the emission of its X-ray burst (T. A. Shelkovenko et al., 2001)

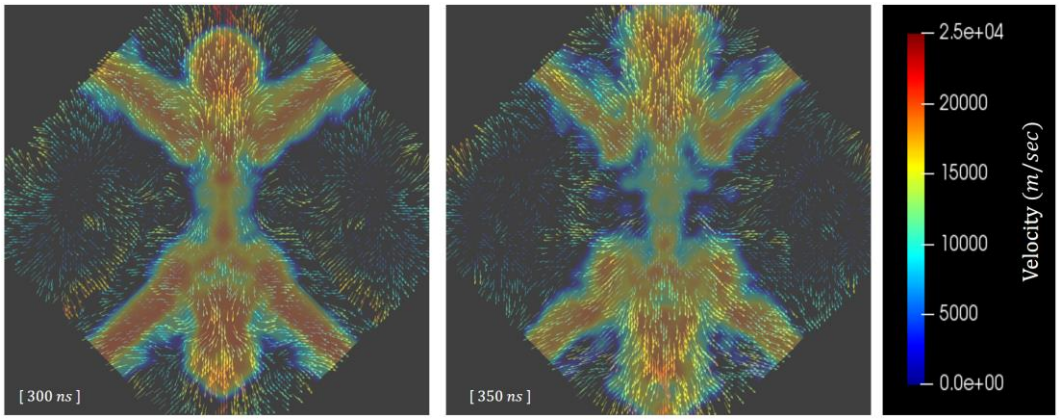

Figure 4.11. Velocity profile of X-pinch simulations at 300 and 350 nsec

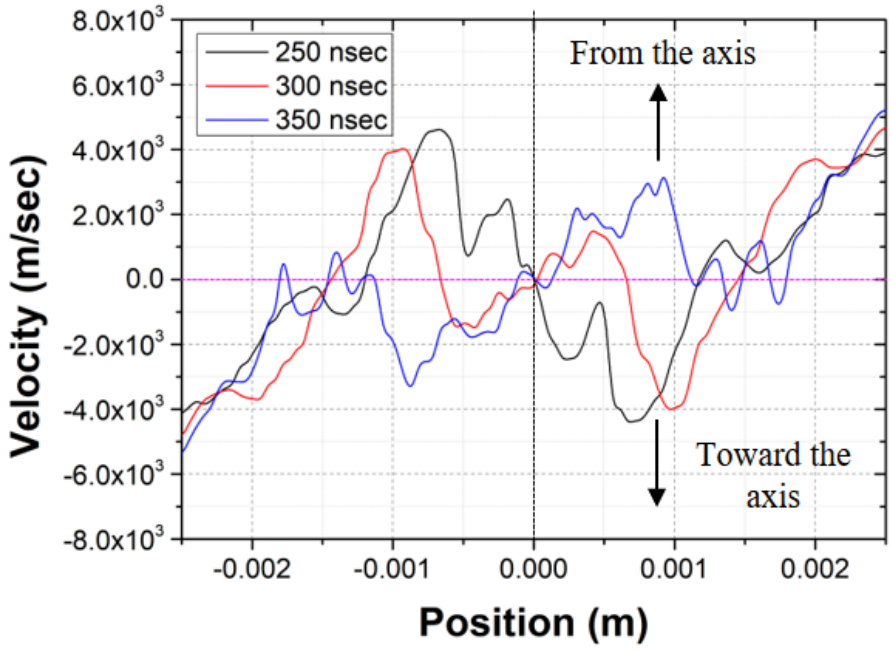

Figure 4.12. Time evolution of the radial jet velocity

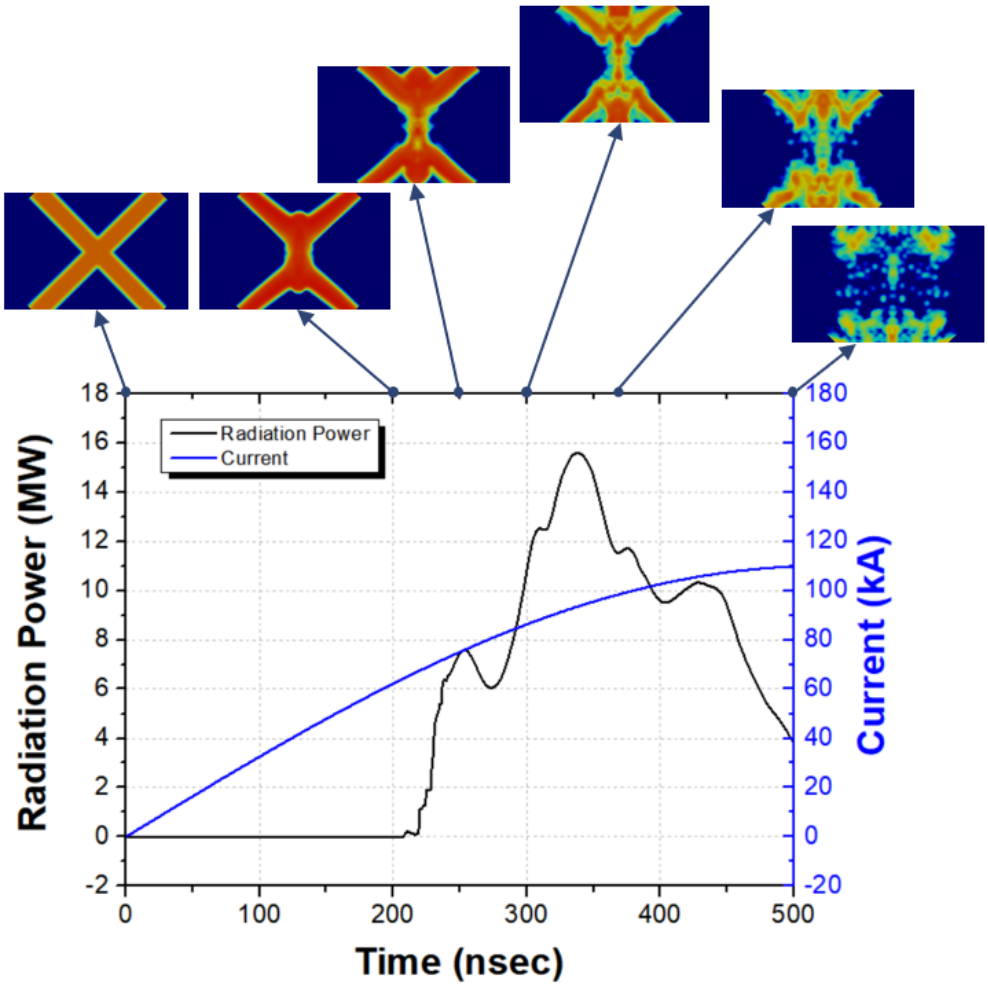

Figure 4.13. Time evolution of the radiation power

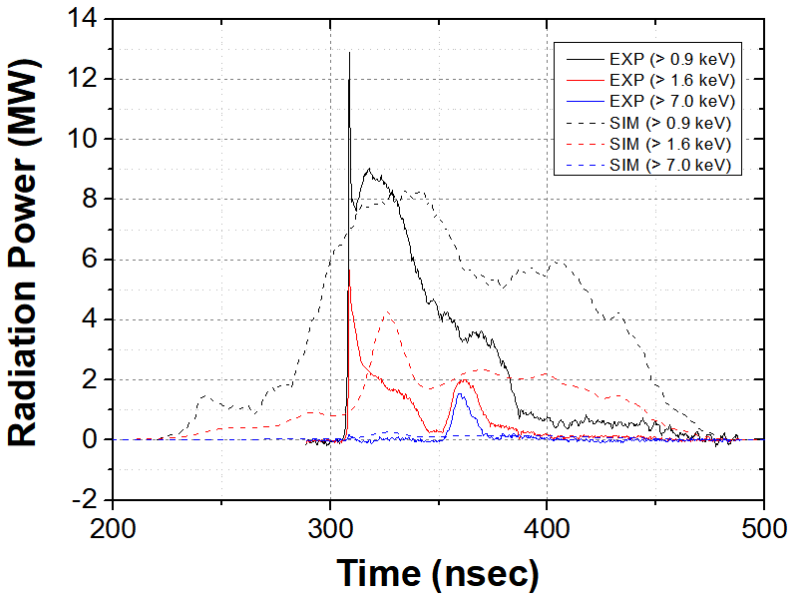

Figure 4.14. Comparison between the simulated radiation power (dashed line) and the measured X-ray power (line). Experiments and simulations were conducted by applying a voltage of 55 kV to copper wires (ϕ30μm)

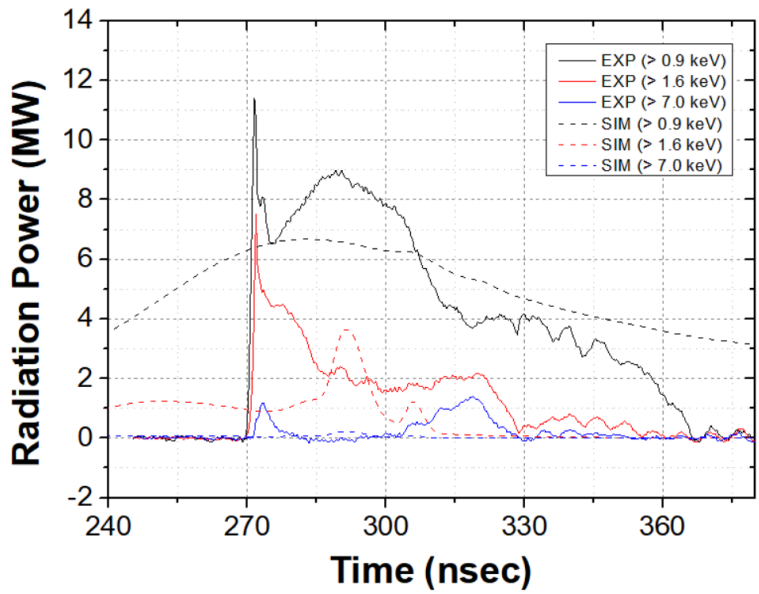

Figure 4.15. Comparison between the simulated radiation power (dashed line) and the measured X-ray power (line). (55 kV, ϕ25μm)

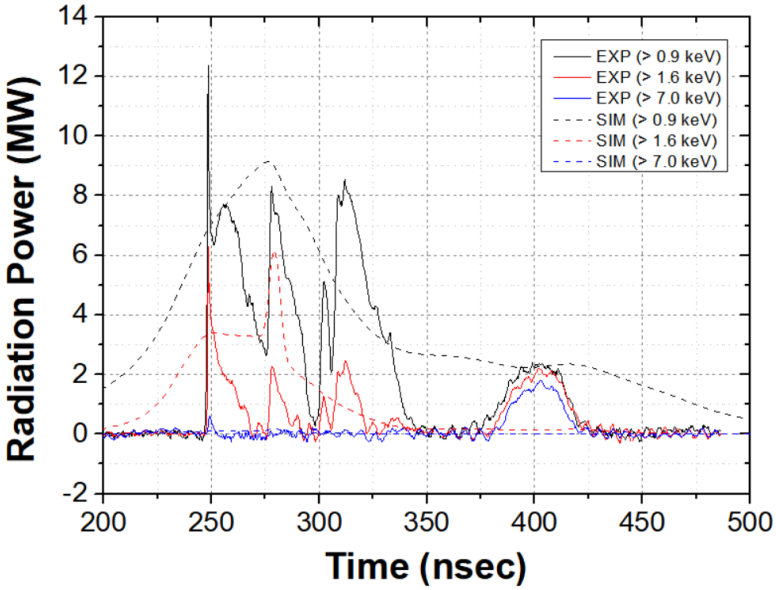

Figure 4.16. Comparison between the simulated radiation power (dashed line) and the measured X-ray power (line). (55 kV, ϕ20μm)

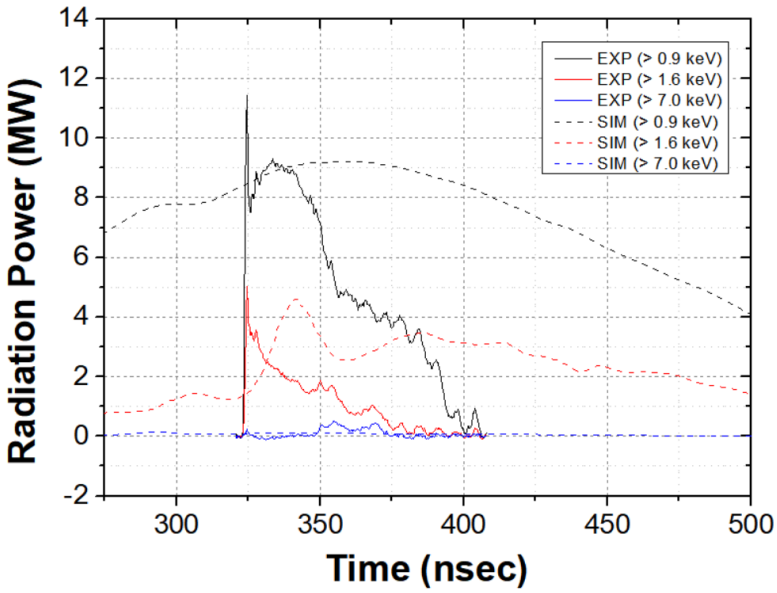

Figure 4.17. Comparison between the simulated radiation power (dashed line) and the measured X-ray power (line). (50 kV, ϕ25μm)

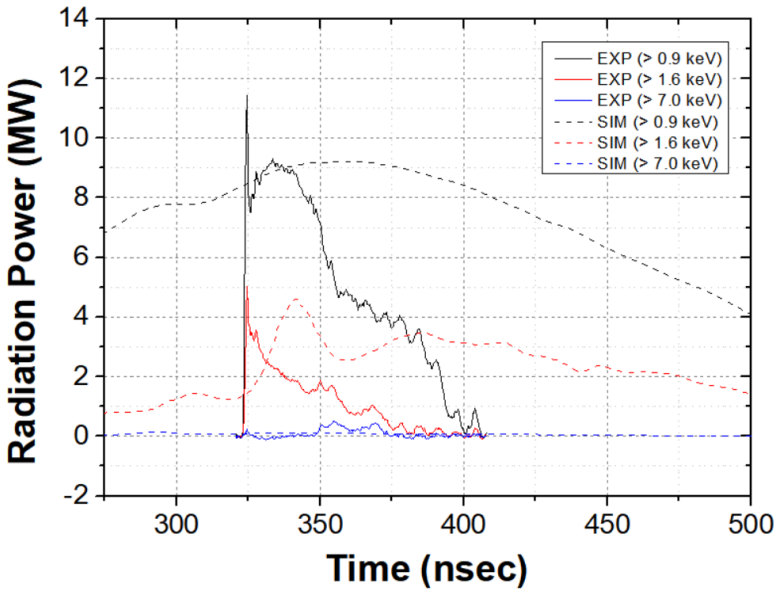

Figure 4.18. Comparison between the simulated radiation power (dashed line) and the measured X-ray power (line). (50 kV, ϕ15μm)

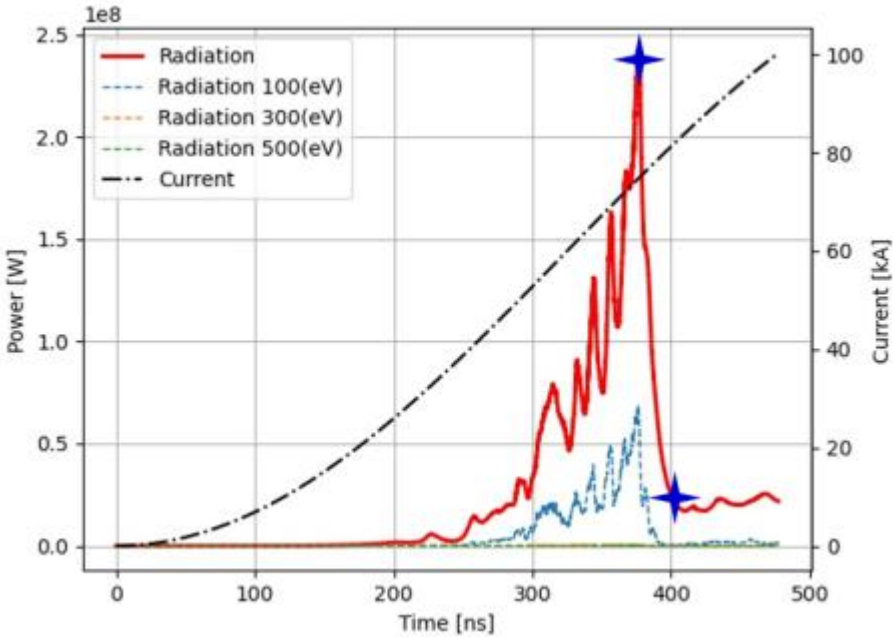

Figure 4.19. Radiation loss power of the copper X-pinch (ϕ30μm) (Byun, 2021)

Chapter 5

Conclusion and Recommendation

5.1 Conclusions

In this study, the SPH-MHD code was developed to simulate the complex X-pinch plasma evolution under extreme conditions. This study is the first implementation of an X-pinch simulation using the SPH methodology, and it can be used as a valuable tool for generating data that is challenging to confirm through experiments or aiding in experimental design. Throughout the study, the achievements, results, and findings are as follows.

(1) Development of SPH-MHD model

A Lagrangian resistive MHD model was developed using the smoothed particle hydrodynamics method. The model has incorporated several advanced numerical treatments, such as a correction term to satisfy the $\nabla \cdot B$ constraint and some artificial dissipation terms to govern the shock wave. Notably, the introduction and implementation of a novel SPH discretization for non-ideal MHD terms enable the model to effectively capture the non-ideal effects of plasma that were unaccounted for in the existing SPH-MHD model. Furthermore, verification with extensive benchmark problems confirms the model's reliability, as the simulation

results exhibited excellent qualitative and quantitative agreement with reference data.

(2) Integration of physics models for X-pinch simulation

Detailed physics models were integrated into the code for the realistic X-pinch simulation. In this study, the SPH-MHD code was expanded to incorporate a two-temperature equation, which allows for the separation of electron and ion energies. Given that the numerical time step size is significantly smaller than the electron-ion collision time scale, a two-temperature description adequately represents the plasma under high-energy-density (HED) conditions. The code utilizes the equation of state (EOS) based on the Thomas-Fermi theory to accurately capture the characteristics of the HED plasma in the X-pinch scenario. Specifically, it addresses the overestimation of ionization in the low-density regions by adopting the Desjarlais correction model as the plasma ionization balance model. Moreover, a radiation model based on the flux-limited diffusion approximation was integrated into the code to account for energy loss through X-ray emission across a broad energy range.

(3) Simulation of the X-pinch plasma evolution

Using the developed code, X-pinch simulations were conducted in full 3D dimensions, and the obtained results were compared with experimental data from the X-pinch device at Seoul National University under the same conditions. The simulations successfully reproduced the four-step X-pinch evolution process (1. Neck formation, 2. Jet formation, 3. Hot spot formation, 4. Neck breaking) commonly observed in various X-pinch configurations. Additionally, the

simulations provided comprehensive spatiotemporal information on a wide range of plasma parameters, including density, temperature, velocity field, and radiated power. Notably, the electron temperature and density at the hot spot were well reproduced at a reasonable level when compared with the experimental values, demonstrating the accuracy and reliability of the developed simulation code. Moreover, the radiation data showed significantly higher accuracy compared to previous simulation results, further affirming the effectiveness of the proposed model. Finally, the simulations provided valuable information about various plasma parameters that are challenging to measure in experiments. Specifically, in this study, the formation and evolution of the jet were accurately captured through the velocity field near the X-pinch cross point. These results can be utilized as reference points for the design of experimental and diagnostic devices for X-pinch studies.

5.2 Recommendations

The result of this research suggests following further studies.

1. In this study, X-pinch plasma simulation and validation were conducted under limited conditions consistent with the experimental conditions. Further simulations are recommended to be performed to investigate the effect of various variables such as current magnitude, frequency, and wire material on X-pinch dynamics.
2. The discrepancy in radiation power estimation during X-pinch simulations is presumed to result from potential issues related to particle resolution.

Some studies suggest that a resolution of at least 10 μm is required to accurately follow hot spot formation in the X-pinch. To overcome computational resource limitations hindering higher-resolution research, the 3D X-pinch problem can be effectively addressed by remapping it into a 2D domain.

3. The developed code employs an EOS table derived from the Thomas-Fermi theory, offering the advantage of efficient and straightforward EOS calculations. However, this approach relies on an empirical formula, limiting its realism. The integration of more advanced theories, such as Density Functional Theory (DFT) and DFT-Molecular Dynamics (DFT-MD) based on first principles, is anticipated to enhance the accuracy of X-pinch
4. This study incorporates the flux-limited diffusion model as the radiation model, enabling more realistic X-pinch calculations compared to previous studies that relied on optically thin assumptions. However, the two-temperature equation employed in this study implies the assumption that the temperatures of electrons and radiation are equal, which may deviate from the actual scenario. To achieve greater physical accuracy, it is proper to employ the 3-temperature equation, which directly computes the radiation energy, in the calculations. For this, a set of equations to calculate the radiation energy (E_R) needs to be added, and a new material property table (κ_p) is required.
5. The model utilized in this study does not incorporate the ablation process, where a solid wire is transformed into plasma. Consequently, the simulation assumes the complete conversion of the metallic wire to plasma

in the initial condition. Considering the non-negligible power consumed in the ablation process, it is crucial to include a model for this phenomenon in future investigations.

References

A. Bonafede, K. Dolag, F. Stasyszyn, G. Murante, and S. Borgani, “A non-ideal magnetohydrodynamic GADGET: Simulating massive galaxy clusters”, Mon. Not. R. Astron. Soc. 418, 2234–2250 (2011)

A. Ciardi, “The evolution of magnetic tower jets in the laboratory“, Physics of Plasmas 14, 056501 (2007)

A. Kemp and J. Meyer-ter-Vehn, “An equation of state code for hot dense matter, based on the QEOS description”, Nucl. Instrum. Methods Phys. Res., Sect. A 415(3), 674–676 (1998)

A. L. Velikovich, J. L. Giuliani, S. T. Zalesak, J. W. Thornhill, and T. A. Gardiner, Exact self-similar solutions for the magnetized Noh Z pinch problem, Phys. Plasmas 19 012707 (2012)

A. Mignone, G. Bodo, S. Massaglia, T. Matsakos, O. Tesileanu, C. Zanni, A. Ferrari, PLUTO: A Numerical Code for Computational Astrophysics, The Astrophysical Journal Supplement Series, 1(170), 228–242 (2007)

A. Skoulakis et al.,,” High performance simulations of a single X-pinch, Plasma Physics and Controlled Fusion”, 64 (2) (2022)

Brio, M, C.C. Wu, “An Upwind Differencing Scheme for the Equations of Ideal Magnetohydrodynamics”, J. Comput. Phys. 75, 400-422 (1988)

D.-K. Kim and I. Kim, “Calculation of ionization balance and electrical

conductivity in nonideal aluminum plasma", Phys. Rev. E 68, 056410 (2003)

D. Haas, S. C. Bott, V. Vikhrev, Y. Eshaq, U. Ueda, T. Zhang, E. Baranova, S. I. Krasheninnikov and F. N. Beg, Dynamics of low-density coronal plasma in low current x-pinches, Plasma Phys. Control. Fusion 49 1151 (2007)

D. J. Price and J. J. Monaghan, "Smoothed Particle Magnetohydrodynamics—I. Algorithm and tests in one-dimension", Mon. Not. R. Astron. Soc. 348(1), 123–138 (2004)

D. J. Price, J. J. Monaghan, Smoothed Particle Magnetohydrodynamics–II. Variational principles and variable smoothing-length terms, Mon. Not. Roy. Astron. Soc., 348 (1), 139-152 (2004)

D. J. Price, Smoothed particle hydrodynamics and magnetohydrodynamics, J. Comput. Phys. 231 (3), 759-794 (2012)

D. S. Balsara, "Total variation diminishing scheme for adiabatic and isothermal magnetohydrodynamics", Astrophys. J., Suppl. Ser. 116(1), 133 (1998)

F. N. Beg, A. Ciardi, I. Ross, Y. Zhu, A. E. Dangor and K. Krushelnick, "Jet Formation and Current Transfer in X –Pinches", in IEEE Transactions on Plasma Science 34 (5), pp. 2325-2329 (2006)

Fuyuan Wu, Rafael Ramis, Zhenghong Li, "A conservative MHD scheme on unstructured Lagrangian grids for Z-pinch hydrodynamic simulations", Journal of Computational Physics 357, pp. 206-229 (2018)

G. Koundourakis, et al., "A numerical study on laboratory plasma dynamics

validated by low current x-pinch experiments”, Plasma Phys. Control. Fusion 62, 125012 (2020)

G. R. Liu, and M. B. Liu, "Smoothed particle hydrodynamics: a meshfree particle method", World scientific (2003)

G. W. Collins, D. Marsical, D. M. Haas, R. E. Madden, K. Gunasekara, J. Kim, M. L. Abarr, S. C. Bott, J. P. Chittenden and F. N. Beg, Effect of the global to local magnetic field ratio on the ablation modulations on X-pinches driven by 80 kA peak current, New J. Phys. 14 043021 (2012)

G.R. Johnson, R.A. Stryk, S.R. Beissel, SPH for high velocity impact computations, Comput. Methods. Appl. Mech. Eng, 139 (1-4), 347-373 (1996).

Gingold, Robert A., and Joseph J. Monaghan. "Smoothed particle hydrodynamics: theory and application to non-spherical stars", Monthly notices of the royal astronomical society 181.3: pp. 375-389 (1977)

H. Alfvén, Existence of electromagnetic-hydrodynamic waves, Nature 150 (3805), 405–406 (1942)

H. U. Rahman et al., "Shock waves in a Z-pinch and the formation of high energy density plasma", Physics of Plasmas 19, 122701 (2012)

Irvin R. Lindemuth, "Comment on “Staged z-pinch modeling of high and low atomic number liners compressing deuterium targets using parameters of the Z pulsed power facility” [Phys. Plasmas 28, 112701 (2021)]", Physics of Plasmas 29, 084702 (2022)

J. Bonet, S. Kulasegaram, Correction and stabilization of smoothed particle hydrodynamics method with applications in metal forming simulations, Internat. J. Numer. Methods Engrg. 47(6), 1189–1214 (2000)

J. Huang, N. Ding, C. Ning, S. Sun, Y. Zhang, D. Xiao, and C. Xue, Numerical investigation on the implosion dynamics of wire-array Z-pinches in (r, q) geometry, Phys. Plasmas 19, 062701 (2012)

J. J. Monaghan and R. A. Gingold, “Shock simulation by the Particle Method SPH”, J. Comput. Phys. 52(2), 374–389 (1983)

J. M. Owen, J. V. Villumsen, P. R Shapiro, H. Martel, Astrophys. J., Suppl. Ser., 116(2), 155 (1998)

J. Monaghan, "Smoothed particle hydrodynamics", Annual review of astronomy and astrophysics 30.1, 543-574 (1992)

J. P. Chittenden, et al., “Structural Evolution and Formation of High-Pressure Plasmas in X Pinches”, PRL 98, 025003 (2007)

J. R. Angus, "1D kinetic study of pinch formation in a dense plasma focus: Transition from collisional to collisionless regimes", Physics of Plasmas 28, 010701 (2021)

J. Ryu, S. Ham, J. Lee, J. Park, S. Park, Y. Choi, H. J. Woo, K. Lee, Y.-C. Ghim, Y. S. Hwang, and K.-J. Chung, “A modular X-pinch device for versatile X-pinch experiments at Seoul National University,” Rev. Sci. Instrum. 92(5), 053533 (2021)

J. Wurster, D. J. Price, and M. R. Bate, “Can non-ideal magnetohydrodynamics solve the magnetic braking catastrophe?”, Mon. Not. R. Astron. Soc. 457, 1037–1061 (2016)

J. Wurster, D. Price, and B. Ayliffe, “Ambipolar diffusion in smoothed particle magnetohydrodynamics”, Mon. Not. R. Astron. Soc. 444(2), 1104–1112 (2014)

J.C. Butcher, Numerical methods for ordinary differential equations in the 20th century, J. Comput. Appl. Math. 125 (1–2), 1-29 (2000)

J.M. Stone, and T.A. Gardiner, ATHENA: A NEW CODE FOR ASTROPHYSICAL MHD, ApJS 178, 137 (2008)

K. Eidmann, J. M. ter Vehn, T. Schlegel, S. Huller, Hydrodynamic simulation of subpicosecond laser interaction with solid-density matter, ¨ Physical Review E 62, 1202–1214 (2000)

K. Iwasaki, S.-I. Inutsuka, Smoothed particle magnetohydrodynamics with a Riemann solver and the method of characteristics, Monthly Notices of the Royal Astronomical Society 418(3), 1668–1688 (2011)

L. Vela Vela, R. Sánchez, J. M. Reynolds-Barredo, and J. Geiger, Magneto-hydrodynamical nonlinear simulations of magnetically confined plasmas using smooth particle hydrodynamics (SPH), Phys. Plasmas 26, 012511 (2019)

M. Brio and C. C. Wu, “An upwind differencing scheme for the equations of ideal magnetohydrodynamics”, J. Comput. Phys. 75, 400–422 (1988)

M. L. Wilkins, Use of artificial viscosity in multidimensional fluid dynamic

calculations, J. Comput. Phys. 36 (3), 281-303 (1980)

M. N. Saha, LIII.Ionization in the solar chromosphere, Philos. Mag. Series 6. 40 (238), 472–488 (1920)

M.B. Liu, G.R. Liu, Restoring particle consistency in smoothed particle hydrodynamics, Appl. Numer. Math, 56(1), 19-36 (2006)

M.P. Desjarlais, “Practical Improvements to the Lee-More Conductivity Near the Metal-Insulator Transition”, Contrib. Plasma Phys. 41, 267 (2001)

N. Ding, J. Wu, Z.H. Yang, S.W. Fu, C. Ning, Q. Liu, X. J. Shu, Y. Zhang, Z. H. Dai, Simulation of Z- pinch implosion using MARED code, High Power Laser Part. Beams 20, 212 (2008)

N. Ding, Y. Zhang, D. Xiao, J. Wu, Z. Dai, L. Yin, Z. Gao, S. Sun, C. Xue, C. Ning, X. Shu, J. Wang, Theoretical and numerical research of wire array Z-pinch and dynamic hohlraum at IAPCM, Matter and Radiation at Extremes 135(1), 135-152 (2016)

P. Hakel et al., "The new Los Alamos opacity code ATOMIC", Journal of Quantitative Spectroscopy and Radiative Transfer 99, 265-271 (2006)

P. Tzeferacos, M. Fatenejad, N. Flocke, G. Gregori, D. Q. Lamb, D. Lee, J. Meinecke, A. Scopatz, and K. Weide, FLASH magnetohydrodynamic simulations of shock-generated magnetic field experiments, High Energy Density Physics 8, 322–328 (2012)

P.W. Randles, L.D. Libersky, Smoothed particle hydrodynamics some recent

improvements and applications, Comput.Methods Appl. Mech. Engrg. 139 (1-4), 375-408 (1996)

R. A. Gingold, J. J. Monaghan, Smoothed particle hydrodynamics: theory and application to non-spherical stars, Mon. Not. R. Astron. Soc. 181(3), 375–389 (1977)

R. Aliaga-Rossel et al., "Plasma jet formation in x-pinch plasmas", AIP Conference Proceedings 563, 270–275 (2001)

R. K. Appartaim and B. T. Maakuu, X-pinch x-ray sources driven by a 1μs capacitor discharge, Phys. Plasmas 15, 072703 (2008)

R. M. More, Pressure ionization resonances and the continuity of bound and free states, Adv. At. Mol. Phys. 21, 305 (1985)

R. Ramis et al.,"Multi-fs – a computer code for laser–plasma interaction in the femtosecond regime¨, Computer Physics Communications 183, 637-655 (2012)

R. S. Rawat, "High energy density pinch plasma - A unique non-conventional tool for plasma nanotechnology", 2012 Abstracts IEEE International Conference on Plasma Science, Edinburgh, UK (2012)

S.-I. Inutsuka, Reformulation of Smoothed Particle Hydrodynamics with Riemann Solver, J. Comput. Phys., 179, 238 (2002)

S. A. Pikuz, T. A. Shelkovenko, and D. A. Hammer, "X-pinch. Part I," Plasma Phys. Rep. 41(4), 291 (2015)

S. A. Pikuz, T. A. Shelkovenko, V. M. Romanova, D. B. Sinars, D. A. Hammer,

S. N. Bland, S. V. Lebedev, X pinch as a source for X-ray radiography, NUKLEONIKA 46(1), 21–25 (2001)

S. Børve, M. Omang, and J. Trulsen, Regularized smoothed particle hydrodynamics: A new approach to simulation magnetohydrodynamic shocks, Astrophys. J., 561:82-93 (2001)

S. Børve, M. Omang, and J. Trulsen, TWO-DIMENSIONAL MHD SMOOTHED PARTICLE HYDRODYNAMICS STABILITY ANALYSIS, ApJS, 153, 447–462 (2004)

S. C. Bott, D. M. Haas, U. Ueda, Y. Eshaq, R. Madden, G. Collins, F. N. Beg, High-Resolution Laser Schlieren Imaging of Coronal Plasma Evolution in 80-kA X-Pinches, in IEEE Transactions on Plasma Science, 36(4), 1274-1275 (2008)

S. Ham et al., "Estimation of plasma parameters of X-pinch with time-resolved x-ray spectroscopy", Matter Radiat. Extremes 8, 036901 (2023)

S. Ham, J. Ryu, S. Park, K.-J. Chung, Y.-C. Ghim, H. J. Woo, and Y. S. Hwang, “Development of a filtered AXUV diode array for X-pinch soft x-ray spectra in the energy range of 1–10 keV,” Rev. Sci. Instrum. 92(5), 053509 (2021)

S. M .Byun, et al., “Numerical simulation for wire X-pinch plasma on 2D/3D geometry”, Physics of Plasmas 29, 062701 (2022)

S. Vanaverbeke, R. Keppens, S. Poedts, and H. Boffin, “GRADSPH: A parallel smoothed particle hydrodynamics code for self-gravitating astrophysical fluid dynamics”, Comput. Phys. Commun. 180(7), 1164–1182 (2009)

Stuart C. Whitehouse, and Matthew R. Bate, "Smoothed particle hydrodynamics with radiative transfer in the flux-limited diffusion approximation", Monthly Notices of the Royal Astronomical Society 353(4), pp.1078-1094 (2004)

T. A. Brunner, & T. A. Mehlhorn, "A user's guide to radiation transport in ALEGRA-HEDP (version 4.6)", Sandia National Laboratories (2009)

T. A. Shelkovenko, S. A. Pikuz, I. N. Tilikin, M. D. Mitchell, S. N. Bland, D.A. Hammer, Evolution of X-pinch loads for pulsed power generators with current from 50 to 5000 kA, Matter and Radiation at Extremes 3(6), 267-277 (2018)

T. Boyd and J. Sanderson, "Resistive magnetohydrodynamics," in The Physics of Plasmas, Cambridge: Cambridge University Press, pp. 140-196 (2003)

T. S. Tricco, D. J. Price, A switch to reduce resistivity in smoothed particle magnetohydrodynamics, MNRAS 436, 2810–2817 (2013)

T. S. Tricco, D. J. Price, Constrained hyperbolic divergence cleaning for smoothed particle magnetohydrodynamics, J. Comput. Phys., 231, 7214 (2012)

U. Shumlak et al., "High energy density Z-pinch plasmas using flow stabilization", AIP Conference Proceedings 1639, 76–79 (2014)

U. Shumlak, "Z-pinch fusion", Journal of Applied Physics 127, 200901 (2020)

V. I. Oreshkin, A. P. Artyomov, S. A. Chaikovsky, E. V. Oreshkin, A. G. Rousskikh, Simulation of the radiation from the hot spot of an X-pinch, Phys. Plasmas 24, 012703 (2017)

V. V. Vikhrev, et al., “MHD Simulation of X-pinch plasma dynamics”, 35th EPS Conference on Plasma Phys. Hersonissos, 9 - 13 June 2008 ECA Vol.32D, P-2.154 (2008)

V. Venugopalan et al., "Radiative transport in the diffusion approximation: An extension for highly absorbing media and small source-detector separations", PHYSICAL REVIEW E, 58(2) (1998)

W. Dehnen, H. Aly, Improving convergence in smoothed particle hydrodynamics simulations without pairing instability, Mon. Not. Roy. Astron. Soc. 425(2), 1068-1082 (2012)

W.F Noh, Errors for calculations of strong shocks using an artificial viscosity and an artificial heat flux, J. Comput. Phys. 72 (1), 78-120 (1998)

X. G. Wang, S. K. Sun, D. L Xiao, G.Q. Wang, Y. Zhang, S. T. Zhou, X. D Ren, Q. Xu, X. B. Huang, N. Ding, and X. J. Shu, Numerical study on magneto-Rayleigh–Taylor instabilities for thin liner implosions on the primary test stand facility, Chin. Phys. B 28 035201 (2019)

X. Y. Hu and N. A. Adams, An incompressible multi-phase SPH method, Journal of Computational Physics, 227(1), 264-278 (2007)

Y. B. Jo, S. H. Park, H. Y. Choi, H. W. Jung, Y. J. Kim, E. S. Kim, SOPHIA: Development of Lagrangian-based CFD code for nuclear thermal-hydraulics and safety applications, Ann. Nucl. Energy 124, 132-149 (2019)

Y. Tsukamoto, K. Iwasaki, and S.-I. Inutsuka, “An explicit scheme for Ohmic dissipation with smoothed particle magnetohydrodynamics,” Mon. Not. R.

Astron. Soc. 434(3), 2593–2599 (2013)

Y. Tsukamoto, K. Iwasaki, S.-I. Inutsuka, An explicit scheme for ohmic dissipation with smoothed particle magnetohydrodynamics, Monthly Notices of the Royal Astronomical Societ 434(3), 2593–2599 (2013)

국문 초록

고에너지밀도 물리학(HEDP)은 핵융합, 고에너지밀도 실험, 별의 생성과정 등에서 발견되는 극한 물성의 물질을 연구하는 학문이다. 최근 실험 및 계산 기술의 발전으로 고에너지밀도 물리학에 대한 연구 역량이 높아지면서 다양한 분야에서 극한 물성 연구에 대한 활용이 증가하고 있다. 이러한 고에너지 밀도를 달성하는 수단 중 하나로 플라즈마가 자기장에 의해 압축되어 고밀도를 형성하는 현상인 핀치 플라즈마가 연구되고 있다. 특히 X-핀치 플라즈마는 비교적 적은 양의 전류로 강력한 X-선을 발생시키기 때문에 고에너지 밀도 물리학을 탐구하는 데 효과적인 도구로 주목받고 있다.

핀치 플라즈마의 실험적 구현은 고성능 전류원이 필수적으로 필요하기 때문에 큰 규모의 실험실이나 연구소 중심으로 이루어져 왔으며, 매우 좁은 공간에서 짧은 시간동안 유지되는 특성 때문에 실험적 진단에 한계가 있다. 따라서 핀치 플라즈마에 대한 보다 상세한 물리 연구를 위해서는 실험적 진단을 보완할 수 있는

수치해석적 연구가 필수적이다. 핀치 플라즈마를 시뮬레이션하기 위해 개발된 기존의 자기유체역학 (MHD) 모델들은 격자기반으로 계산이 이루어지는 오일러리안 방식을 채택하고 있다. 하지만 이러한 방식은 플라즈마와 진공사이의 경계처리에 추가적인 수치 처리가 요구되며, 이러한 처리가 다양한 오류를 유발하는 것으로 보고되고 있다. 반면, 공간과 함께 물리량이 이동하는 라그랑지안 수치기법은 이러한 문제에 대해 상대적으로 자유롭다. 특히, 해석영역을 입자로 처리하여 진공과 플라즈마 영역을 완전히 분리할 수 있는 완화입자유체동역학 (SPH) 방법은 이러한 문제에 효과적이다. 이러한 관점에서 본 연구에서는 극한 조건의 핀치 플라즈마를 시뮬레이션 할 수 있는 SPH-MHD 모델을 개발하였다.

개발된 SPH-MHD 모델에는 자기장의 발산 제약을 만족시키는 보정 항과 충격파를 제어하기 위해 도입된 인공 소산 항 등 여러 가지 수치 기법들이 통합되었다. 또한 비이상적 MHD 항에 대한 새로운 SPH 이산화 식을 제안하고 도입하였다. 이렇게 개발된 모델을 검증하기 위해 세 가지 벤치마크 문제에 대한 해석을

수행하였다. 결과적으로, 수행된 시뮬레이션 결과는 다른 검증된 시뮬레이션 결과 및 이론적 결과와 잘 일치하여 도입된 수치 처리 방법들이 유효함이 확인되었다.

본 연구의 최종 목적은 개발된 코드를 활용하여 X-핀치 시뮬레이션을 수행하는 것이다. 이를 위해 X-핀치 물리에 특화된 상세 물리 모델이 코드에 통합되었다. 첫째로, 전자와 이온의 에너지를 분리하는 2 온도 방정식으로 코드를 확장했다. 수치 계산에 사용되고 있는 시간 단계의 크기가 전자-이온의 충돌 시간보다 훨씬 짧기 때문에 두 온도를 같다고 가정할 수 없고, 이러한 모델이 적절하게 활용된다. 다음으로는 X-핀치 조건에서 고에너지밀도 플라즈마 특성을 효과적으로 포착하기 위해 토마스-페르미 이론에 기반한 상태방정식을 도출하고 적용하였다. 특히 데잘레의 보정 모델을 플라즈마 이온화에 대한 균형 모델로 채택하여 저밀도 영역에서 발생하는 이온화 과대평가 문제를 해결하였다. 마지막으로, 플럭스 제한 확산 근사법을 기반으로 하는 복사 모델이 코드에 통합되어 넓은 에너지 범위에서 X-선 방출을 통한 에너지 손실을

설명한다.

마지막으로, 개발된 코드를 사용하여, 3차원 X-핀치 시뮬레이션을 수행하였고, 이 결과를 서울대학교 X-핀치 장치에서 얻어진 실험데이터와 비교하였다. 수행된 시뮬레이션은 X-핀치 플라즈마의 내파 거동을 성공적으로 포착하여, 다양한 X-핀치 구성에서 일반적으로 관찰되는 4단계의 발전과정을 정확히 재현한다. 이때, 시뮬레이션은 밀도, 온도, 속도장 및 복사 전력을 포함한 다양한 플라즈마 매개변수에 대한 포괄적인 시공간 정보를 제공한다. 특히 핫스팟에서의 전자 온도와 밀도는 실험값과 비교했을 때 합리적인 수준으로 잘 재현되어 개발된 코드의 정확성과 신뢰성을 입증하였다. 또한 시뮬레이션을 통해 계산된 방사선 데이터는 이전 시뮬레이션 결과에 비해 월등히 높은 정확도를 보여 제안 모델의 유효성을 확인할 수 있다.

본 연구에서 개발된 SPH-MHD 코드는 기존의 수치 기법으로는 해결하기 어려웠던 일부 플라즈마 시뮬레이션에 대한 좋은 대안이 될

것으로 기대된다. 결론적으로 이 코드는 핀치 플라즈마의 복잡한 거동에 대한 전반적인 지식을 제공할 수 있는 훌륭한 수단으로 확인되었으며, 고에너지밀도 물리학 연구에 기여할 수 있는 높은 잠재력을 보여준다.

주요어

고에너지밀도물리학, 완화입자유체동역학, 자기유체역학, 핀치 플라즈마, 엑스 핀치 플라즈마, 플럭스 제한 확산근사 모델

학번: 2018-34777